

Diss. ETH No. 18453

Applications of GHz Ultrasound: Material Characterization and Wave Propagation in Microstructures

A dissertation submitted to

ETH ZURICH

for the degree of
Doctor of Sciences

presented by

JÜRIG BRYNER

Dipl. Masch-Ing. ETH
born April 19, 1976
citizen of Kloten (ZH)

accepted on the recommendation of

Prof. Dr. J. Dual, examiner
Prof. Dr. Th. Dekorsy, co-examiner

2009

Acknowledgements

In the last 4 years I spent a very good and interesting time during my PhD thesis at the Center of Mechanics. I'm grateful to everyone who contributed to my thesis. Many thanks to Prof. Dr. Jurg Dual for giving me his confidence and support. He provided an excellent environment for research and guided my work giving me a lot of academic freedom.

I would like to thank Prof. Dr. Thomas Dekorsy for accepting to be my co-examiner and for reviewing my thesis.

I'm very grateful to Dr. Jacqueline Vollmann. From the beginning of my thesis she supported me with ideas and hints and we had countless inspiring discussions. She introduced me to many people of the laser acoustic community.

Many thanks to Dr. Dieter Profunser for the numerous fruitful discussions, especially regarding the experimental setup.

I'm thankful to my PhD colleagues from the laser acoustic group, Laurent Aebi and Ingo Wenke, for the good collaboration and the reviewing of my thesis. We always had a very good atmosphere in our group.

Also many thanks to Dr. Tim Kehoe from the Institut Catala de Nanotecnologia in Barcelona and to Dr. Oliver Kluth from Oerlikon Solar AG. With Tim we had an excellent collaboration regarding the investigation of polymers used for nanoimprinting lithography. With Oliver we built up the very fruitful collaboration with OC Oerlikon for the investigation of solar cell materials.

The perfect infrastructure at the Center of Mechanics is much appreciated. Traude Junker, Gabriela Squindo, Dr. Stephan Kaufmann, and Bernhard Cadonau provided excellent administrative and computational services.

Guillaume Bugnard, Ingo Wenke, Nicolas Bochud, Christine Tobler, and Onur Caglar wrote their semester, diploma, or master theses with great enthusiasm within the scope of my research.

Many thanks to my colleagues at the Center of Mechanics for the good time we had together, especially to Francesco Colombo, Andreas Schifferle, Bernard Masserey, Udo Lang, Laurent Aebi, Stefano Oberti, Sandro Dinser, Niels Quack, Andrea Cambruzzi, Dirk Moeller, Johannes Hengstler, and Thomas Schwarz.

Finally, I'm most grateful to Sandra and my family for their support and motivation throughout my thesis.

Contents

Abstract	ix
Zusammenfassung	xi
List of Figures	xiii
List of Tables	xvii
List of Abbreviations	xix
List of Symbols	xxi
1 Introduction	1
1.1 Objectives of the present work	3
1.2 Outline of this thesis	4
2 Laser acoustics: Theory and modeling	7
2.1 Overview	7
2.2 Excitation: Ultrashort laser pulse heating	8
2.2.1 Governing equations	9
2.2.2 Numerical implementation	10
2.3 Wave propagation: 1-dimensional viscoelastic model	11
2.3.1 Governing equations	12
2.3.2 Numerical implementation	14
2.3.2.1 Discretization	14
2.3.2.2 Boundary conditions	16
2.3.2.3 Stability conditions	16
2.3.3 Frequency dependence of bulk wave velocity and attenuation .	17
2.4 Wave propagation: 3-dimensional model	17
2.4.1 Governing equations	19
2.4.2 Numerical implementation	20
2.4.2.1 Discretization	20
2.4.2.2 Boundary conditions	23
2.4.2.3 Stability conditions	24
2.4.2.4 Structures with arbitrary shapes	25
2.4.3 Validation	25
2.4.3.1 Wave velocities	26
2.4.3.2 Energy	29

2.4.3.3	Long wavelengths	32
2.5	Detection: Change of reflectance	33
2.5.1	Relation between dielectric constant and reflectance	33
2.5.2	Relation between strain and dielectric constant	34
3	Experimental setup	37
3.1	Basic setup	37
3.1.1	Overview	37
3.1.2	Noise reduction	37
3.1.2.1	Double modulation	38
3.1.2.2	Cross polarization	38
3.1.2.3	Balanced photodetector	38
3.2	Collinear setup	39
3.2.1	Beam guidance	40
3.2.2	Camera	40
3.2.3	Delay line	41
3.3	Typical characteristics of a reflectance measurement	43
4	Results	47
4.1	Aluminum thin films	47
4.1.1	Introduction	47
4.1.2	Specimens	47
4.1.3	Direct analysis of the attenuation from measurements	48
4.1.4	Analysis with the viscoelastic simulation	49
4.2	Polymer films used for nanoimprint lithography	54
4.2.1	Introduction	54
4.2.2	Specimens and typical characteristics of the measurements	54
4.2.3	Bulk wave velocity	57
4.2.4	Attenuation	57
4.2.5	Effect of thickness on bulk wave velocity	59
4.2.6	Effect of surface material on bulk wave velocity	60
4.3	Structured polymer specimens	61
4.3.1	Introduction	61
4.3.2	100 μm line structures	61
4.3.3	10 μm square dots	62
4.3.4	Submicron patterns	62
4.4	Materials for thin film solar cells	66
4.4.1	Introduction	66
4.4.2	Layout of the specimens	66
4.4.3	Determination of Young's modulus with nanoindentation	66
4.4.4	Hydrogenated amorphous silicon (a-Si:H)	68
4.4.5	Hydrogenated microcrystalline silicon ($\mu\text{c-Si:H}$)	72
4.4.6	Influence of crystalline volume fraction in $\mu\text{c-Si:H}$	76
4.4.7	Low pressure chemical vapor deposited (LPCVD) ZnO	77
4.4.8	Sputtered ZnO	78
4.4.9	Silicon multilayer stack	80
4.5	Wave focusing in silicon microstructures	83

4.5.1	Introduction	83
4.5.2	Focusing properties of a tip	83
4.5.3	Detection properties of a tip	86
4.5.4	Influence of the crystallographic orientation	87
4.5.5	Strategies for future simulations	87
4.5.6	Measurements on a cantilever	89
4.5.7	Measurements in cut AFM tips	90
5	Conclusions and outlook	95
5.1	Theory and modeling	95
5.2	Experimental setup	95
5.3	Experimental results	96
A	Appendix	99
A.1	Parameters used for the two temperature model	99
	References	101
	Curriculum vitae	109
	List of publications	111

Abstract

Short pulse laser acoustics is a powerful method for measurements and the characterization of thin films and microstructures. With the pump probe technique laser pulses with a duration of about 100 fs excite mechanical waves in the specimen of interest. These laser pulses are called pump pulses. The waves propagate into the specimen and at the interfaces and boundaries of the specimen the waves are scattered. The waves propagating back to the surface can be detected by laser pulses with a variable time delay with respect to the excitation, the probe pulses. The presence of mechanical strain influences the optical reflectivity at the surface of the specimen. This is called the photoelastic effect. So by the measurement of the intensity of the probe pulses reflected at the surface of the specimen it is possible to determine the times of arrival of mechanical waves.

For the full interpretation of the pump probe measurements and for the extraction of as much as possible information from the measurements it is essential to have a numerical simulation tool. In this work a complete one dimensional numerical simulation tool based on finite differences is presented. The excitation of the mechanical waves by the pump laser pulse is modeled with a two temperature model. Two temperature models take into account that during very fast heating processes in metals the temperature of the electrons and the lattice are not in equilibrium. The wave propagation is modeled with a viscoelastic material model, the standard linear solid. The viscoelastic model incorporates the attenuation of the mechanical waves. The detection of the mechanical waves is modeled with a photoelastic model. With the simulation tool it is possible to interpret and quantitatively evaluate pump probe measurements of multilayered specimens with interfering wave patterns. The thickness and attenuation of buried layers can be determined with the help of this tool. Additionally, for microstructures with lateral boundaries the wave propagation is simulated using a 3-dimensional model.

In this work the laser acoustic pump probe technique using ultrasound in the GHz regime is applied to specimens with thicknesses of some nanometers up to some microns. The lower limit of detectable thicknesses is determined by the wavelength of the mechanical waves. The wavelength of the mechanical waves must be smaller or in the order of the object to be detected. The upper limit is theoretically determined by the attenuation of the mechanical waves only. In the application the maximum time window of the experimental setup must be large enough to capture the reflected mechanical waves. The experimental setup is explained and some important features are discussed in detail. A collinear beam guidance is applied to the pump and probe beams in order to use a microscope objective for an enhanced focusing with spot dimensions of 3-5 μm . The delay line enabling the temporal shift between pump and probe beam is equipped with two retroreflectors. This configuration

allows multiple reflections and thus is increasing the maximum time window of the measurements. At the same time the use of retroreflectors instead of single mirrors decreases measurement errors caused by beam walking.

Two differently deposited aluminum thin films are investigated regarding their attenuation. It turns out that there is a significant attenuation in the GHz regime and that the attenuation in the sputtered film is about 3 times higher than in the film deposited by electron-beam evaporation. For the analysis of the attenuation in buried layers, the attenuation in the aluminum top layer must be considered.

The analysis of polymers used for nanoimprinting lithography reveals that there is a significant attenuation in the range of 50 GHz, but it is still on a similar level as in sputtered aluminum. So pump probe measurements on polymer specimens with thicknesses in the range of some hundred nanometers are possible without difficulties. Moreover, for PMMA specimens thinner than 80 nm, an increase of the bulk wave velocity is found. Additionally, an influence of the surface material on bulk wave velocity is found for very thin PMMA layers with thicknesses in the range of 10-30 nm. With measurements on different structured polymer specimens the capabilities of the pump probe setup regarding lateral characterization is shown. For structured specimens with feature sizes between 10 and 100 μ m laterally resolved measurements are done. Like this in a scanning setup 2-dimensional thickness maps can be generated. Specimens with submicron structures are analyzed by measuring their mechanical resonance frequencies. This procedure is successfully shown for specimens with imprinted holes.

A measurement series is done with thin films used in photovoltaics with special interest on the active area materials: Hydrogenated amorphous silicon and hydrogenated microcrystalline silicon. For both, amorphous and microcrystalline silicon films, the determined mechanical properties as bulk wave velocity, Young's modulus, and density significantly differ from the values for crystalline bulk material. E.g. the bulk wave velocity of the amorphous silicon films is found to be 8.4% smaller, and that of microcrystalline silicon films is found to be 3.7% smaller than the value for crystalline silicon [100]. For the microcrystalline silicon specimens a correlation between the crystalline volume fraction and the bulk wave velocity is found. Photovoltaic multilayer stacks with several layers are successfully analyzed with the pump probe setup. With a single pump probe measurement, the thickness of 4 layers is determined.

Silicon microstructures, i.e. modified atomic force microscopy (AFM) tips, are analyzed numerically and experimentally. By a 3-dimensional numerical orthotropic model the wave propagation is simulated in silicon tips regarding their applicability for the focusing and detection of mechanical waves. The simulations show that a compromise must be found between optimal focusing and optimal detection properties. Pump probe measurements of a series of 4 modified AFM tips show the feasibility of launching and detecting waves in the GHz regime in 3-dimensional micro structures.

Zusammenfassung

Die Kurzpuls Laserakustik ist sehr gut geeignet für die Messung und die Charakterisierung von Dünnschichten und Mikrostrukturen. Die Pump Probe Technik verwendet ungefähr 100 fs lange Laserpulse, um in der zu untersuchenden Probe mechanische Wellen anzuregen. Diese Laserpulse werden Pumppulse genannt. Die Wellen breiten sich im Probenstück aus und werden an Materialübergängen und an Grenzflächen reflektiert. Die Wellenpakete, die an die Oberfläche des Probenstücks zurücklaufen, können mit zeitlich versetzten Laserpulsen, den Probepulsen, detektiert werden. Mechanische Dehnung verändert die optischen Reflexionseigenschaften an der Oberfläche eines Probenstücks. Diese Eigenschaft wird photoelastischer Effekt genannt. Mit der Messung der Intensität der an dem Probenstück reflektierten Probepulse können so Ankunftszeiten mechanischer Wellen bestimmt werden.

Für die vollständige Interpretation von Pump Probe Messungen und um möglichst viel Information aus den Messungen zu kriegen, ist es wichtig ein numerisches Simulationstool zu haben. In dieser Arbeit wird ein komplettes eindimensionales numerisches Tool präsentiert, das auf finiten Differenzen basiert. Die Anregung der mechanischen Wellen durch den Pump Laserpuls wird mit einem Zweitemperatur-Modell modelliert. Im Zweitemperatur-Modell wird berücksichtigt, dass bei sehr schneller Erwärmung in Metallen die Elektronen und das Gitter nicht im thermischen Gleichgewicht sind. Die Wellenausbreitung wird mit einem viskoelastischen Modell modelliert, dem sogenannten linearen Standardkörper. Das viskoelastische Modell berücksichtigt die Dämpfung von mechanischen Wellen. Die Detektion der mechanischen Wellen wird mit einem photoelastischen Modell simuliert. Mit dem Simulationstools ist es möglich, Pump Probe Messungen von mehrschichtigen Proben mit interferierenden Wellenmustern zu interpretieren und quantitativ auszuwerten. Selbst für verdeckte Schichten können die Dicke und die Dämpfung mit diesem Tool bestimmt werden. Für Mikrostrukturen mit seitlichen Grenzflächen wird die Wellenausbreitung mit einem dreidimensionalen Modell simuliert.

In dieser Arbeit wird die laserakustische Pump Probe Technik, die mit Ultraschall im GHz-Bereich arbeitet, angewendet auf Probenstücke mit Dicken im Bereich von einigen Nanometern bis hinauf zu einigen Mikrometern. Die untere Grenze von detektierbaren Schichtdicken ist bestimmt durch die Wellenlänge der mechanischen Wellen. Die Wellenlänge der mechanischen Wellen muss kleiner oder in der gleichen Größenordnung sein, wie die Dicke der zu untersuchenden Schicht. Die obere Grenze von detektierbaren Schichtdicken ist theoretisch nur durch die Dämpfung der mechanischen Wellen limitiert. In der Praxis muss zusätzlich das maximal mögliche Zeitfenster des Messaufbaus gross genug sein, um die reflektierten mechanischen Wellen zu detektieren. Der Messaufbau wird erklärt und die wichtigsten Komponenten werden detailliert diskutiert. Um für eine verbesserte Fokussierung ein

Mikroskopobjektiv gebrauchen zu können, wird eine kollineare Strahlführung für den Pump und den Probe Laser verwendet. Das verwendete Mikroskopobjektiv fokussiert die Laserstrahlen auf einen Durchmesser im Bereich von 3-5 μm . Die Delay-Line, die den Zeitversatz zwischen Pump und Probe Laser steuert, ist mit zwei Retroreflektoren ausgestattet. Das ermöglicht Mehrfachreflexionen, die das maximal mögliche Zeitfenster des Messaufbaus vergrössern. Gleichzeitig verkleinern die Retroreflektoren Messfehler durch Beam Walking im Vergleich zu Einzelspiegeln.

Zwei unterschiedlich aufgebrauchte Aluminiumschichten werden hinsichtlich ihrer Dämpfung untersucht. Es stellt sich heraus, dass die Dämpfung im GHz Bereich beträchtlich ist und sie in der gesputterten Schicht etwa 3 Mal grösser ist als in der aufgedampften Schicht. Die Dämpfung in Aluminiumschichten muss berücksichtigt werden bei der Untersuchung der Dämpfung von darunterliegenden Schichten.

Die Analyse von Polymerschichten, die in der Nanoimprinting Lithographie verwendet werden, zeigt, dass die Dämpfung im Bereich von 50 GHz in Polymerschichten zwar beträchtlich ist, aber nicht signifikant grösser als in gesputterten Aluminiumschichten. Deshalb sind Pump Probe Messungen in Polymerschichten mit Dicken von einigen hundert Nanometern kein Problem. Für Polymerschichten dünner als 80 nm werden erhöhte P-Wellengeschwindigkeiten gemessen. Zusätzlich wird für sehr dünne Polymerschichten mit Dicken im Bereich von 10-30 nm ein Einfluss vom Trägermaterial auf die P-Wellengeschwindigkeit festgestellt. Messungen auf strukturierten Polymerproben zeigen das Potential der Pump Probe Technik hinsichtlich örtlich aufgelösten Messungen. Polymerproben mit Strukturgrössen zwischen 10 und 100 μm werden örtlich aufgelöst gemessen. So können in einem Scanprozess zweidimensionale Dickenkarten erstellt werden. Proben mit Strukturgrössen im Submikrometerbereich werden mit der Messung von Resonanzfrequenzen charakterisiert. Dies wird an Proben mit Lochstrukturen erfolgreich gezeigt.

Für Dünnschichten, die in der Photovoltaik eingesetzt werden, wird eine Messreihe durchgeführt. Der Fokus dieser Messungen liegt auf den amorphen und mikrokristallinen Siliziumschichten. Für beide Typen von Siliziumschichten weichen die gemessenen mechanischen Eigenschaften wie P-Wellengeschwindigkeit, E-Modul und Dichte erheblich von den Werten von kristallinen Proben ab. Zum Beispiel ist die gemessene P-Wellengeschwindigkeit in den amorphen Siliziumfilmen um 8.4% kleiner und in den mikrokristallinen Filmen um 3.7% kleiner als in kristallinem Silizium [100]. Für die mikrokristallinen Proben wird ein Zusammenhang zwischen dem Kristallinitätsgrad und der P-Wellengeschwindigkeit festgestellt. Mehrschichtige Proben aus der Photovoltaik werden erfolgreich mit Pump Probe Messungen untersucht. Mit einer einzelnen Pump Probe Messung können die Dicken von 4 verschiedenen Schichten bestimmt werden.

Modifizierte Siliziumspitzen aus der Atomkraftmikroskopie (AFM Spitzen) werden numerisch und experimentell untersucht. Mit einem dreidimensionalen numerischen orthotropen Modell wird die Wellenausbreitung in den Spitzen analysiert. Das Ziel ist eine optimale Fokussierung und Detektion von mechanischen Wellen. Die Simulationen zeigen, dass ein Kompromiss zwischen guter Fokussierung und guten Detektionseigenschaften gefunden werden muss. Eine Messreihe mit 4 modifizierten AFM Spitzen belegt, dass mechanische Wellen im GHz Bereich in dreidimensionalen Mikrostrukturen angeregt und wieder gemessen werden können.

List of Figures

2.1	Simulation model: Laser power density S , stress σ , strain ε , reflectance change ΔR , and sensitivity function $F(z)$	8
2.2	Standard linear solid.	12
2.3	Creep compliance function of the standard linear solid.	13
2.4	Typical specimen with two thin film layers and the substrate: The simulated part of the substrate is only some nanometers thick.	14
2.5	Staggered grid for the spatial discretization. The stress grid points are marked with filled circles, the velocity grid points are marked with arrows.	15
2.6	Staggered grid for the spatial discretization: Situation at the boundary. The stress grid points are marked with filled circles, the velocity grid points are marked with arrows.	16
2.7	Staggered grid for the spatial discretization: Situation at the position where Mur's law is applied. The stress grid points are marked with filled circles, the velocity grid points are marked with arrows.	16
2.8	Frequency dependent properties of the standard linear solid for three parameter sets (double logarithmic plots). Upper diagram: Storage modulus \bar{E}' . Lower diagram: Attenuation α	18
2.9	Orientation of the calculation axes and the orthotropic axes of the material.	19
2.10	Unit cell for the discretization at the position $x = i, y = j, z = k$	21
2.11	Situation at the boundary $i = 1$: involved grid points for the calculation of v_x , according to equation (2.88).	23
2.12	Step-like approximation of the stress-free boundary conditions to the 'real' geometry (dashed line).	25
2.13	Normalized stress excitation signal for the considerations in the chapters 2.4.3.1 and 2.4.3.2.	26
2.14	Slowness curves for silicon: The group velocities \underline{v}_G are parallel to the corresponding propagation directions \underline{n} for the [100] and [110] direction, and equal to the phase velocities.	27
2.15	Excited layers for the wave propagation in the [100], [110], and [111] direction, respectively.	28
2.16	Determination of the velocity for the case 1.	28
2.17	Temporal evolution of the energy in Case 2 for the first 55 ps: total energy (solid line), kinetic energy (dashed line), and potential energy (dotted line).	31

2.18	Upper part: Sketch with the excitation at the base surface and the four sections. Lower part: Numerically calculated displacement amplitudes in z-direction in the cross-sections S1-S4.	31
3.1	Main components of the basic pump probe setup (figure taken from Profunser [60]).	38
3.2	Basic setup in detail (figure taken from Profunser [60]).	39
3.3	Layout of the collinear setup. NDF: Neutral density filter.	40
3.4	Left: 3x delay line. Right: Realignment of the pump and the probe beams by the polarizing beam splitter and the coupling of the camera.	41
3.5	Frontal view on a schematic retroreflector: The position of the outgoing beam (<i>Out</i>) corresponds to the position of the incident beam (<i>In</i>) mirrored at the center of the retroreflector (<i>C</i>).	41
3.6	Left: Top view of the 3x delay line. Right: Side view of the 3x delay line.	42
3.7	Measurement of the total reflectance change of a 115 nm Al film deposited by e-beam evaporation on a sapphire wafer (solid line). The dotted line corresponds to the thermal contribution to the reflectance change.	43
3.8	Acoustic contribution to the reflectance change of a 115 nm Al film deposited by e-beam evaporation on a sapphire wafer.	44
4.1	Upper diagram: Acoustic contribution to the reflectance change for a 304 nm Al film deposited by e-beam evaporation on a sapphire substrate. Lower diagram: Magnitudes of the Fourier transforms.	49
4.2	Upper diagram: Acoustic contribution to the reflectance change for a 319 nm Al film sputtered on a sapphire substrate. Lower diagram: Magnitudes of the Fourier transforms.	50
4.3	Left: Viscoelastic simulation of the stress field in the 304 nm Al film deposited by e-beam evaporation on a sapphire substrate. Right: Schematic sketch of the specimen.	51
4.4	Acoustic contribution to the reflectance change of the 304 nm Al film deposited by e-beam evaporation on a sapphire substrate: Measurement, viscoelastic simulation, and elastic simulation.	52
4.5	Reflectance change and attenuation of the 304 nm Al film deposited by e-beam evaporation on a sapphire substrate: Comparison between measurement and viscoelastic simulation.	53
4.6	Left: Viscoelastic simulation of the stress field in a typical polymer specimen. Right: Schematic picture of the specimen.	55
4.7	Measurement of the acoustic contribution to the reflectance change of a typical polymer specimen. Δt_{PMMA} is the roundtrip time for the mechanical wave packet within the PMMA layer.	56
4.8	Acoustic contribution to the reflectance change of a specimen with an Al layer of 35 nm and a PMMA layer of 30 nm. Three simulations are compared to the measurement curve.	58

4.9	Acoustic contribution to the reflectance change: Measurements and viscoelastic simulations for the fitting of attenuation α . Left: 346 nm PMMA specimen. Right: 590 nm PMMA specimen.	59
4.10	Bulk wave velocity in PMMA layers as a function of thickness: Measurements and an exponential fit.	60
4.11	Bulk wave velocity in thin PMMA layers with and without HMDS primer.	61
4.12	Structured polymer specimen with 100 μm line structures. The image is taken with a confocal light microscope.	62
4.13	Thickness measurements (200 μm line scan) on the specimen shown in Fig. 4.12. Due to a imperfect imprinting there are walls at the edges of the line.	63
4.14	Structured polymer specimen with 10 μm square dots. The image is taken with a confocal light microscope.	63
4.15	Specimen with 10 μm square dots: Measurements of the acoustic contribution to the reflectance change at two different positions. Left: Position between the dots. Right: Position on a dot.	64
4.16	SEM top view images of Area 1 and Area 2. Depending on the lateral position the holes with nominal diameter 350 nm are distorted differently due to problems during the imprinting process.	64
4.17	Specimen with submicron holes measured at point 1 of area 1 (see also table 4.4). Left: Measurement of the acoustic contribution to the reflectance change. Right: Magnitude of the Fourier transform.	65
4.18	Schematic sketch of the specimens with layers from photovoltaics.	67
4.19	Hemisphere of influence for the deformation field during nanoindentation, figure taken from Jung et al. [41].	68
4.20	Left: Structure of a-Si:H. Right: Structure of crystalline Si. In crystalline Si there is long range order whereas in a-Si:H not even short range order is present. Figures taken from Meiloud [51].	69
4.21	Measurement of the acoustic contribution to the reflectance change of a typical a-Si:H specimen. Thickness Al layer 42 nm, thickness a-Si:H layer 186 nm.	70
4.22	Nanoindentation measurements of a 192 nm a-Si:H layer on a float glass substrate.	71
4.23	Left: Structure of μc -Si:H. Right: Structure of crystalline Si. In crystalline Si there is long range order whereas in μc -Si:H only short range order (some tens of Nanometers) is present. Figures taken from Meiloud [51].	72
4.24	Structure of a μc -Si:H film depending on the crystalline volume fraction. Figure taken from Senoussaoui et al. [69].	73
4.25	Measurement of the acoustic contribution to the reflectance change of a typical μc -Si:H specimen. Thickness Al layer 41 nm, thickness μc -Si:H layer 208 nm.	74
4.26	Nanoindentation measurements of a 208 nm μc -Si:H layer on a float glass substrate.	75

4.27	Measurement of the acoustic contribution to the reflectance change of the series with increasing crystalline volume fraction.	77
4.28	Measurement of the acoustic contribution to the reflectance change of the LPCVD ZnO specimen with flat surface and a thickness of 1716 nm.	78
4.29	Measurement of the acoustic contribution to the reflectance change of a typical sputtered ZnO specimen. Thickness Al layer 54 nm, thickness ZnO layer 211 nm.	79
4.30	Schematic sketch of the multilayer specimen.	80
4.31	Acoustic contribution to the reflectance change of the multilayer stack shown in Fig. 4.30: Measurement and simulation with a pure elastic model for the wave propagation.	81
4.32	Elastic simulation of the stress field in the multilayer specimen. . . .	81
4.33	Focusing tip acting as an acoustic lense.	83
4.34	Cross-sections of the five investigated tips.	84
4.35	Averaged displacements in z-direction (see Fig. 4.34) at the sharp end of the tips.	85
4.36	The non-uniform displacement distributions at the sharp end after 100 ps and 106 ps for case 2.	85
4.37	Averaged displacements in z-direction at the base surface of the tips for cases 1 and 2 as described in Fig. 4.34.	86
4.38	Averaged displacements in z-direction (see Fig. 4.34 for geometries) at the sharp end of the tips. The z-axis of the pyramid is either parallel to the [001] or to the [011] crystal axis.	88
4.39	SEM image (done at the EMPA in Dübendorf) of a cantilever with AFM tip. The upper side of the cantilever (left hand side in the image) is coated with an approximately 35 nm thick Al layer.	89
4.40	Measurement of the acoustic contribution to the reflectance change of a Si cantilever with a thickness in the range of 2 μm and an approximately 35 nm thick Al top layer.	90
4.41	Measurement of the acoustic contribution to the reflectance change of a Si cantilever with a thickness in the range of 2 μm and an approximately 35 nm thick Al top layer. Zoomed view of the first 25 ps.	91
4.42	SEM image (done at the EMPA in Dübendorf) of a cut AFM tip. . . .	92
4.43	Left: Measurements of the acoustic contribution to the reflectance change of 4 cut AFM tips with different lengths. Right: SEM images of the 4 corresponding tips.	93
4.44	Zoomed views of the first echoes of the measurements shown in Fig. 4.43. The signals are normalized to their maximum amplitude.	94

List of Tables

2.1	Dimensions of the gridpoint matrices for the different variables. . . .	21
2.2	Listing of the reference cases and the corresponding analytically calculated velocities.	27
2.3	Numerical simulation: Values of the stress excitation components, the numerically calculated velocities, and the deviations to the analytically calculated velocities of table 2.2.	29
2.4	Validation for long wavelengths: Comparison between analytically calculated and numerically simulated displacement amplitudes for the cross-sections shown in Fig. 2.18.	32
4.1	Listing of the deposition process parameters for the e-beam evaporated Al film.	48
4.2	Listing of the deposition process parameters for the sputtered Al film.	48
4.3	Bulk wave velocity measurements of polymer specimens with thicknesses in the range of 300 nm: Bulk wave velocity c_p , standard deviation of the measured velocities, Poisson's ratio ν (assumption), density ρ (given by the manufacturer), and Young's modulus E (calculated).	58
4.4	Specimen with submicron holes: Resonance frequencies in areas 1 and 2.	65
4.5	Listing of the deposition process parameters for the a-Si:H layers.	69
4.6	Summary of the properties of a-Si:H films with thicknesses in the range of 200 nm.	71
4.7	Listing of the deposition process parameters for the μ c-Si:H layers.	72
4.8	Summary of the properties of μ c-Si:H films with thicknesses in the range of 200 nm.	74
4.9	Results of the series with different crystallinity: Thickness d , crystalline volume fraction ϕ , imaginary part of complex refractive index κ , and bulk wave velocity c_p	77
A.1	Al films simulated in chapters 4.1.4 and 4.2.4: Material properties used for the simulations of the excitation with the two temperature model.	99

List of Abbreviations

a-Si:H	Hydrogenated amorphous silicon
AFM	Atomic force microscopy
ASOPS	Asynchronous optical sampling
CAD	Computer aided design
e-beam	Electron-beam
FE	Finite elements
FIB	Focused ion beam
HDMS	Hexamethyldisilazane
HF-PECVD	High frequency plasma enhanced chemical vapor deposition
ITRS	International roadmap for semiconductors
LPCVD	Low pressure chemical vapor deposition
μ c-Si:H	Hydrogenated microcrystalline silicon
MEMS	Micro electro mechanical systems
MPI	Message passing interface
NDF	Neutral density filter
NIL	Nanoimprint Lithography
PMMA	Polymethylmethacrylat
SEM	Scanning electron microscope
TCO	Transparent conductive oxide
VS-FDTD	Velocity stress finite difference time domain method

List of Symbols

Roman alphabet

a	[m]	Contact radius of nanoindenter
A	[-]	Fitting parameter for nanoindentation
\bar{A}^0	[m ² /N]	Constant
$\Delta\bar{A}^0$	[m ² /N]	Constant
B	[m]	Parameter of the retroreflector position
c_0	[m/s]	Speed of light in vacuum
c_p	[m/s]	Bulk wave velocity
C	[-]	Fitting parameter for nanoindentation
C_{11}, C_{12}, C_{44}	[N/m ²]	Stiffness coefficients
C_c	[-]	Dimensionless constant
C_e	[J/m ³ K]	Heat capacity of the electrons
C_{e0}	[J/m ³ K]	Heat capacity of the electrons at reference temperature
C_l	[J/m ³ K]	Heat capacity of the lattice
d	[m]	Thickness
d_{tl}	[m]	Thickness of the top metal layer
D_e	[-]	Dimensionless constant
E	[N/m ²]	Young's modulus
\bar{E}	[N/m ²]	P-wave modulus
E_0	[N/m ²]	Young's modulus
E_1	[N/m ²]	Young's modulus
E_2	[N/m ²]	Young's modulus
E_∞	[N/m ²]	Young's modulus
E_{In}	[N/As]	Electric field of an incoming wave
E_{kin}	[J]	Kinetic energy
E_{pot}	[J]	Potential energy
E_{tot}	[J]	Total Energy
E_r	[N/m ²]	Reduced modulus
$E_{R\Delta\epsilon}$	[N/As]	Electric field of a reflected wave
E^*	[N/m ²]	Complex modulus
E'	[N/m ²]	Storage modulus
\bar{E}'	[N/m ²]	P-wave storage modulus
E''	[N/m ²]	Loss modulus
f	[1/s]	Frequency
f_0	[rad/m]	Constant of the sensitivity function
$F(z)$	[1/m]	Sensitivity function

List of Symbols

g_{xx}	[N/m ²]	Stress excitation term component
g_{yy}	[N/m ²]	Stress excitation term component
g_{zz}	[N/m ²]	Stress excitation term component
g_{yz}	[N/m ²]	Stress excitation term component
g_{xz}	[N/m ²]	Stress excitation term component
g_{xy}	[N/m ²]	Stress excitation term component
G	[W/m ³ K]	Electron-phonon coupling factor
h	[m]	Maximum penetration depth of nanoindenter
I_L	[W/m ²]	Laser intensity
$J_c(t)$	[m ² /N]	Creep compliance function
$\bar{J}_c(t)$	[m ² /N]	P-wave modulus creep compliance function
$\bar{J}_c(0)$	[m ² /N]	Constant
$\dot{\bar{J}}_c^0$	[m ² /N]	Constant
$\Delta\dot{\bar{J}}_E^0$	[m ² /N]	Constant
k	[rad/m]	Electromagnetic wave number
k^*	[rad/m]	Complex electromagnetic wave number
K_e	[W/mK]	Thermal conductivity of the electrons
K_{e0}	[W/mK]	Thermal conductivity of the electrons at equilibrium
L_1	[m]	Parameter of the retroreflector position
L_2	[m]	Parameter of the retroreflector position
n	[-]	Real part of the refraction index
n^*	[-]	Complex refraction index
$\partial n/\partial \varepsilon$	[-]	Photoelastic constant
N	[-]	Dimensionless constant
NR	[-]	Number of roundtrips on the delay line
Q	[-]	Quality factor
r_0	[-]	Reference reflectivity
r_{FS}	[-]	Bulk force reflection coefficient
r'	[-]	Reflection coefficient
Δr	[-]	Reflectivity change
R	[-]	Reflectance
ΔR	[-]	Reflectance change
S	[W/m ³]	Laser power density
t	[s]	Time coordinate
t_0	[s]	Normalizing time
t_f	[s]	Time of flight
t_{fv}	[-]	Transmission coefficient from film into vacuum
t_{pulse}	[s]	Laser pulse duration
t_{vf}	[-]	Transmission coefficient from vacuum into film
Δt	[s]	Time step
T_0	[K]	Reference temperature
T_e	[K]	Temperature of the electrons
T_l	[K]	Temperature of the lattice
T_{xx}	[N/m ²]	Normal stress component
T_{yy}	[N/m ²]	Normal stress component

T_{zz}	[N/m ²]	Normal stress component
T_{yz}	[N/m ²]	Shear stress component
T_{xz}	[N/m ²]	Shear stress component
T_{xy}	[N/m ²]	Shear stress component
ΔT_l	[K]	$T_l - T_0$
u	[m]	Displacement
v	[m/s]	Velocity
x	[m]	Spatial coordinate
Δx	[m]	Spatial step
y	[m]	Spatial coordinate
Δy	[m]	Spatial step
z	[m]	Spatial coordinate
z_0	[m]	Normalizing length
Δz	[m]	Spatial step
Z	[kg/m ² s]	Acoustic impedance

Greek alphabet

α	[1/m]	Attenuation
α_{th}	[1/K]	Thermal expansion coefficient
γ	[J/m ³ K ²]	Grüneisen constant
δ	[-]	Dirac function
ϵ^*	[-]	Complex dielectric constant
$\Delta\epsilon^*$	[-]	Change of the complex dielectric constant
ϵ	[-]	Strain
ϵ_{xx}	[-]	Normal strain component
ϵ_{yy}	[-]	Normal strain component
ϵ_{zz}	[-]	Normal strain component
ϵ_{yz}	[-]	Shear strain component
ϵ_{xz}	[-]	Shear strain component
ϵ_{xy}	[-]	Shear strain component
η	[Ns/m ²]	Newtonian damper
θ_e	[-]	Normalized temperature of the electrons
θ_l	[-]	Normalized temperature of the lattice
κ	[-]	Imaginary part of the refraction index
$\partial\kappa/\partial\epsilon$	[-]	Photoelastic constant
λ	[m]	Wavelength of the mechanical waves
λ_L	[m]	Wavelength of the laser
ν	[-]	Poisson's ratio
ξ	[m]	Absorption length
ρ	[kg/m ³]	Mass density
σ	[N/m ²]	Stress
τ	[-]	Normalized time coordinate
τ_0	[-]	Time constant in the viscoelastic model
$\Delta\tau$	[-]	Normalized time step
ϕ	[-]	Crystalline volume fraction

List of Symbols

χ	[-]	Normalized spatial coordinate
$\Delta\chi$	[-]	Normalized spatial step
Ψ	[-]	Memory variable
ψ	[-]	Constant of the sensitivity function
ω	[rad/s]	Circular frequency

1 Introduction

During the last two decades laser acoustics has become a well established technique for the investigation of thin films. In 1986 Thomsen et al. [76] reported about measurements performed with picosecond laser pulses. They launched and detected mechanical waves in thin film layers with thicknesses in the range of 100 nm. Two laser pulses have been used: A pump pulse for the excitation of the mechanical waves and a probe pulse for the detection of the waves. For this reason this technique is called pump probe technique. The optical reflectance on the surface of the thin film is influenced by mechanical strain. So by measuring the intensity of the reflected probe pulses the roundtrip time of the mechanical waves can be determined. They also presented a theory about the excitation of the waves, their propagation, and the detection. This measurement technique was first introduced for opaque films deposited as single layers on a substrate. In the following years several groups presented various improvements and new application fields for this measurement technique. Some important steps are shortly discussed in the following.

Enhanced detection techniques

In 1992 Wright [85] presented pump probe measurements on transparent layers. He also developed a theory for the different contributions to the reflectivity change in transparent layers. Shortly later Wright et al. [86] introduced a detection technique which is based on the angular deflection of the probe beam. Perrin et al. [57], [58], introduced an interferometric detection scheme. By the use of a Mach-Zehnder interferometer they were able to detect not only changes of the amplitude but also changes of the phase of the reflected probe beam. The phase of the reflected probe beam is directly related to the displacement of the specimen surface. Hurley et al. [39] used also an interferometric setup, but with a modified Sagnac interferometer. They demonstrated this setup on gold films. In 2006 Bartels et al. [5] presented a revolutionary concept for pump probe measurements without a mechanical delay line. Their asynchronous optical sampling (ASOPS) technique works with two mode locked lasers operated with two slightly different repetition rates. The pump and probe beams are guided with fixed optical pathes to the specimen. The temporal shift between the pump and probe pulses is achieved by their different repetition rates.

Applications to different types of specimens

Thomsen et al. [76] started with opaque thin films. As mentioned above, Wright [85] presented pump probe measurements on transparent layers. He investigated α -SiO₂ films. Lee et al. [45] and Bretz et al. [9] from Sachse's group characterized transparent polymer top layers deposited on a metallic transducer film. Morath et

al. [54] also investigated polymers, but their specimens had a different layout. They deposited the polymer layer directly on a substrate and used an Al top layer as transducer film. They investigated the attenuation in PMMA for frequencies of 90 GHz and above.

Although the lateral resolution of pump probe measurements is limited to approximately the wavelength of the laser, measurements on nanostructures are possible. Such structures can be analyzed by investigating their resonance frequencies or vibrational modes excited by the pump pulse. Lin et al. [47] from Maris' group studied vibrational modes of gold nanostructures, stripes and dots, with lateral repeat distances in the range of 200 nm. Bienville et al. [7] from Perrin's group investigated individual and collective vibrational modes of nanostructures. They measured square platinum and aluminum dots with different spacings between them and with different focal spot sizes. Dekorsy et al. [23], [24] used the ASOPS technique to investigate the acoustic dynamics of superlattices and of gold triangles on different substrates.

Some groups also presented papers about pump probe measurements in liquids. Shelton et al. [70] from Maris' group investigated the velocity of phonons in water. In 2008 Wright et al. [87] presented pump probe measurements in liquid mercury. They investigated the frequency dependent attenuation and sound velocity at frequencies up to 10 GHz.

A new application of pump probe measurements is given by Decremps et al. [21]. They combined a pump probe setup with a diamond anvil cell in order to investigate sound velocity and attenuation of specimens under pressures of tens of GPa.

Mechanical wave types

In most laser acoustic pump probe experiments the pump laser irradiates a spot with a diameter of several microns but penetrates the transducer layer only some tens of nanometers, see also chapter 2.1. Like this in isotropic materials or in symmetrically cut crystals only longitudinal mechanical waves in the depth direction are excited. Several groups presented different approaches to excite and detect also shear waves and surface waves.

Hurley et al. [40] excited shear waves indirectly by mode conversion at an interface between an isotropic film and an obliquely cut anisotropic film. Later, Matsuda et al. [50] and Pezeril et al. [59] excited shear waves directly on an anisotropic crystal. Recently, theories are presented concerning the photoelastic detection of shear waves by Dehoux et al. [22] and Matsuda et al. [49].

Wright et al. [88] used the pump probe technique for the excitation and detection of surface acoustic waves in isotropic and anisotropic materials. By lateral 2-dimensional scans they could image the propagation of surface acoustic waves up to 1 GHz. With this technique Profunser et al. [62] imaged surface acoustic waves on a phononic crystal.

1.1 Objectives of the present work

At the Center of Mechanics at the ETH laser acoustic measurements have been done for the first time by Profunser in a former PhD project [60]. One of the outcomes of this project was a pump probe setup (see chapter 3.1 'Basic setup') which was successfully tested and used for various applications, [60]: Measurements of various metallic thin films, characterization of transparent materials, freestanding membranes, and barrier layers, first feasibility studies for measurements of silicon microstructures, among others. In parallel, a simulation tool incorporating a linear elastic material model for the wave propagation was developed in order to interpret the pump probe measurements.

The objective of the present work is mainly the analysis of four different kind of specimens with the pump probe measurement technique. The kinds of specimens being investigated, and the necessary enhancements regarding the pump probe setup and regarding the simulation tools are shortly discussed in the following. More background about the different specimens and the motivation for the investigations of them can be found in the respective introduction sections in chapter 4.

Aluminium thin films

Aluminum thin films are often used as transducer top layer for pump probe measurements. So it is important to know the properties of the aluminum top layer regarding the investigation of the buried layers of interest. Two different aluminum specimens shall be investigated regarding the attenuation of mechanical waves. Since the wave patterns of such single film specimens are quite simple, the attenuation can be calculated directly from the measurements. A simulation tool implemented for the determination of the attenuation in more complex specimens shall be validated with these results.

Polymers used for nanoimprinting lithography

The polymer specimens which shall be investigated in this thesis have thicknesses between 10 and 600 nm. Polymers exhibit a strong attenuation of acoustic waves. In order to fully interpret pump probe measurements of such specimens, the implementation of a simulation tool with a viscoelastic material model is necessary. Additionally, due to the strong attenuation in thick polymer specimens higher energy densities of the pump laser pulses are necessary compared to the setup of Profunser [60]. This can be achieved by a better focusing with a microscope objective.

Materials for thin film solar cells

In a first step single layers of relevant materials for the production of thin film solar cells shall be characterized. The active area materials, different kinds of silicon thin films, are of special interest. In a second step the feasibility of pump probe measurements on stacks with several silicon layers shall be investigated.

Silicon microstructures

Microstructures which can act as a focusing and/or as a detection tool for mechanical waves shall be investigated numerically and experimentally. Based on first experiments of Profunser [60] the specimens of interest are tip like silicon microstructures. For the numerical investigations a 3-dimensional code for orthotropic structures must be implemented. For the measurements of these microstructures with dimensions of some microns the pump probe setup must be enhanced regarding the maximum time window of a measurement and regarding the lateral resolution.

1.2 Outline of this thesis

The thesis is divided in four main chapters: Theory and modeling, experimental setup, results, and conclusions and outlook.

Laser acoustics: Theory and modelling

In chapter 2 the theory and principles of the laser acoustic pump probe technique are discussed. All presented theoretical models are numerically implemented in order to have a complete simulation tool. The relevant processes of a pump probe measurement can be split into three parts: The excitation of the mechanical waves, the wave propagation in the specimen, and the detection of the mechanical waves. The excitation of the mechanical waves is done by very short laser pulses with a duration in the range of 100 fs. For the description of such fast diffusion processes the 1-dimensional two temperature model presented by Qiu et al. [63] is used. The wave propagation in thin films is modeled with a 1-dimensional viscoelastic material model in order to account for the attenuation of the mechanical waves, Bryner et al. [10]. The detection of the mechanical waves is described with a model based on the photoelastic relation between strain and dielectric constant. In addition to the above mentioned 1-dimensional models, a 3-dimensional model is presented and validated for the description of wave propagation phenomena in orthotropic microstructures as for example silicon tips, Bryner et al. [11].

Experimental setup

Chapter 3 describes the experimental setup. It is based on the setup of Profunser [60], which is called 'Basic setup' in the following. Therefore the most important parts of the basic setup are described first. Afterwards the enhancements, which are necessary for the new kinds of specimens, are presented and explained: The collinear beam guidance with the microscope objective, the camera, and the improved delay line with retroreflectors. Additionally, typical characteristics of a pump probe measurement curve are discussed by means of a measurement of an aluminum thin film.

Results

In chapter 4 the results are presented. First, the attenuations in aluminum films deposited with different methods are investigated and compared.

Afterwards, polymers used for nanoimprint lithography are analyzed regarding the bulk wave velocity and the attenuation. The influence of the thickness and the surface material of polymer specimens on the bulk wave velocity is investigated, too. Structured polymer specimens are characterized regarding their geometry. Structures with dimensions of some microns or larger are investigated by lateral scans. For smaller structures the measured resonance frequencies are taken as a characterization criterion.

Then materials used in thin film solar cells are investigated with a special interest on the active area layers consisting of different silicon films. These films are measured with the pump probe setup and additionally with nanoindentation. The nanoindentation technique and the interpretation of such measurements is discussed briefly. For microcrystalline silicon specimens the influence of the crystalline volume fraction on the mechanical properties is shown. The pump probe measurement technique is applied successfully to a stack with several silicon layers delivering thicknesses of the different layers with one measurement.

The wave propagation properties in 3-dimensional silicon microstructures are first analyzed by numerical simulations. The focusing and detection properties and the influence of the crystallographic orientation are investigated. Then pump probe measurements in silicon cantilevers and in cut silicon tips are presented.

Conclusions and outlook

The present work is summarized in chapter 5. The main results are presented and possible future directions of the project are discussed.

2 Laser acoustics: Theory and modeling

2.1 Overview

Short pulse laser acoustics is well known and widely used in the semiconductor industry, mostly for measurements on metallic specimens, e.g. interconnects of computer chips. This measurement technique as introduced by Thomsen et al. [76], [77] uses a pump-probe setup. Very short laser pulses having durations of less than 100 fs are used in order to excite and detect mechanical pulses in the specimens. The laser pulse for the excitation is called pump pulse, the laser pulse for the detection is called probe pulse. Depending on the material and the thickness of the absorbing top layer of the specimen the pump pulse generates mechanical wave packets with frequencies beyond 100 GHz. The specimens considered in this work have thicknesses in the range from 10 nm (thin films) to several microns (microstructures as for example AFM tips).

The pump pulse arriving on the surface of the specimen causes a fast temperature increase near the surface. This generates mechanical stress that starts to propagate as a bulk wave into the specimen. The wave propagation is mainly one-dimensional, as long as the spot size of the laser is much larger than the wavelength of the mechanical waves. At every interface of the specimen the waves are partly reflected thus heading back to the surface. Near the surface, the mechanical waves cause a small change of the optical reflectance at the surface. This is called the photoacoustic effect. Superimposed to the photoacoustic effect, there is also a change in the optical reflectance caused by the temperature rise at the surface. The optical reflectance, influenced by the photoacoustic effect and the temperature at the surface, is recorded by the measurement of the intensity of the reflected probe beam.

With the measurement of the optical reflectance the time of flight t_f of the bulk wave pulses through the thin film layers can be determined. If the material properties determining the bulk wave velocity c_p are known, with the time of flight the thickness d of the corresponding layer can be calculated with equation (2.1).

$$d = \frac{t_f \cdot c_p}{2} \quad (2.1)$$

Or vice versa, for a known thickness, the bulk wave velocity can be calculated with equation (2.2).

$$c_p = \frac{2d}{t_f} \quad (2.2)$$

Furthermore, by the analysis of the amplitude and the shape of the peaks in the optical reflectance data, the phonon attenuation can be determined.

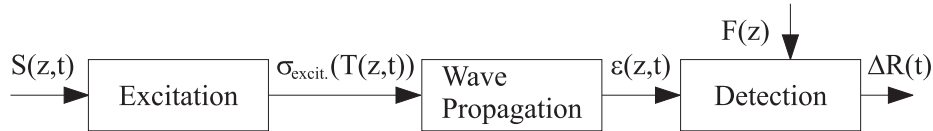


Figure 2.1: Simulation model: Laser power density S , stress σ , strain ε , reflectance change ΔR , and sensitivity function $F(z)$.

The entire laser acoustic measurement procedure can be described with a 1-dimensional model consisting of three main parts, see Fig. 2.1. The three parts are discussed in detail in the chapters 2.2, 2.3, and 2.5. 1-dimensional modeling gives good results for configurations where the diameter of the irradiated spot on the surface of the specimen is large compared to the absorption length of the laser ξ . Additionally there must be no lateral boundaries in the wave propagation area. These conditions are satisfied for the measurements investigated in sections 4.1 to 4.4. Metallic thin films have absorption lengths in the order of 10 to 20 nm (Profunser [60]) which is 2 - 3 orders of magnitude smaller than the size of the focused laser spot (4 - 40 μm).

In chapter 2.4 a 3-dimensional modeling of the wave propagation part is discussed. This approach can be used for specimens with lateral boundaries causing 3-dimensional wave patterns. Such specimens are investigated in chapter 4.5.

2.2 Excitation: Ultrashort laser pulse heating

Thomsen et al. [76] introduced a simple model for the temperature distribution in a metallic thin film after the exposure to an ultrashort laser pulse. Their model assumes that the laser intensity is constant during the duration of the laser pulse and neglects the heat diffusion and the so called hot electron diffusion within the metallic thin film. The simplicity of this model enables an analytical solution of the subsequent wave propagation equations but overestimates the peak temperatures and the temperature gradients due to the negligence of any diffusion effects (see Profunser [60]).

In this thesis the temperature distribution in the metallic top layer is calculated with the two temperature model described by Qiu et al. [63]. The two temperature model takes into account that the electron temperature and the lattice temperature are not in an equilibrium due to the fast heating process caused by the short pulse laser. This model is discussed in great detail by Profunser [60], whereas here in the following the model and its numerical implementation are introduced in a short way. More information about models for fast heating processes can be found in the book of Tzou [78].

2.2.1 Governing equations

The two temperature model consists of a nonlinear system of two equations:

$$C_e(T_e)\frac{\partial T_e}{\partial t} = \frac{\partial}{\partial z}\left(K_e(T_e)\frac{\partial T_e}{\partial z}\right) - G(T_e - T_l) + S(z, t) \quad (2.3)$$

$$C_l\frac{\partial T_l}{\partial t} = G(T_e - T_l) \quad (2.4)$$

C_e is the heat capacity of the electrons, T_e is the temperature of the electrons, t is the time, z is the spatial coordinate, K_e is the thermal conductivity, G is the electron-phonon coupling factor, T_l is the temperature of the lattice, S is the laser power density, and C_l is the heat capacity of the lattice. Since the diameter of the irradiated spot (4 - 40 μm) is at least 2 - 3 orders of magnitude larger than the penetration depth of the laser ξ , the two temperature model is solved in one dimension only with the spatial coordinate z perpendicular to the film surface.

The laser power density S is defined as

$$S(z, t) = \frac{1}{\xi}(1 - R)I_L(t)e^{-z/\xi}. \quad (2.5)$$

ξ is the absorption length of the laser in the thin film, R the optical reflectance of the thin film, and $I_L(t)$ is the intensity of the incoming laser pulse. R and ξ depend on the complex refraction index $n^* = n + i\kappa$ and are wavelength dependent. Detailed derivations of equations (2.6) and (2.7) are done by Wenke [84].

$$\xi = \frac{\lambda_L}{4\pi\kappa} \quad (2.6)$$

λ_L is the wavelength of the laser in air.

$$R = \left| \frac{n_{Air}^* - n_{Film}^*}{n_{Air}^* + n_{Film}^*} \right|^2 \quad (2.7)$$

The heat capacity $C_e(T_e)$ and conductivity $K_e(T_e)$ of the electrons are temperature dependent. A good approximation at temperatures below the Curie temperature is a linear ansatz (Tas et al. [73], Hostetler et al. [37]):

$$C_e(T_e) = \gamma T_e = \frac{C_{e0}}{T_0} T_e = \frac{T_e}{T_0} C_{e0} \quad (2.8)$$

$$K_e(T_e) = \frac{T_e}{T_l} K_{e0} \quad (2.9)$$

γ is the Grüneisen constant. Instead of using the Grüneisen constant, γ can be expressed by the electron heat capacity C_{e0} at the reference temperature T_0 (see equation (2.8)). K_{e0} in equation (2.9) is the electron heat conductivity at the temperature equilibrium $T_e = T_l$.

For the numerical simulations equations (2.3) and (2.4) are written dimensionless. Dimensionless variables are defined as:

$$\tau = t/t_0 \quad (2.10)$$

$$\chi = z/z_0 \quad (2.11)$$

$$\theta_e = T_e/T_0 \quad (2.12)$$

$$\theta_l = T_l/T_0. \quad (2.13)$$

τ is the normalized time, χ the normalized spatial coordinate, θ_e and θ_l are the normalized temperatures of the electrons and the lattice, respectively. For normalizing time t_0 and length z_0 the pulse duration t_{pulse} and the absorption length ξ are useful. Furthermore the following dimensionless constants are used:

$$C_c = C_{e0}/C_l \quad (2.14)$$

$$N = Gt_0/C_{e0} \quad (2.15)$$

$$D_e = K_{e0}/Gz_0^2 \quad (2.16)$$

C_c is the ratio of the heat capacities, N is the inverse normalized relaxation time and D_e characterizes the relation between the electron heat conductivity and the electron-phonon interaction. With equations (2.8) to (2.16), relations (2.3) and (2.4) yield

$$\frac{\partial \theta_e}{\partial \tau} = ND_e \left[\frac{1}{\theta_e \theta_l} \left(\frac{\partial \theta_e}{\partial \chi} \right)^2 - \frac{1}{\theta_l^2} \frac{\partial \theta_e \partial \theta_l^2}{\partial \chi} + \frac{1}{\theta_l} \frac{\partial^2 \theta_e}{\partial \chi^2} \right] - N \left(1 - \frac{\theta_l}{\theta_e} \right) + S \frac{t_0}{C_{e0} T_0 \theta_e} \quad (2.17)$$

$$\frac{\partial \theta_l}{\partial \tau} = NC_c \left(\theta_e - \theta_l \right). \quad (2.18)$$

For both the electrons (equation (2.17)) and the lattice (equation (2.18)) adiabatic boundary conditions are applied, thus neglecting the heat transfer into the air and the underlying layer:

$$\left. \frac{\partial \theta_e}{\partial \chi} \right|_{\chi=0} = \left. \frac{\partial \theta_e}{\partial \chi} \right|_{\chi=\frac{d_{tl}}{z_0}} = \left. \frac{\partial \theta_l}{\partial \chi} \right|_{\chi=0} = \left. \frac{\partial \theta_l}{\partial \chi} \right|_{\chi=\frac{d_{tl}}{z_0}} = 0 \quad (2.19)$$

d_{tl} is the thickness of the top metal layer. As initial conditions the dimensionless temperatures θ_e and θ_l are set to 1, meaning that all the system is at the reference temperature τ_0 before the laser heating.

2.2.2 Numerical implementation

Equations (2.17) and (2.18) are solved numerically using a finite difference code. The spatial discretization is done with second order central differences:

$$\frac{\partial \theta_k}{\partial \chi} \simeq \frac{\theta_{k+1} - \theta_{k-1}}{2\Delta\chi} \quad \frac{\partial^2 \theta_k}{\partial \chi^2} \simeq \frac{\theta_{k+1} - 2\theta_k + \theta_{k-1}}{\Delta\chi^2} \quad (2.20)$$

The index k refers to the coordinate χ . The explicit Euler scheme is used for the temporal integration:

$$\theta^{n+1} = \theta^n + \Delta\tau \cdot \frac{\partial \theta^n}{\partial \tau} \quad (2.21)$$

The index n refers to the dimensionless time τ . With equations 2.20 to 2.21, relations 2.17 and 2.18 yield

$$\begin{aligned} \theta_{e,k}^{n+1} = \theta_{e,k}^n + \Delta\tau \left[ND \left(\frac{1}{\theta_{e,k}^n \theta_{l,k}^n} \left(\frac{\theta_{e,k+1}^n - \theta_{e,k-1}^n}{2\Delta\chi} \right)^2 - \frac{1}{(\theta_{l,k}^n)^2} \frac{\theta_{e,k+1}^n - \theta_{e,k-1}^n}{2\Delta\chi} \cdot \dots \right. \right. \\ \left. \left. \dots \cdot \frac{\theta_{l,k+1}^n - \theta_{l,k-1}^n}{2\Delta\chi} + \frac{1}{\theta_{l,k}^n} \frac{\theta_{e,k+1}^n - 2\theta_{e,k}^n + \theta_{e,k-1}^n}{\Delta\chi^2} \right) - N \left(1 - \frac{\theta_{l,k}^n}{\theta_{e,k}^n} \right) + S_k^n \frac{t_0}{C_{e0} T_0 \theta_{e,k}^n} \right] \end{aligned} \quad (2.22)$$

$$\theta_{l,k}^{n+1} = \theta_{l,k}^n + \Delta\tau \left[NC_c (\theta_{e,k}^n - \theta_{l,k}^n) \right]. \quad (2.23)$$

For the numerical implementation of the adiabatic boundary conditions (2.19) a right hand side (2.24) and a left hand side (2.25) difference scheme of second order are used:

$$\frac{\partial\theta_k}{\partial\chi} \cong \frac{-3\theta_k + 4\theta_{k+1} - \theta_{k+2}}{2\Delta\chi} = 0 \quad (2.24)$$

$$\frac{\partial\theta_k}{\partial\chi} \cong \frac{3\theta_k - \theta_{k-1} + \theta_{k-2}}{2\Delta\chi} = 0 \quad (2.25)$$

This leads to the following equations for the boundary elements of the electron and the lattice temperature, respectively:

$$\theta_{e,1}^n = \frac{4}{3}\theta_{e,2}^n - \frac{1}{3}\theta_{e,3}^n \quad (2.26)$$

$$\theta_{e,end}^n = \frac{4}{3}\theta_{e,end-1}^n - \frac{1}{3}\theta_{e,end-2}^n \quad (2.27)$$

$$\theta_{l,1}^n = \frac{4}{3}\theta_{l,2}^n - \frac{1}{3}\theta_{l,3}^n \quad (2.28)$$

$$\theta_{l,end}^n = \frac{4}{3}\theta_{l,end-1}^n - \frac{1}{3}\theta_{l,end-2}^n \quad (2.29)$$

2.3 Wave propagation: 1-dimensional viscoelastic model

In this section the wave propagation in thin film specimens is described with a 1-dimensional viscoelastic model, Bryner [10]. A detailed discussion of viscoelastic models is covered by Christensen [19]. Viscoelastic models incorporate the attenuation of the mechanical waves within the thin films. Therefore they are optimally suited for the simulation of materials with a high attenuation, e.g. polymers, or for simulations of thick specimens where there is a significant attenuation due to the long travel distance of the mechanical pulses. By setting the attenuation towards zero the viscoelastic model is getting equivalent to the pure elastic model. The pure elastic model is suited for thin specimens with a low attenuation. A detailed description of the pure elastic model and its numerical implementation is given by Profunser [60].

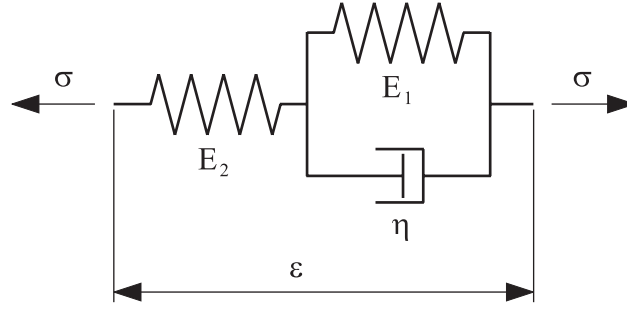


Figure 2.2: Standard linear solid.

2.3.1 Governing equations

As a viscoelastic material model the standard linear solid is used. It is represented by two Hookean springs with Young's moduli E_1 and E_2 and a Newtonian damper η . Its representation is shown in Fig. 2.2. σ is the stress, and ϵ is the strain. The dynamic behavior of a visco-elastic solid is completely defined by its creep compliance function, which looks as follows for the standard linear solid:

$$J_c(t) = \frac{E_1 + E_2}{E_1 E_2} - \frac{1}{E_1} e^{-\frac{E_1}{\eta_1} t} \quad (2.30)$$

The creep compliance function can be interpreted as the time dependent strain that is created by a stress load in form of a unit step function. The creep compliance function for the standard linear solid is plotted in Fig. 2.3, where three useful substitutions are introduced: E_0 , E_∞ , and τ_0 .

$$E_0 = E_2 \quad (2.31)$$

$$E_\infty = \frac{E_1 E_2}{E_1 + E_2} \quad (2.32)$$

$$\tau_0 = \frac{\eta_1}{E_1} \quad (2.33)$$

E_∞ can be interpreted as the Young's modulus for low frequencies ($f \ll 1/\tau_0$), E_0 can be interpreted as the Young's modulus for high frequencies ($f \gg 1/\tau_0$), and τ_0 is the time constant of the exponential creep compliance function. The frequency dependent attenuation α [1/m] in the standard linear solid can be calculated analytically from the three parameters E_0 , E_∞ , and τ_0 . This is shown in equations (2.34) to (2.37). The complex modulus E^* of a standard linear solid is defined by equation (2.34):

$$E^*(f) = E_\infty + \frac{(E_0 - E_\infty)2\pi f i}{\frac{E_0}{E_\infty \tau_0} + 2\pi f i} \quad (2.34)$$

E^* can be decomposed in a real part E' , the storage modulus, and in an imaginary part E'' , the loss modulus:

$$E^*(f) = E'(f) + iE''(f) \quad (2.35)$$

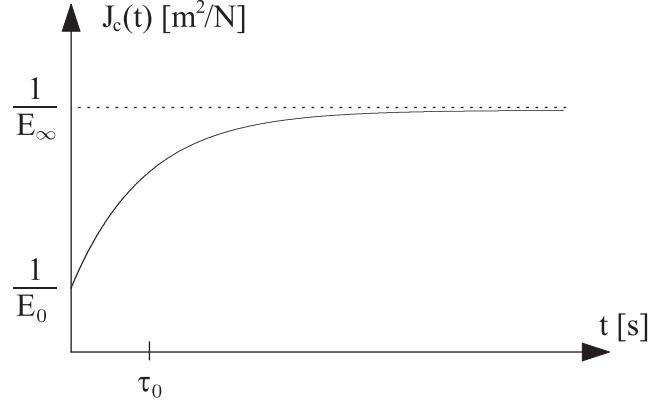


Figure 2.3: Creep compliance function of the standard linear solid.

The quality factor Q then is defined by the ratio of E' and E'' . Q corresponds to the number of wavelengths, after which a mechanical pulse has reduced its magnitude by a factor of e^π .

$$Q(f) = \frac{E'(f)}{E''(f)} = \frac{E_0 + E_\infty \tau_0^2 (2\pi f)^2}{(E_0 - E_\infty) \tau_0 2\pi f} \quad (2.36)$$

The attenuation α is directly related to the quality factor by equation (2.37):

$$\alpha(f) = \sqrt{\frac{\rho}{E'(f)} \frac{\pi f}{Q(f)}} \quad (2.37)$$

For the 1-dimensional wave propagation in thin films a uniaxial strain state is assumed. For this reason in the following considerations the Young's moduli of the standard linear solid, E_0 and E_∞ , are replaced by the corresponding p-wave moduli \bar{E}_0 and \bar{E}_∞ . The relation between p-wave modulus and Young's modulus is given in equation 2.38:

$$\bar{E} = \frac{E(1 - \nu)}{(1 + \nu)(1 - 2\nu)} \quad (2.38)$$

ν is the Poisson's ratio. In the following all parameters related to the bulk wave modulus are denoted by a bar. The 1-dimensional wave propagation in a standard linear solid is described by the following three equations:

$$\frac{\partial v}{\partial t} = \frac{1}{\rho} \frac{\partial \sigma}{\partial z} \quad (2.39)$$

$$\varepsilon = \frac{\partial u}{\partial z} \quad (2.40)$$

$$\varepsilon(t) = \bar{J}_c(0)\sigma(t) + \int_0^t \dot{\bar{J}}_c(t)\sigma(t - \tau)d\tau + \frac{1 + \nu}{1 - \nu} \alpha_{th} \Delta T_l \quad (2.41)$$

ρ is the mass density, u is the displacement, v is the velocity, α_{th} is the thermal expansion coefficient, and ΔT_l is the difference between the lattice temperature T_l and the reference temperature T_0 . Equation (2.39) is Newton's equation, equation (2.40) is the kinematic relation, and equation (2.41) is the constitutive law for viscoelastic materials with the excitation term by temperature increase. It is assumed

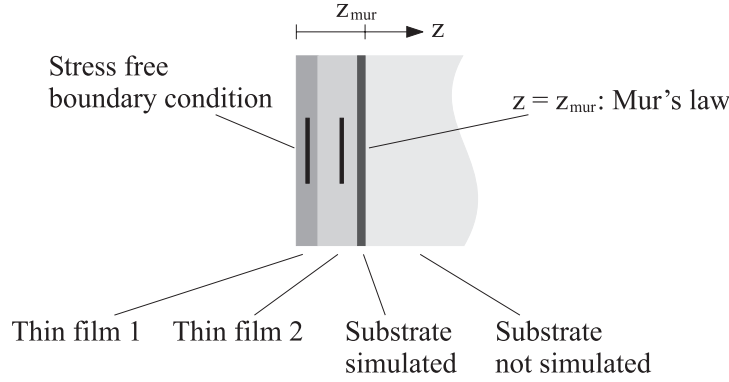


Figure 2.4: Typical specimen with two thin film layers and the substrate: The simulated part of the substrate is only some nanometers thick.

that the only nonzero component of the strain tensor is in z -direction, see Fig. 2.4. At the surface of the specimen the stress free boundary condition is applied:

$$\sigma_{z=0} = 0 \quad (2.42)$$

Since the substrate of thin film specimens usually is some orders of magnitude thicker than the thin film layers, the waves in the substrate are not reflected from the back of the substrate to the surface of the specimen during the time window of a measurement. So in order to save computation time, for the substrate the wave propagation is calculated only in the first nanometers, see Fig. 2.4. At the back of these first nanometers, at position $z = z_{mur}$, a fully absorbing boundary condition is applied, which is modeled by the Mur's law (Taflove and Hagness [72]). The Mur's law is given by

$$\left. \frac{\partial v}{\partial t} \right|_{z=z_{mur}} = c_p \left. \frac{\partial v}{\partial z} \right|_{z=z_{mur}}, \quad (2.43)$$

where c_p is the bulk wave velocity.

As initial condition all variables are set to zero: The velocity v , the stress σ , and the memory variable Ψ . Ψ is described in chapter 2.3.2.1.

2.3.2 Numerical implementation

Equation (2.39) can be directly solved numerically by using finite differences. Equations (2.40) and (2.41) are solved together with the piecewise-linear recursive convolution method as described by Taflove and Hagness [72]. Taflove and Hagness use this method to calculate the dynamic response of the electric field intensity to a changing electric flux density in Debye media. From the mathematical point of view this relation is modeled the same way as the relation between mechanical stress and strain in the standard linear solid.

2.3.2.1 Discretization

For the discretization finite differences on a staggered grid in space and time are used. Using the staggered grid in Fig. 2.5 equation (2.39) can be spatially discretized with

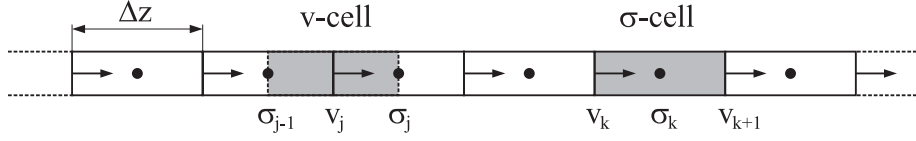


Figure 2.5: Staggered grid for the spatial discretization. The stress grid points are marked with filled circles, the velocity grid points are marked with arrows.

central differences:

$$\frac{\partial v_j}{\partial t} \cong \frac{1}{\rho} \frac{\sigma_j - \sigma_{j-1}}{\Delta z} \quad (2.44)$$

Δz is the spatial step, the subscript j denotes the spatial position $j\Delta z$. For the integration in time also a formulation based on a staggered grid is used similar to Schubert et al. [67] with a time step Δt :

$$\frac{\partial v^n}{\partial t} \cong \frac{v^{n+1/2} - v^{n-1/2}}{\Delta t} \quad (2.45)$$

The superscript n denotes the time step $n\Delta t$. Inserting equation (2.44) in (2.45) yields the explicit scheme for the calculation of the velocity v :

$$v_j^{n+1/2} = v_j^{n-1/2} + \frac{\Delta t}{\rho \Delta z} (\sigma_j^n - \sigma_{j-1}^n) \quad (2.46)$$

Equations (2.40) and (2.41) are discretized with the piecewise-linear recursive convolution method following the derivations in Taflove and Hagness [72] using the staggered grid in Fig. 2.5. This leads to the following equations:

$$\begin{aligned} \sigma_k^{n+1} = \frac{1}{\bar{J}_c(0) - \bar{A}^0 + \dot{\bar{J}}_c^0} \cdot \left[(\bar{J}_c(0) - \bar{A}^0) \sigma_k^n + \frac{\Delta t}{\Delta z} (v_{k+1}^{n+1/2} - v_k^{n+1/2}) \right. \\ \left. + \Psi_k^n - \frac{1+\nu}{1-\nu} \alpha_{th} (\Delta T_{l,k}^{n+1} - \Delta T_{l,k}^n) \right] \end{aligned} \quad (2.47)$$

$$\Psi_k^{n+1} = (\Delta \dot{\bar{J}}_c^0 - \Delta \bar{A}^0) \sigma_k^{n+1} + \Delta \bar{A}^0 \sigma_k^n + e^{-\Delta t \bar{E}_1 / \eta} \Psi_k^n \quad (2.48)$$

The subscript k denotes the spatial position $k\Delta z$, Ψ is a memory variable which is calculated recursively at every time step. $\bar{J}_c(0)$, \bar{A}^0 , $\dot{\bar{J}}_c^0$, $\Delta \dot{\bar{J}}_c^0$, and $\Delta \bar{A}^0$ are constants with the following definitions:

$$\bar{J}_c(0) = 1/\bar{E}_2 \quad (2.49)$$

$$\bar{A}^0 = \frac{\eta}{\bar{E}_1^2 \Delta t} \left[1 - \left(\frac{\Delta t \bar{E}_1}{\eta} + 1 \right) e^{-\Delta t \bar{E}_1 / \eta} \right] \quad (2.50)$$

$$\dot{\bar{J}}_c^0 = \frac{1}{\bar{E}_1} \left(1 - e^{-\Delta t \bar{E}_1 / \eta} \right) \quad (2.51)$$

$$\Delta \dot{\bar{J}}_c^0 = \frac{1}{\bar{E}_1} \left(1 - e^{-\Delta t \bar{E}_1 / \eta} \right)^2 \quad (2.52)$$

$$\Delta \bar{A}^0 = \frac{\eta}{\bar{E}_1^2 \Delta t} \left[1 - \left(\frac{\Delta t \bar{E}_1}{\eta} + 1 \right) e^{-\Delta t \bar{E}_1 / \eta} \right] \left(1 - e^{-\Delta t \bar{E}_1 / \eta} \right) \quad (2.53)$$

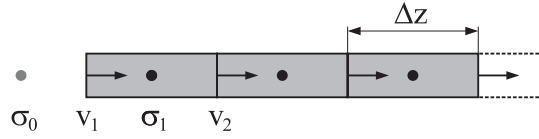


Figure 2.6: Staggered grid for the spatial discretization: Situation at the boundary. The stress grid points are marked with filled circles, the velocity grid points are marked with arrows.

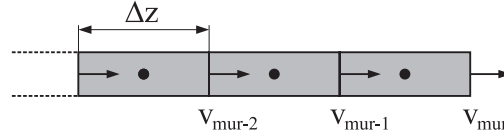


Figure 2.7: Staggered grid for the spatial discretization: Situation at the position where Mur's law is applied. The stress grid points are marked with filled circles, the velocity grid points are marked with arrows.

2.3.2.2 Boundary conditions

Stress free boundary

The staggered grid is chosen in a way that the physical boundary is positioned on a velocity grid point, see Fig. 2.7. For the calculation of v_1 a ghost point σ_0 is introduced. The stress free boundary condition is implemented by linear interpolation as follows:

$$\sigma_0 = -\sigma_1 \quad (2.54)$$

With equation (2.54) inserted in (2.44) the velocity on the boundary is then calculated as follows:

$$\frac{\partial v_1}{\partial t} \cong \frac{2\sigma_1}{\rho\Delta z} \quad (2.55)$$

Mur's law

In order to save computation time at position $z = z_{mur}$ the Mur's law is implemented, see equation (2.43). It is discretized using the left hand side difference scheme of second order, see equation (2.25):

$$\frac{\partial v_{mur}}{\partial t} \cong c_p \frac{-3v_{mur} + 4v_{mur-1} - v_{mur-2}}{2\Delta z} \quad (2.56)$$

2.3.2.3 Stability conditions

The mechanical waves must be sampled sufficiently in the space domain to minimize the errors of the numerical dispersion. For a purely elastic code Schubert et al. [67] proposed that the shortest relevant wavelength λ_{min} should be sampled at least eight times in order to keep the numerical dispersion at a reasonably low level:

$$\Delta z \leq \frac{1}{8}\lambda_{min} \quad (2.57)$$

Since in the standard linear solid the wave propagation is physically dispersive (depending on the frequency range) it is even more important to minimize the numerical dispersion. Otherwise there is no possibility to distinguish between the physically relevant and the numerical dispersion. To be on the safe side Δz is chosen typically more than 10 times smaller than demanded by formula 2.57.

The maximum allowed time step for a numerical stable code is related to Δz and the highest wave velocity $c_{p,max}$, Fellingner [32]:

$$\Delta t \leq \frac{\Delta z}{c_{p,max}} \quad (2.58)$$

For the viscoelastic code there has to be paid attention to the fact, that the bulk wave velocity is frequency dependent with the maximum value for frequencies towards infinity. So the maximum value of the bulk wave velocity $c_{p,max}$ which must be used in equation 2.58 is related to \bar{E}_0 , see also explanations in chapter 2.3.1:

$$c_{p,max} = \sqrt{\frac{\bar{E}_0}{\rho}} \quad (2.59)$$

2.3.3 Frequency dependence of bulk wave velocity and attenuation

The standard linear solid has three independent parameters by which the frequency dependent behavior regarding the bulk wave velocity and the attenuation can be influenced and adapted to the measurements. The three parameters are used to tune first the storage modulus \bar{E}' (determines the bulk wave velocity) at the frequency of interest, second the attenuation α , and third the frequency dependent characteristics of the storage modulus and the attenuation. In Fig. 2.8 three parameter sets are presented for a given storage modulus \bar{E}'_{Fit} to fit and a given attenuation α_{Fit} to fit at the frequency f_{Fit} . By choosing a very large \bar{E}_2 and a small τ_0 for the frequency $f_{Fit} \ll 1/\tau_0$ a Kelvin-Voigt like behavior is achieved (solid lines in Fig. 2.8) which exhibits a constant storage modulus and a quadratic attenuation behavior (because of the double logarithmic plot a straight line with a certain slope represents a quadratic behaviour). By choosing a very small \bar{E}_1 and a large τ_0 for the frequency $f_{Fit} \gg 1/\tau_0$ a Maxwell fluid like behavior is achieved which exhibits a constant storage modulus and a constant attenuation (dotted line in Fig. 2.8). The dashed line in Fig. 2.8 represents an intermediate case.

2.4 Wave propagation: 3-dimensional model

There are various motivations for the investigation of the 3-dimensional wave propagation in microstructures, Bryner et al. [11]: A first motivation is, that a microscopic focusing tip can act as an acoustic lense, in order to improve the lateral resolution of Pump-Probe measurements, see Profunser et al. [61]. The optimization of such a focussing tip with lateral boundaries requires the 3-dimensional simulation of the wave propagation within the tip. A second motivation is that the Pump-Probe technique

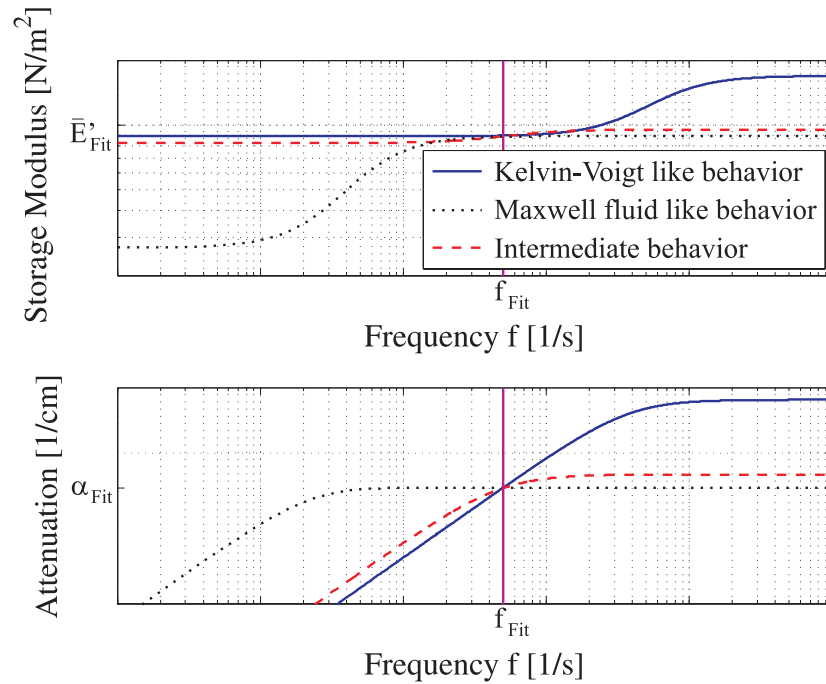


Figure 2.8: Frequency dependent properties of the standard linear solid for three parameter sets (double logarithmic plots). Upper diagram: Storage modulus \bar{E}' . Lower diagram: Attenuation α . The solid line represents a Kelvin-Voigt like behavior for frequencies from 0 to the order of f_{Fit} . The dotted line represents a Maxwell fluid like behavior for frequencies from the order of f_{Fit} to ∞ .

could also be used for measurements, e.g. for quality inspection, of 3-dimensional structures with arbitrary geometries, like MEMS components. A quantitative interpretation of such measurements demands the calculation of the wave propagation in the specimen. Additionally, a numerical, 3-dimensional code which provides access to the full temporal evolution of all relevant quantities like stresses, velocities, and displacements, is helpful for the investigation of general wave propagation phenomena, also in arbitrary, finite geometries. For example, it could be applied to the examination of phenomena in orthotropic structures where in the past a lot of work has been done by Every and Sachse, analytically, numerically, and experimentally [27], [31], [29], [30], [28].

Silicon is a probable candidate for the material of a microscopic focusing tip mentioned above and a widely used material for MEMS components. Since single crystal silicon has cubic orthotropic material properties, the wave propagation is simulated for these materials. For the simulations the Velocity Stress Finite Difference Time Domain method (VS-FDTD) on a staggered grid is used. This method with a staggered grid for mechanical waves was presented 1976 by Madariaga for an axisymmetric two-dimensional case [48]. In 1984 and 1986 Virieux investigated the SH- and P-SV-wave propagation with a staggered two-dimensional VS-FDTD formulation for geophysical problems [80], [81]. In 1988 Temple presented a 3-dimensional numerical model where the PDEs for the displacement were directly discretized [75]. Here the 3-dimensional case is solved with the VS-FDTD method using a staggered grid, which is taken from Fellingner [32]. The VS-FDTD approach gives direct access

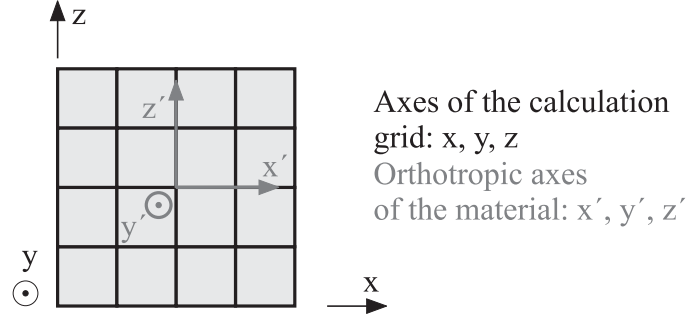


Figure 2.9: Orientation of the calculation axes and the orthotropic axes of the material.

to both, the displacement components and the stress components.

2.4.1 Governing equations

The orthotropic axes of the considered silicon structure are chosen to be parallel to the calculation axes, see Fig. 2.9. This leads to the following stiffness coefficient tensor, here written in Voigts notation, which determines the constitutive equations (2.64) - (2.69):

$$\begin{bmatrix}
 C_{11} & C_{12} & C_{12} & 0 & 0 & 0 \\
 C_{12} & C_{11} & C_{12} & 0 & 0 & 0 \\
 C_{12} & C_{12} & C_{11} & 0 & 0 & 0 \\
 0 & 0 & 0 & C_{44} & 0 & 0 \\
 0 & 0 & 0 & 0 & C_{44} & 0 \\
 0 & 0 & 0 & 0 & 0 & C_{44}
 \end{bmatrix} \quad (2.60)$$

The wave propagation is described by the equations of motion,

$$\rho \dot{v}_x = \frac{\partial T_{xx}}{\partial x} + \frac{\partial T_{xy}}{\partial y} + \frac{\partial T_{xz}}{\partial z}, \quad (2.61)$$

$$\rho \dot{v}_y = \frac{\partial T_{xy}}{\partial x} + \frac{\partial T_{yy}}{\partial y} + \frac{\partial T_{yz}}{\partial z}, \quad (2.62)$$

$$\rho \dot{v}_z = \frac{\partial T_{xz}}{\partial x} + \frac{\partial T_{yz}}{\partial y} + \frac{\partial T_{zz}}{\partial z}, \quad (2.63)$$

the constitutive equations in Voigt notation,

$$\dot{T}_{xx} = C_{11} \dot{\epsilon}_{xx} + C_{12} (\dot{\epsilon}_{yy} + \dot{\epsilon}_{zz}) + \dot{g}_{xx}, \quad (2.64)$$

$$\dot{T}_{yy} = C_{11} \dot{\epsilon}_{yy} + C_{12} (\dot{\epsilon}_{xx} + \dot{\epsilon}_{zz}) + \dot{g}_{yy}, \quad (2.65)$$

$$\dot{T}_{zz} = C_{11} \dot{\epsilon}_{zz} + C_{12} (\dot{\epsilon}_{xx} + \dot{\epsilon}_{yy}) + \dot{g}_{zz}, \quad (2.66)$$

$$\dot{T}_{yz} = 2C_{44} \dot{\epsilon}_{yz} + \dot{g}_{yz}, \quad (2.67)$$

$$\dot{T}_{xz} = 2C_{44}\dot{\varepsilon}_{xz} + \dot{g}_{xz}, \quad (2.68)$$

$$\dot{T}_{xy} = 2C_{44}\dot{\varepsilon}_{xy} + \dot{g}_{xy}, \quad (2.69)$$

and the kinematic relations,

$$\dot{\varepsilon}_{pq} = \frac{1}{2}(v_{p,q} + v_{q,p}). \quad (2.70)$$

v_p , T_{pq} , and ε_{pq} with $p, q = x, y, z$ are the cartesian components of the particle velocity vector and that of the stress and strain tensor, respectively. g_{pq} are the stress excitation terms. The dots denote the time derivatives. The material properties are described by C_{11} , C_{12} , and C_{44} , the three independent components of the stiffness tensor in Voigts notation, and the density ρ . Substituting the kinematic relations into the constitutive equations leads to the following six equations:

$$\dot{T}_{xx} = C_{11}\frac{\partial v_x}{\partial x} + C_{12}\left(\frac{\partial v_y}{\partial y} + \frac{\partial v_z}{\partial z}\right) + \dot{g}_{xx} \quad (2.71)$$

$$\dot{T}_{yy} = C_{11}\frac{\partial v_y}{\partial y} + C_{12}\left(\frac{\partial v_x}{\partial x} + \frac{\partial v_z}{\partial z}\right) + \dot{g}_{yy} \quad (2.72)$$

$$\dot{T}_{zz} = C_{11}\frac{\partial v_z}{\partial z} + C_{12}\left(\frac{\partial v_x}{\partial x} + \frac{\partial v_y}{\partial y}\right) + \dot{g}_{zz} \quad (2.73)$$

$$\dot{T}_{yz} = C_{44}\left(\frac{\partial v_y}{\partial z} + \frac{\partial v_z}{\partial y}\right) + \dot{g}_{yz} \quad (2.74)$$

$$\dot{T}_{xz} = C_{44}\left(\frac{\partial v_x}{\partial z} + \frac{\partial v_z}{\partial x}\right) + \dot{g}_{xz} \quad (2.75)$$

$$\dot{T}_{xy} = C_{44}\left(\frac{\partial v_x}{\partial y} + \frac{\partial v_y}{\partial x}\right) + \dot{g}_{xy} \quad (2.76)$$

With the nine equations (2.61) - (2.63) and (2.71) - (2.76) the wave propagation is completely described for the case that the orthotropic axes of the material are parallel to the coordinate directions x , y , and z .

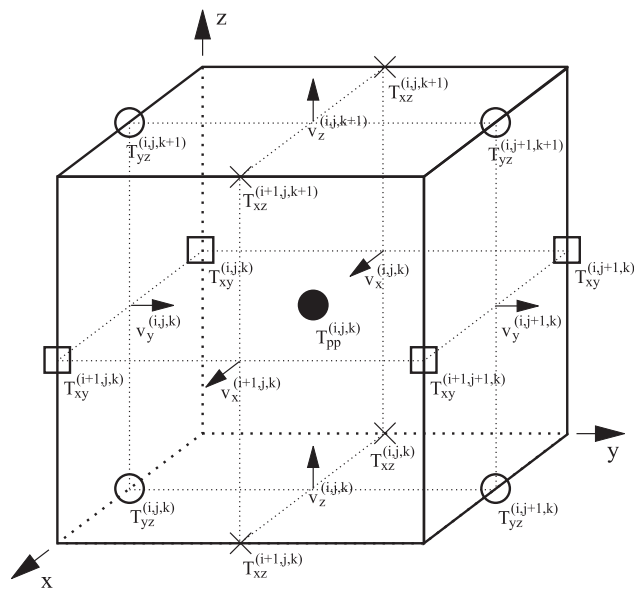
2.4.2 Numerical implementation

2.4.2.1 Discretization

The discretization is done using a staggered grid as described by Fellingner [32]. In Fig. 2.10 the position of the different components is illustrated. The unit cell with the edge lengths Δx , Δy , and Δz is chosen such that the normal stresses are in the middle of the cell, the shear stresses are in the middle of the edges, and the velocities are in the middle of the surfaces. Correspondingly a structure with $I \times J \times K$ unit cells (I , J , K are the numbers of unit cells in x , y , z -direction, respectively) has the dimensions of the different gridpoint matrices presented in Table 2.1. With

Matrix	Dimension
T_{xx}	$I \times J \times K$
T_{yy}	$I \times J \times K$
T_{zz}	$I \times J \times K$
T_{yz}	$I \times (J + 1) \times (K + 1)$
T_{xz}	$(I + 1) \times J \times (K + 1)$
T_{yx}	$(I + 1) \times (J + 1) \times K$
v_x	$(I + 1) \times J \times K$
v_y	$I \times (J + 1) \times K$
v_z	$I \times J \times (K + 1)$

Table 2.1: Dimensions of the gridpoint matrices for the different variables.


 Figure 2.10: Unit cell for the discretization at the position $x = i$, $y = j$, $z = k$.

this staggered grid the PDEs can be discretized in a second order approximation by central differences with respect to the spatial coordinates x , y , and z . The nine spatially discretized equations are:

$$\begin{aligned} \dot{T}_{xx(i,j,k)} &= C_{11} \frac{v_x(i+1,j,k) - v_x(i,j,k)}{\Delta x} + \\ C_{12} &\left(\frac{v_y(i,j+1,k) - v_y(i,j,k)}{\Delta y} + \frac{v_z(i,j,k+1) - v_z(i,j,k)}{\Delta z} \right) + \dot{g}_{xx(i,j,k)} \end{aligned} \quad (2.77)$$

$$\begin{aligned} \dot{T}_{yy(i,j,k)} &= C_{11} \frac{v_y(i,j+1,k) - v_y(i,j,k)}{\Delta y} + \\ C_{12} &\left(\frac{v_x(i+1,j,k) - v_x(i,j,k)}{\Delta x} + \frac{v_z(i,j,k+1) - v_z(i,j,k)}{\Delta z} \right) + \dot{g}_{yy(i,j,k)} \end{aligned} \quad (2.78)$$

$$\begin{aligned} \dot{T}_{zz(i,j,k)} &= C_{11} \frac{v_z(i,j,k+1) - v_z(i,j,k)}{\Delta z} + \\ C_{12} &\left(\frac{v_y(i,j+1,k) - v_y(i,j,k)}{\Delta y} + \frac{v_x(i+1,j,k) - v_x(i,j,k)}{\Delta x} \right) + \dot{g}_{zz(i,j,k)} \end{aligned} \quad (2.79)$$

$$\dot{T}_{yz(i,j,k)} = C_{44} \left(\frac{v_z(i,j,k) - v_z(i,j-1,k)}{\Delta y} + \frac{v_y(i,j,k) - v_y(i,j,k-1)}{\Delta z} \right) + \dot{g}_{yz(i,j,k)} \quad (2.80)$$

$$\dot{T}_{xz(i,j,k)} = C_{44} \left(\frac{v_z(i,j,k) - v_z(i-1,j,k)}{\Delta x} + \frac{v_x(i,j,k) - v_x(i,j,k-1)}{\Delta z} \right) + \dot{g}_{xz(i,j,k)} \quad (2.81)$$

$$\dot{T}_{xy(i,j,k)} = C_{44} \left(\frac{v_y(i,j,k) - v_y(i-1,j,k)}{\Delta x} + \frac{v_x(i,j,k) - v_x(i,j-1,k)}{\Delta y} \right) + \dot{g}_{xy(i,j,k)} \quad (2.82)$$

$$\rho \dot{v}_x(i,j,k) = \frac{T_{xx(i,j,k)} - T_{xx(i-1,j,k)}}{\Delta x} + \frac{T_{xy(i,j+1,k)} - T_{xy(i,j,k)}}{\Delta y} + \frac{T_{xz(i,j,k+1)} - T_{xz(i,j,k)}}{\Delta z} \quad (2.83)$$

$$\rho \dot{v}_y(i,j,k) = \frac{T_{yy(i,j,k)} - T_{yy(i,j-1,k)}}{\Delta y} + \frac{T_{xy(i+1,j,k)} - T_{xy(i,j,k)}}{\Delta x} + \frac{T_{yz(i,j,k+1)} - T_{yz(i,j,k)}}{\Delta z} \quad (2.84)$$

$$\rho \dot{v}_z(i,j,k) = \frac{T_{zz(i,j,k)} - T_{zz(i,j,k-1)}}{\Delta z} + \frac{T_{xz(i+1,j,k)} - T_{xz(i,j,k)}}{\Delta x} + \frac{T_{yz(i,j+1,k)} - T_{yz(i,j,k)}}{\Delta y} \quad (2.85)$$

The lower indices i, j, k denote the spatial steps Δx , Δy , and Δz . According to Schubert [67] an explicit scheme is used for the temporal integration. For each time step Δt , the results are calculated by equations (2.77) - (2.85) and second order central differences in the time domain which leads to a staggered grid in time, too:

$$v_p^n = v_p^{n-1} + \dot{v}_p^{n-\frac{1}{2}} \Delta t \quad (2.86)$$

$$T_{pq}^{n+\frac{1}{2}} = T_{pq}^{n-\frac{1}{2}} + \dot{T}_{pq}^n \Delta t \quad (2.87)$$

The upper index n denotes the number of time steps Δt .

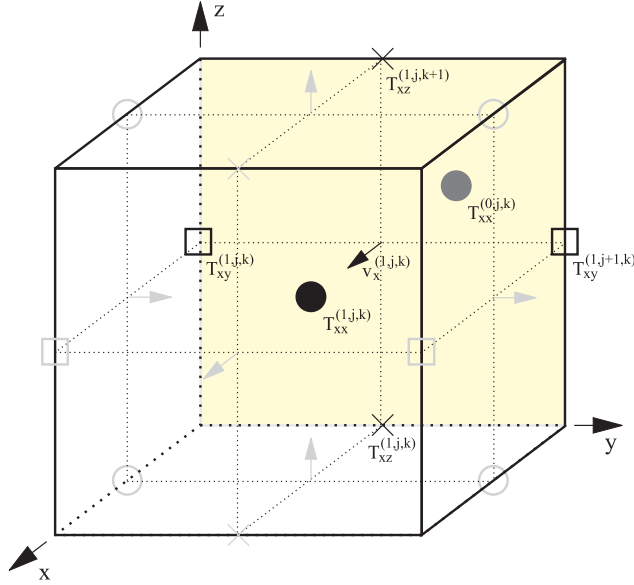


Figure 2.11: Situation at the boundary $i = 1$: involved grid points for the calculation of v_x , according to equation (2.88).

2.4.2.2 Boundary conditions

If not mentioned otherwise, the simulations are calculated with the stress free boundary conditions described in this chapter. Using the unit cell shown in Fig. 2.10 there are no grid points for the normal stresses on the surface. So equations (2.77) - (2.79) need no special consideration regarding the boundary conditions. The values of the shear stress grid points at the boundary surfaces are directly set to zero instead of using equations (2.80) - (2.82). This is the case for the T_{yz} -components at boundary planes parallel to the xy - and the xz -plane, for the T_{xz} -components at boundary planes parallel to the xy - and the yz -plane, and for the T_{xy} -components at boundary planes parallel to the xz - and the yz -plane.

The calculation of the velocity grid points at the boundary surfaces requires some modifications of equations (2.83) - (2.85). The missing values for the normal stress components are replaced with so called ghost points. This is explained for the calculation of the v_x -component at the position $(i = 1, j, k)$, see Fig. (2.11). Equation (2.83) applied for this position looks as follows:

$$\rho \dot{v}_x(1,j,k) = \frac{T_{xx}(1,j,k) - T_{xx}(0,j,k)}{\Delta x} + \frac{T_{xy}(1,j+1,k) - T_{xy}(1,j,k)}{\Delta y} + \frac{T_{xz}(1,j,k+1) - T_{xz}(1,j,k)}{\Delta z} \quad (2.88)$$

The ghost point $T_{xx}(0,j,k)$, which is outside of the simulated area, is set to the value of $-T_{xx}(1,j,k)$. Like this, the actual boundary condition is guaranteed, i.e. the interpolated value of T_{xx} on the surface is equal to zero. As mentioned before, the shear stress components at the boundaries are equal to zero. With these assumptions equation (2.88) can be simplified:

$$\rho \dot{v}_x(1,j,k) = \frac{2T_{xx}(1,j,k)}{\Delta x} \quad (2.89)$$

In the same way the other equations for the velocities at the boundaries are derived:

$$\rho\dot{v}_{x(I+1,j,k)} = -\frac{2T_{xx(I,j,k)}}{\Delta x} \quad (2.90)$$

$$\rho\dot{v}_{y(i,1,k)} = \frac{2T_{yy(i,1,k)}}{\Delta y} \quad (2.91)$$

$$\rho\dot{v}_{y(i,J+1,k)} = -\frac{2T_{yy(i,J,k)}}{\Delta y} \quad (2.92)$$

$$\rho\dot{v}_{z(i,j,1)} = \frac{2T_{zz(i,j,1)}}{\Delta z} \quad (2.93)$$

$$\rho\dot{v}_{z(i,j,K)} = -\frac{2T_{zz(i,j,K+1)}}{\Delta z} \quad (2.94)$$

2.4.2.3 Stability conditions

The numerical errors can be separated into phase errors and amplitude errors (Leutenegger [46]). The first group of errors is called numerical dispersion and is related to the spatial discretization. The numerical dispersion cannot be eliminated but reduced to an acceptable level by decreasing the lateral step sizes. Schubert et al. [67] proposed that the shortest wavelength should be sampled at least eight times in order to keep the numerical dispersion at a reasonably low level. Applying this criterion to the present 3-dimensional case leads to the following condition:

$$\sqrt{\Delta x^2 + \Delta y^2 + \Delta z^2} \leq \frac{1}{8} \lambda_{min} \quad (2.95)$$

λ_{min} denotes the shortest wavelength. In case that the lateral step sizes are identical in x-, y-, and z-direction equation (2.95) can be simplified to

$$\Delta x \leq \frac{\sqrt{3}}{24} \lambda_{min}. \quad (2.96)$$

The second group of errors are the amplitude errors. If the time step Δt is too big compared to Δx , Δy , and Δz , the calculated amplitudes increase exponentially, the code then becomes unstable. The maximum allowed time step for a stable 3-dimensional code for isotropic material is calculated by Fellingner [32]:

$$\Delta t \leq \frac{1}{c_p \sqrt{\frac{1}{\Delta x^2} + \frac{1}{\Delta y^2} + \frac{1}{\Delta z^2}}} \quad (2.97)$$

c_p denotes the velocity of the primary waves. Again, this equation can be simplified in case of identical lateral step sizes in x-, y-, and z-direction and isotropy:

$$\Delta t \leq \frac{\Delta x}{\sqrt{3}c_p} \quad (2.98)$$

For orthotropic materials equation (2.98) is still valid, if c_p is replaced by c_{po} , the velocity of the fastest primary wave:

$$\Delta t \leq \frac{\Delta x}{\sqrt{3}c_{po}}. \quad (2.99)$$

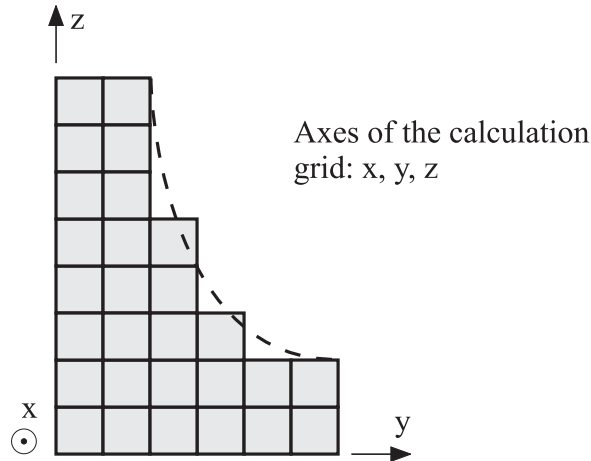


Figure 2.12: Step-like approximation of the stress-free boundary conditions to the 'real' geometry (dashed line).

2.4.2.4 Structures with arbitrary shapes

The numerical code discussed above is based on a cartesian calculation grid. So the simplest applications of this code are block-shaped structures. In order to simulate the wave propagation in other structures, their geometry is approximated by steps. In this manner it is possible to calculate arbitrary geometries with the numerical code presented above. A schematic example of the step-like approximation is illustrated in Fig. 2.12. The accuracy of the step-like approximation is related to the ratio between the wave length of the considered wave packets and the size of the steps. The step size of the approximation should be smaller at least one order of magnitude than the wavelength of the considered wave packets.

2.4.3 Validation

For the validation of the numerical code, first the wave velocities are compared with analytical values. In a second step, the energy within the simulated cube is considered. For these two considerations in the chapters 2.4.3.1 and 2.4.3.2 3-dimensional simulations of the wave propagation in a silicon cube with side lengths of 400 nm are performed. The material properties for silicon are taken from Royer et al. [65]: $C_{11} = 165.6$ GPa, $C_{12} = 63.9$ GPa, $C_{44} = 79.5$ GPa, $\rho = 2329$ kg / m^3 . The temporal shape of the stress excitation is one sinusoidal oscillation at 80 GHz multiplied with a Hanning window. It is plotted in Fig. 2.13. The spatial discretization is done with a step size of 2 nm in the three cartesian directions. The temporal discretization is done with a step size of 0.1 ps which satisfies the stability condition given in equation (2.99) taking the value of 9354 m/s for c_{po} (see table 2.2). In chapter 2.4.3.3 simulation results for waves with large wavelengths in pyramidal structures are compared with the results of an analytical model. The parameters used for these considerations are described in chapter 2.4.3.3.

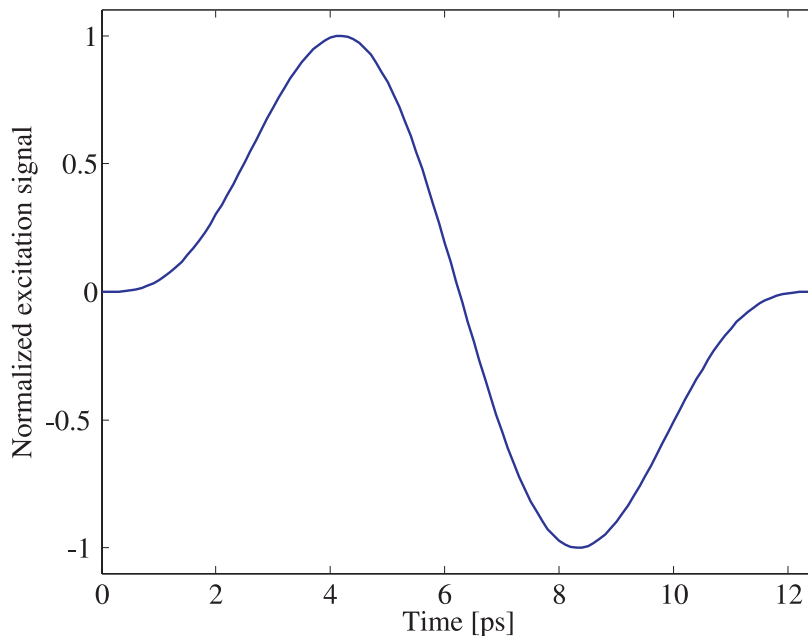


Figure 2.13: Normalized stress excitation signal for the considerations in the chapters 2.4.3.1 and 2.4.3.2.

2.4.3.1 Wave velocities

In a cubic orthotropic medium the velocities of plane waves vary depending on their propagation directions and polarizations. In Table 2.2 the analytically calculated velocities for seven different cases are listed (formulas taken from Royer et al. [65]). For all three considered propagation directions [100], [110], and [111], the group velocities and the phase velocities are the same. For the [100] and the [110] directions this is shown in Fig. 2.14: The group velocities \underline{v}_G are by definition at all points normal to the slowness curves. The points generating the slowness curves correspond to the inverted group velocities. For the [100] and the [110] direction they are parallel to the corresponding propagation directions \underline{n} and equal to the phase velocities. In order to validate the numerical code, the seven cases in Table 2.2 are simulated numerically. The excited layers have to be chosen perpendicular to the propagation direction of interest according to Fig. 2.15. On these layers the excitation is carried out, weighting the different stress components in a way that the polarization of the resulting plane wave is according to the seven cases in Table 2.2. These stress excitation components are listed in Table 2.3.

For two reference points $P1$ and $P2$ along the corresponding propagation direction (step 1 in Fig. 2.16), the temporal evolution of the displacement in direction of the corresponding polarization is calculated (step 2 in Fig. 2.16). With the cross correlation of these two signals, the shift of the arrival times at the two reference points is calculated (step 3 in Fig. 2.16). With the shift of the arrival times and the known positions of the reference points, the corresponding wave velocities are determined (step 4 in Fig. 2.16). In Fig. 2.16 the procedure is shown for the calculation of the velocity for case 1. The velocities of the other cases are determined accordingly. They are listed in Table 2.3 and agree well with the analytically calculated

Case	Propagation direction	Polarization	Formula	Velocity for Si
1	[100]	[100]	$\sqrt{\frac{c_{11}}{\rho}}$	8432 m/s
2	[100]	(100) plane	$\sqrt{\frac{c_{44}}{\rho}}$	5843 m/s
3	[110]	[110]	$\sqrt{\frac{c_{11}+c_{12}+c_{44}}{2\rho}}$	9133 m/s
4	[110]	$[1\bar{1}0]$	$\sqrt{\frac{c_{11}-c_{12}}{2\rho}}$	4673 m/s
5	[110]	[001]	$\sqrt{\frac{c_{44}}{\rho}}$	5843 m/s
6	[111]	[111]	$\sqrt{\frac{c_{11}+2c_{12}+4c_{44}}{3\rho}}$	9354 m/s
7	[111]	(111) plane	$\sqrt{\frac{c_{11}-c_{12}+c_{44}}{3\rho}}$	5093 m/s

Table 2.2: Listing of the reference cases and the corresponding analytically calculated velocities.

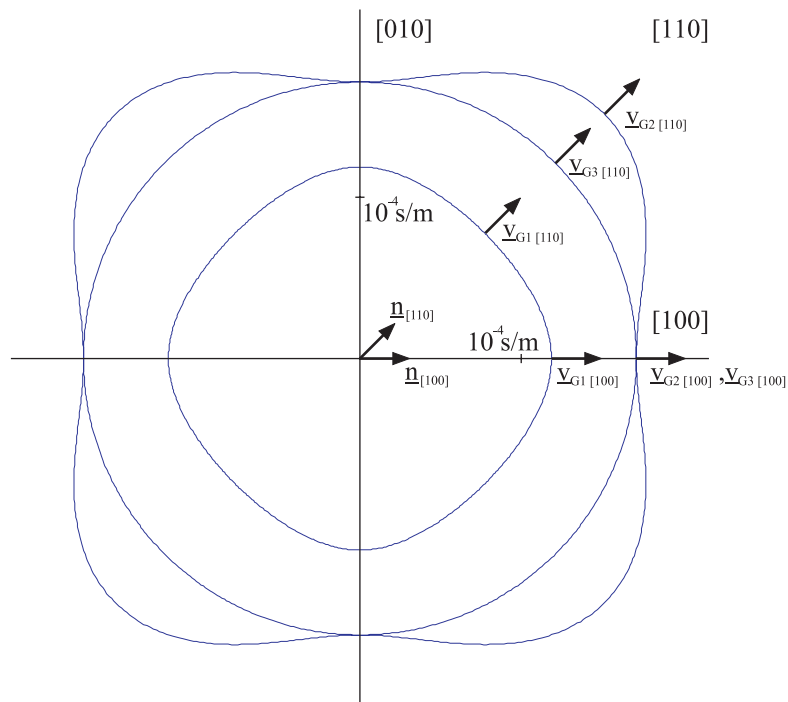


Figure 2.14: Slowness curves for silicon: The group velocities \underline{v}_G are parallel to the corresponding propagation directions \underline{n} for the [100] and [110] direction, and equal to the phase velocities.

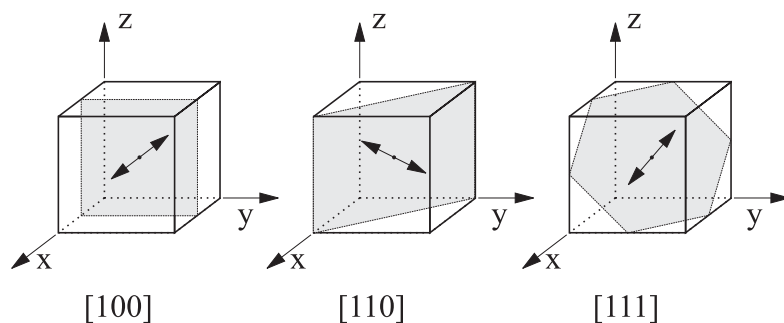


Figure 2.15: Excited layers for the wave propagation in the [100], [110], and [111] direction, respectively.

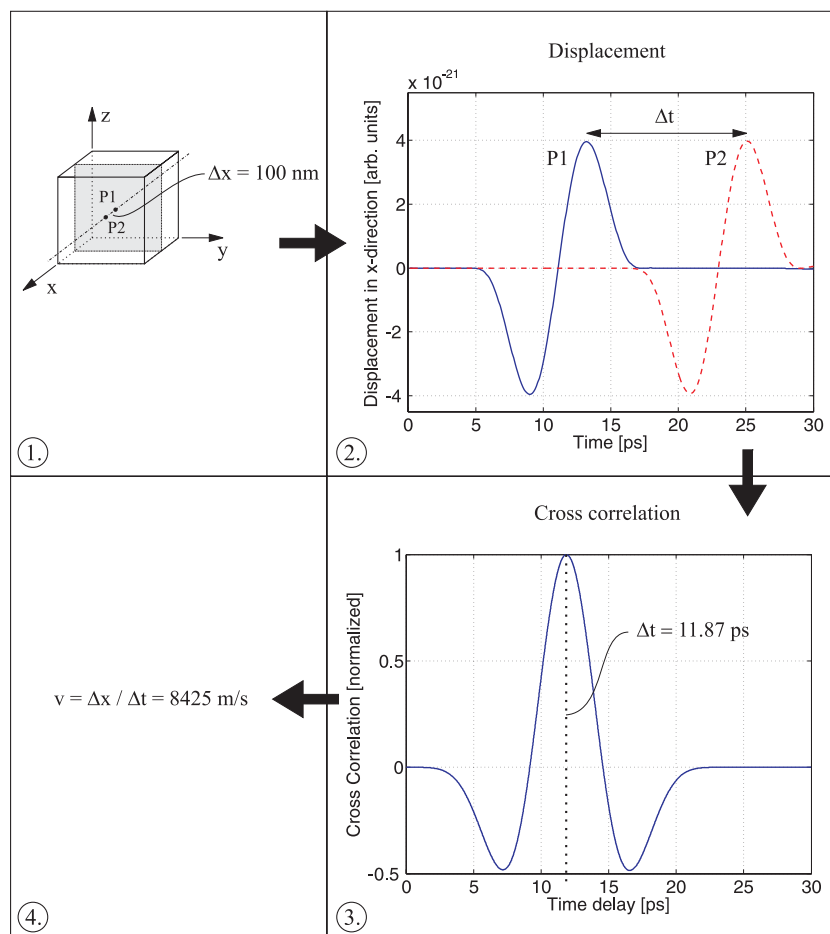


Figure 2.16: Determination of the velocity for the case 1. Step 1: Definition of two reference points. Step 2: Calculation of their displacement curves. Step 3: Calculation of the cross correlation. Step 4: Calculation of the velocity.

Case	g_{xx}	g_{yy}	g_{zz}	g_{yz}	g_{xz}	g_{xy}	Velocity from num. simulation	Deviation to analytical result
1	1	0	0	0	0	0	8425 m/s	0.08%
2	0	0	0	0	0	1	5845 m/s	0.03%
3	$\frac{1}{2}$	$\frac{1}{2}$	0	0	0	$\frac{1}{2}$	9130 m/s	0.03%
4	1	-1	0	0	0	0	4663 m/s	0.21%
5	0	0	0	$\frac{1}{\sqrt{2}}$	$\frac{1}{\sqrt{2}}$	0	5808 m/s	0.60%
6	1	1	1	0	0	0	9368 m/s	0.15%
7	$\frac{1}{\sqrt{2}}$	$\frac{1}{\sqrt{2}}$	$-\sqrt{2}$	0	0	0	5087 m/s	0.12%

Table 2.3: Numerical simulation: Values of the stress excitation components, the numerically calculated velocities, and the deviations to the analytically calculated velocities of table 2.2.

velocities in Table 2.2. The maximum deviation is less than 0.6%.

2.4.3.2 Energy

Since the presented numerical code is nondissipative, the energy is used as a criterion in order to validate the code. Neglecting material damping and radiation loss, the total energy remains constant after the excitation is terminated. Monitoring the energy level during the entire simulation represents a necessary condition for the numerical accuracy. The total energy E is given by the sum of the kinetic energy E_{kin} and the potential energy E_{pot}

$$E = E_{kin} + E_{pot}. \quad (2.100)$$

The kinetic energy is given by

$$E_{kin} = \frac{1}{2}\rho \int \int \int v_p v_p dV, \quad (2.101)$$

and the potential energy is given by

$$E_{pot} = \frac{1}{2} \int \int \int T_{pq} \varepsilon_{pq} dV. \quad (2.102)$$

Repeated indices are summed up in equations (2.101) and (2.102). For the numerical calculation of the energy it is assumed that the velocities, stresses, and strains are constant within a unit cell (see Fig. 2.10). While the normal stress components are directly calculated at the center of the unit cells (see Fig. 2.10), the other components are linearly interpolated for the center point. The velocity component in x-direction at the center of the unit cell (i, j, k) is denoted by v_{xC} and calculated as follows:

$$v_{xC(i,j,k)} = \frac{v_{x(i,j,k)} + v_{x(i+1,j,k)}}{2} \quad (2.103)$$

The other missing velocity components at the center, v_{yC} and v_{zC} are calculated accordingly.

With these velocity components, the discretized kinetic energy in the unit cell (i, j, k) at time n is calculated:

$$E_{kin(i,j,k)}^n = \frac{1}{2} \rho (v_{pC(i,j,k)}^n)^2 \Delta x \Delta y \Delta z \quad (2.104)$$

For the calculation of the potential energy, the shear stress components have to be interpolated at the center of the unit cell. This is shown for the T_{yz} -component:

$$T_{yzC(i,j,k)} = \frac{T_{yz(i,j,k)} + T_{yz(i,j+1,k)} + T_{yz(i,j,k+1)} + T_{yz(i,j+1,k+1)}}{4} \quad (2.105)$$

The other missing shear stress components at the center, $T_{xzC(i,j,k)}$ and $T_{xyC(i,j,k)}$ are calculated accordingly.

The strain components ε_{xxC} , ε_{yyC} , ε_{zzC} , ε_{yzC} , ε_{xzC} , and ε_{xyC} are calculated from the stress components with the inverted constitutive equations 2.64-2.69. Like this, the discretized potential energy in the unit cell (i, j, k) at time $n + \frac{1}{2}$ is calculated as follows:

$$E_{pot(i,j,k)}^{n+\frac{1}{2}} = \frac{1}{2} (T_{pqC(i,j,k)}^{n+\frac{1}{2}}) (\varepsilon_{pqC(i,j,k)}^{n+\frac{1}{2}}) \Delta x \Delta y \Delta z \quad (2.106)$$

The corresponding potential energy at time n is derived by linear interpolation in time:

$$E_{pot(i,j,k)}^n = \frac{E_{pot(i,j,k)}^{n+\frac{1}{2}} + E_{pot(i,j,k)}^{n-\frac{1}{2}}}{2} \quad (2.107)$$

The total energy then is calculated by the summation over all unit cells of the kinetic and the potential energy:

$$E_{tot}^n = \sum_{i=1}^I \sum_{j=1}^J \sum_{k=1}^K E_{kin(i,j,k)}^n + E_{pot(i,j,k)}^n \quad (2.108)$$

The energy plot of the simulation of case 2 (see Table 2.2) is shown in Fig. 2.17: total energy (solid line), kinetic energy (dashed line), and potential energy (dotted line). During the excitation in the first 12 ps the total energy increases, afterwards it remains at a constant level. When waves are reflected at the boundaries, there are interchanges between the kinetic and potential energies after approximately 40 ps. During these interchanges a weak ripple in the total energy can be seen (circle in Fig. 2.17), which is not expected for physical reasons. According to Gsell [36] these ripples are due to the approximation of a constant energy within the grid cells. They vanish when smaller grid cells are chosen.

Also a long term simulation has also been performed for 100000 time steps, which correspond to 10 ns, in order to verify that the total energy remains constant. Within these 100000 time steps, in case 2 the waves travel more than 140 times through the cube with the sidelength of 400 nm. A linear regression analysis of the total energy in this simulation estimates an decrease of negligible 0.000013% of the total energy after a simulated period of 10 ns.

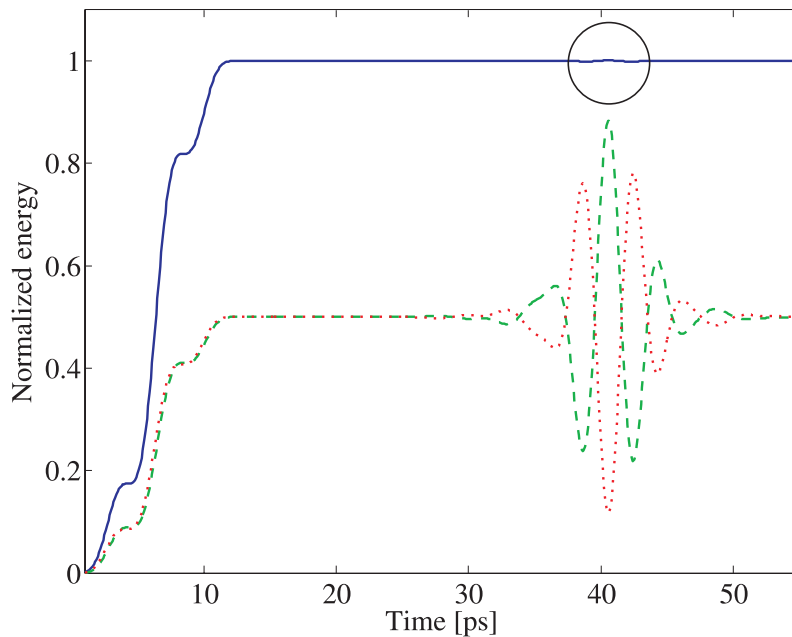


Figure 2.17: Temporal evolution of the energy in Case 2 for the first 55 ps: total energy (solid line), kinetic energy (dashed line), and potential energy (dotted line).

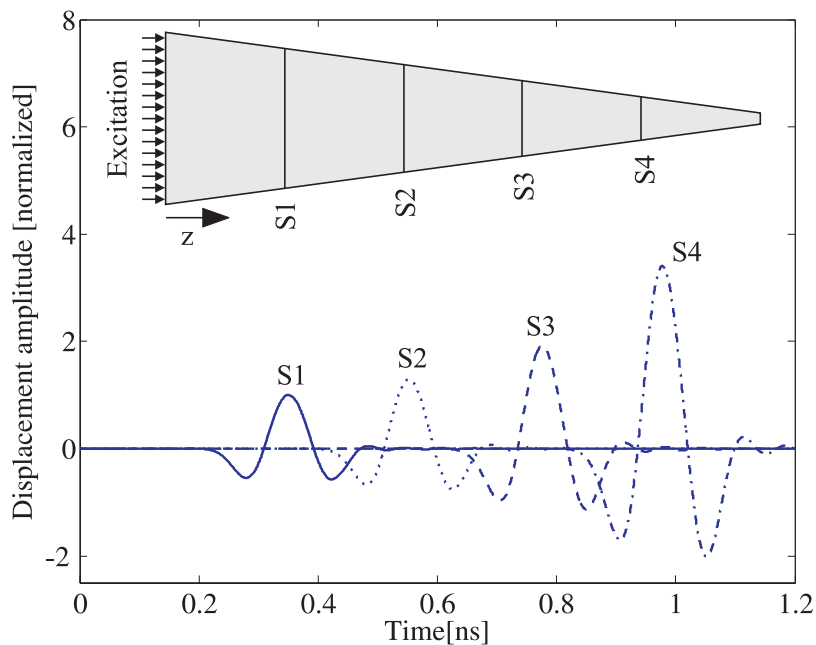


Figure 2.18: Upper part: Sketch with the excitation at the base surface and the four sections. Lower part: Numerically calculated displacement amplitudes in z -direction in the cross-sections S1-S4.

Section number	Side length	Norm. ampl. analytical	Norm. ampl. numerical	Deviation
1	158 nm	1	1	reference section
2	122 nm	1.295	1.291	0.31 %
3	82 nm	1.927	1.914	0.67 %
4	46 nm	3.435	3.408	0.79 %

Table 2.4: Validation for long wavelengths: Comparison between analytically calculated and numerically simulated displacement amplitudes for the cross-sections shown in Fig. 2.18.

2.4.3.3 Long wavelengths

In this chapter the wave propagation in a long pyramidal structure (base length $0.2 \mu\text{m}$, length $8 \mu\text{m}$) is considered. Numerical results are compared with a simplified analytical model for large wavelengths and isotropic materials taken from Graff [35]. Assuming a uniform stress distribution within the cross section, this model predicts the displacement amplitudes for longitudinal waves in horn shaped geometries with slight cross-sectional variations. In this theory the displacement amplitudes are inversely proportional to the square root of the cross-section area and thus inversely proportional to the side length of the cross-section. 3-dimensional effects are neglected. For the numerical simulation the pyramidal shape is approximated in a step-like manner as described in chapter 2.4.2.4. An isotropic material is chosen: $C_{11} = 165.6 \text{ GPa}$, $C_{12} = 63.9 \text{ GPa}$, $C_{44} = 0.5(C_{11} - C_{12})$, $\rho = 2329 \text{ kg/m}^3$. The spatial discretization is done with a step size of 2 nm in the three cartesian directions, the temporal discretization is done with a time step of 10^{-13} s . The temporal shape of the stress excitation is one sinusoidal oscillation at 4 GHz multiplied with a Hanning window. The excitation takes place at the base surface where a uniform normal stress in z-direction is applied (see Fig. 2.18 upper part). The wavelength of the excited waves is in the order of $2 \mu\text{m}$ which is large compared to the lateral dimensions of the structure. In four different cross-sections the numerically simulated displacement amplitudes are compared with the analytical model of Graff [35]. In Table 2.4 the analytically calculated and the numerically calculated displacement amplitudes are compared. For both of the calculations the values are normalized to the amplitude in cross-section 1. There is a good agreement between the analytically and the numerically calculated amplitudes with deviations of less than 1 %. In the lower part of Fig. 2.18 the numerically calculated displacement amplitudes in z-direction are plotted for the four sections S1-S4. Small dispersion effects can be seen (non-symmetrical shape of the displacement amplitudes). These effects are caused by the variable cross-section and the lateral-inertia which are incorporated implicitly in the numerical code presented in this paper, while neglected in the approximate analytical solution.

2.5 Detection: Change of reflectance

The 1-dimensional theory described in this chapter gives a relation between the spatially distributed strain in a metallic thin film caused by the mechanical waves and the change in the optical reflectance on the surface of the thin film measured by pump-probe measurements. The change in temperature due to the laser heating also influences the optical reflectance. But in the pump-probe measurements the contribution of the temperature changes can well be subtracted because the thermal diffusion process has a time constant which is much larger than the duration of the mechanical pulses. So the thermal contribution is not considered in this chapter. The theory described in this chapter is mainly based on a paper of Thomsen et al. [76] and discussed in detail by Wenke [84]. The relation between strain and reflectance can be split in two parts which are discussed in the following.

- The relation between a specific change of the dielectric constant $\Delta\epsilon^*$ at the depth z' on the reflectance R at the surface.
- The relation of a plane strain distribution $\varepsilon(z, t)$ and the dielectric constant $\epsilon^*(z, t)$.

For the following considerations it is assumed that the refraction index of air is equal to the value in vacuum: $n_{air} = n_{vac} = 1$. The refraction index of the metallic film $n_{film}^* = n_{film} + ik_{film}$ is a complex number indicated by the asterisk.

2.5.1 Relation between dielectric constant and reflectance

To get the influence of a specific change of the dielectric constant at the depth z' , $\Delta\epsilon$ is put to $\delta(z - z')$, where δ is the dirac function. The electromagnetic wave (i.e. the laser pulse) running in the film is partially reflected at this discontinuity of $\epsilon^*(z, t)$ with the following reflection coefficient r' (Thomsen [76]):

$$r' = \frac{ik_{vac}^2}{2k_{film}^*} \quad (2.109)$$

k_{vac} and k_{film}^* are the wave numbers of the electromagnetic wave in the air and in the film, respectively. The relation between the amplitude of an incoming electromagnetic wave E_{In} and the part of the wave which is reflected at the discontinuity of the dielectric constant $E_{R\Delta\epsilon}$ is then given by

$$E_{R\Delta\epsilon} = t_{vf}t_{fv}r' \cdot e^{2i\omega n_{film}^*z'/c_0} \cdot E_{In} =: \Delta r_s(z') \cdot E_{In}. \quad (2.110)$$

ω is the circular frequency of the electromagnetic wave and c_0 is the speed of light in vacuum. t_{vf} is the transmission coefficient from vacuum into the film and t_{fv} vice versa. They are defined as follows:

$$t_{vf} = \frac{2}{1 + n_{film}^*} \quad (2.111)$$

$$t_{fv} = \frac{2n_{film}^*}{1 + n_{film}^*} \quad (2.112)$$

$\Delta r_s(z')$ is the reflectivity change caused by a discontinuity of the dielectric constant at $z = z'$. To get the whole reflectivity change Δr of a distribution $\Delta\epsilon^*(z, t)$ equation (2.110) has to be integrated over the space domain:

$$\Delta r = t_{vf} t_{fv} r' \int_0^\infty e^{2i\omega n^* z'/c_0} \cdot \Delta\epsilon^*(z', t) \cdot dz' \quad (2.113)$$

The reflectance change ΔR is then calculated as follows:

$$\Delta R = |r_0 + \Delta r|^2 - |r_0|^2 \quad (2.114)$$

r_0 is the reflectivity in case of no perturbation:

$$r_0 = \frac{1 - n_{film}^*}{1 + n_{film}^*} \quad (2.115)$$

Equations (2.109), (2.111), and (2.112) with $k_{vac} = \omega/c_0$ and $k_{film}^* = n_{film}^* \omega/c_0$ inserted in equation (2.113) and then inserted with (2.115) in (2.114) yield the complete expression for the reflectance change:

$$\Delta R = \left| \frac{1 - n^*}{1 + n^*} + \frac{2i\omega}{c_0 \cdot (1 + n^*)^2} \cdot \int_0^\infty e^{2i\omega n^* z'/c_0} \cdot \Delta\epsilon^*(z', t) dz' \right|^2 - \left| \frac{1 - n^*}{1 + n^*} \right|^2 \quad (2.116)$$

2.5.2 Relation between strain and dielectric constant

The influence of mechanical strain ε on the dielectric constant ϵ^* is also known as photoelastic behaviour. The linearized photoelastic behaviour is characterized by the following terms (Thomsen et al. [76]):

$$\Delta\epsilon^*(z, t) \cong \frac{\partial(n^*)^2}{\partial\varepsilon} \Big|_{\varepsilon=0} \cdot \varepsilon(z, t) = 2n^* \cdot \left[\frac{\partial n}{\partial\varepsilon} \Big|_{\varepsilon=0} + i \frac{\partial \kappa}{\partial\varepsilon} \Big|_{\varepsilon=0} \right] \cdot \varepsilon(z, t) \quad (2.117)$$

$\partial n/\partial\varepsilon$ and $\partial \kappa/\partial\varepsilon$ are called the photoelastic constants. Inserting equation (2.117) in equation (2.116) yields a direct relation between strain distribution and reflectance change:

$$\Delta R = \left| \frac{1 - n_{film}^*}{1 + n_{film}^*} + \frac{4i\omega n_{film}^*}{c_0(1 + n_{film}^*)^2} \int_0^\infty e^{2i\omega n_{film}^* z/c_0} \left[\frac{\partial n}{\partial\varepsilon} \Big|_{\varepsilon=0} + i \frac{\partial \kappa}{\partial\varepsilon} \Big|_{\varepsilon=0} \right] \varepsilon(z, t) dz \right|^2 - \left| \frac{1 - n_{film}^*}{1 + n_{film}^*} \right|^2 \quad (2.118)$$

Equation 2.118 can be linearized for the strain ε which leads to a compact formulation (Thomsen [76]):

$$\Delta R \cong \int_0^\infty f(z) \varepsilon(z, t) dz \quad (2.119)$$

where

$$f(z) = f_0 \left[\frac{\partial n}{\partial\varepsilon} \sin\left(\frac{2\omega n z}{c_0} - \psi\right) + \frac{\partial \kappa}{\partial\varepsilon} \cos\left(\frac{2\omega n z}{c_0} - \psi\right) \right] e^{-z/\xi} \quad (2.120)$$

with

$$f_0 = \frac{8\omega\sqrt{n^2(n^2 + \kappa^2 - 1)^2 + \kappa^2(n^2 + \kappa^2 + 1)^2}}{c_0[(n + 1)^2 + \kappa^2]^2} \quad (2.121)$$

and

$$\psi = \arctan \left[\frac{\kappa(n^2 + \kappa^2 + 1)}{n(n^2 + \kappa^2 - 1)} \right] \quad (2.122)$$

In equations (2.120) to (2.122) n and k are the real part and the imaginary part of the refractive index of the film. ξ is the absorption length according to equation (2.6). $f(z)$ is called the sensitivity function. It determines how strain at different depths below the surface contributes to the change in the reflectance.

3 Experimental setup

For the laser acoustic measurements a collinear pump probe setup is used. It is based on the pump probe setup presented in very detail by Profunser [60], which is called "basic setup" in the following. In order to have the most important information in one place the basic setup it is described shortly in chapter 3.1. More details can be found in the publications of Profunser [60] and Vollmann et al. [82]. The measurements presented in in this thesis are all carried out with an enhanced setup which is called "collinear setup" in the following. In chapter 3.2 the enhancements of the collinear setup and the motivations for them are discussed.

3.1 Basic setup

3.1.1 Overview

The pump probe setup described in this chapter was built up by Profunser [60] and Vollmann et al. [82]. A schematic sketch with the most important components is shown in Fig. 3.1. A pulse laser generates very short light pulses with a duration of less than 100 fs, with a repetition rate of 81 MHz, and with an optical wavelength of 800 nm. The maximum average power is 1 W. By a beam splitter, the laser beam is separated into a pump beam (90% of the energy) and a probe beam (10% of the energy), which are used for the excitation and detection of acoustic pulses in the specimen. A translation table with two mirrors (see Fig. 3.1) is used as a delay line in the optical path of the pump beam. This enables a very precise control of the shift between the arrival times of the pump and the probe beam at the surface of the specimen. Moving the translation table 1 μm corresponds to a change in the time shift of 6.7 fs between the pump and the probe pulse. Both the pump and the probe beam are focused on the same spot on the surface of the specimen by convex lenses. The diameter of the focused beams on the surface is estimated to be in the order of 100 μm , Profunser [60]. The light of the probe beam reflected at the surface of the specimen is collected with a collimator and transmitted by a fibre to the photo-detector. The photo detector measures the intensity of the reflected probe beam.

3.1.2 Noise reduction

Since the quantity to be measured, the optical reflectance change, is very small, the goal of the experimental setup is to maximize the signal to noise ratio. This is mainly done by three arrangements.

- Double modulation of pump and probe beam

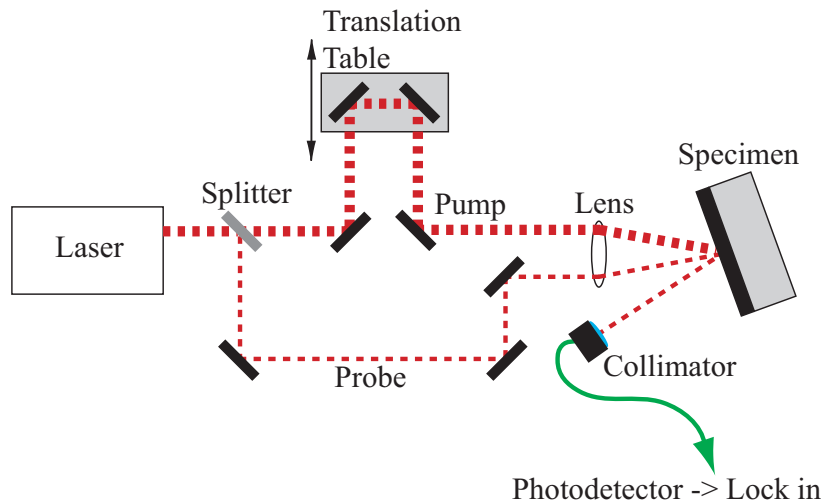


Figure 3.1: Main components of the basic pump probe setup (figure taken from Profunser [60]).

- Cross polarization of pump and probe beam
- Balanced photodetector

3.1.2.1 Double modulation

The pump beam is harmonically modulated by an electro optical modulator with a frequency of 19 MHz. The probe beam is modulated by a mechanical chopper in the order of 400 Hz. Both frequencies are used for the double lock-in amplification, which is discussed in detail by Profunser [60].

3.1.2.2 Cross polarization

In order to reduce optical cross-talk, the polarization of the probe beam is turned around 90 degrees by a $\lambda/2$ plate, see Fig. 3.2. Doing so, the probe beam is horizontally polarized whereas the pump beam remains vertically polarized. A filter in front of the collimator of the probe beam reflected at the specimen suppresses disturbing influences of scattered light of the pump beam.

3.1.2.3 Balanced photodetector

The reflected probe beam is filtered and collected with a collimator. The light is transmitted to the balanced photodetector by a single mode fiber. The second input of the balanced photodetector collects the light of the reference probe beam, which is not affected by the reflectance change at the surface of the specimen. The intensities of these two probe pulses are equalized by a variable neutral density filter (NDF) before the experiment is started. Doing so, only the difference of their intensities is amplified by the photodetector. With this configuration the measured and amplified signal of the photodetector is caused by the reflectance change only and fluctuations of the laser (caused by the laser for instance) are strongly reduced.

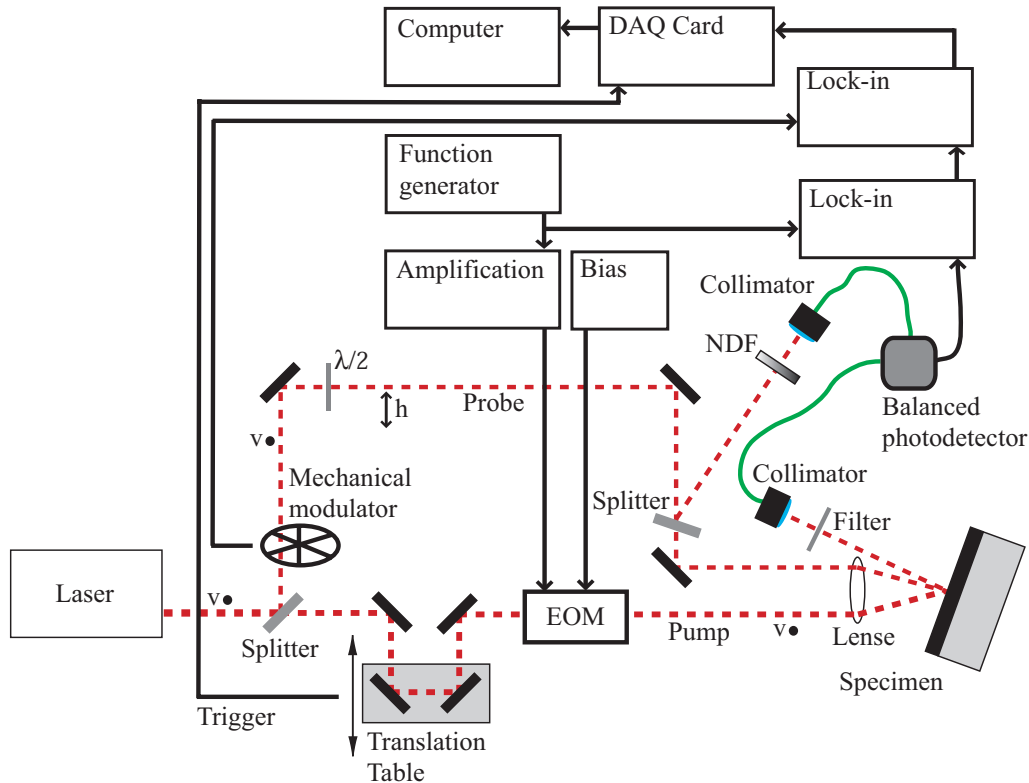


Figure 3.2: Basic setup in detail (figure taken from Profunser [60]).

3.2 Collinear setup

All pump probe measurements presented in this thesis are carried out with an extended setup, the collinear setup, which is described in the following. There are three main motivations for the enhancements of the collinear setup:

- In the basic setup the focus points of the laser beams have a diameter in the order of $100 \mu\text{m}$. This diameter is sufficiently small for measurements of planar structures like thin films. For measurements of microstructures with features or lateral dimensions in the order of some microns, a better focusing is needed.
- The beam walking of the pump beam must be reduced. The beam walking is mainly caused by an imperfect adjustment of the two mirrors on the translation table. If they are not perfectly adjusted, the outgoing beam gets a parallel offset depending on the position of the translation table. The offset changes the overlap between pump and probe beam during the measurement. This disturbing effect increases with increasing travel distance of the translation table and decreasing size of the focal spot of the laser beams.
- The maximum time window of the setup is determined by the travel distance of the delay line which has a length of 250 mm. Therefore the monitoring of the wave propagation is limited to a maximum time window of 1.67 ns in the basic setup. This time window is not large enough for the measurement of waves in silicon structures with thicknesses larger than $7 \mu\text{m}$.

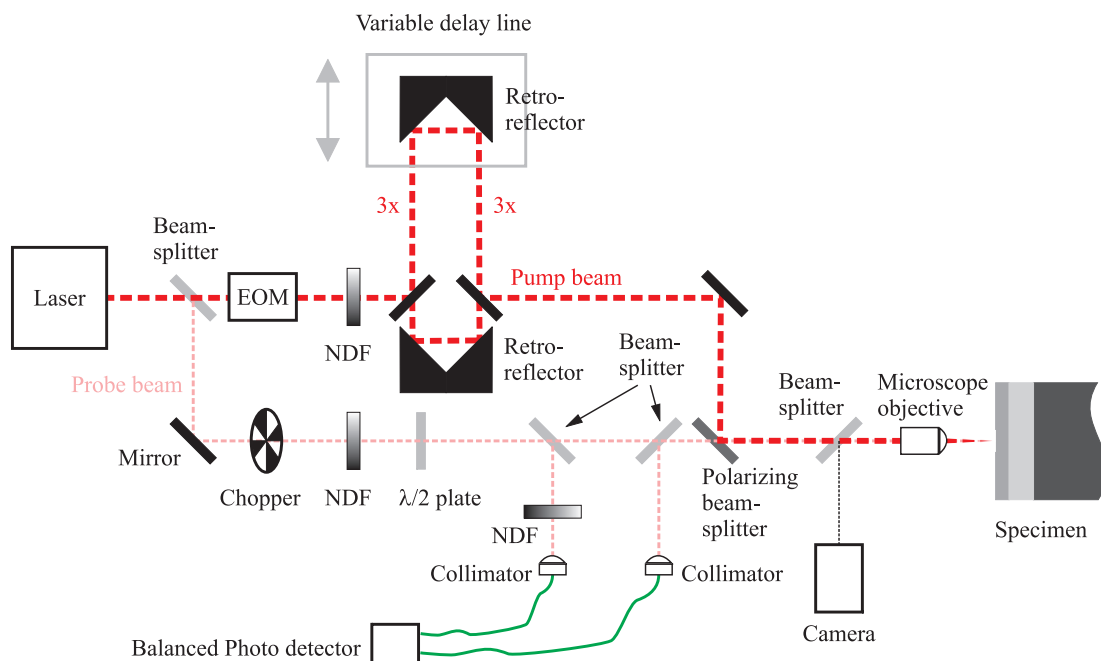


Figure 3.3: Layout of the collinear setup. NDF: Neutral density filter.

3.2.1 Beam guidance

In order to achieve a better focusing, the convex lenses of the basic setup are replaced by a microscope objective. With a 20x objective the laser beam can be focused to a diameter in the range of estimated 3-5 μm . Since the working distance of such objectives is in the range of 3 mm, it is no longer possible to work with individual objectives for the pump and the probe beam as it is done in the basic setup. Therefore a collinear beam guidance is used where for the pump and the probe beams the same objective is used, see Fig. 3.3. As in the basic setup, the pump and probe beam are separated first in order to introduce a variable time delay, cross polarization, and two different modulations. Then the two beams are realigned using a polarizing beam splitter as shown in Fig. 3.3 and Fig. 3.4 on the right. Due to the better focusing it is necessary to attenuate the beams with two neutral density filters (NDF). Typical values for the average power used with the 20x objective are 10 mW for the pump beam and 2 mW for the probe beam. For a similar pump beam intensity (38 mW average power, spot size diameter 20 μm) Morath et al. [54] estimate a very low steady state heating of the specimens of less than 5 K at ambient temperatures above 80 K.

The features for the noise reduction are still the same ones as in the basic setup: Double modulation, cross polarization, and a balanced photodetector.

3.2.2 Camera

With spot sizes in the order of 3-5 μm it is no longer possible to align the pump and the probe beams without the help of a camera. Therefore a commercial webcam is coupled into the beam path using a simple microscope slide as beam splitter, see

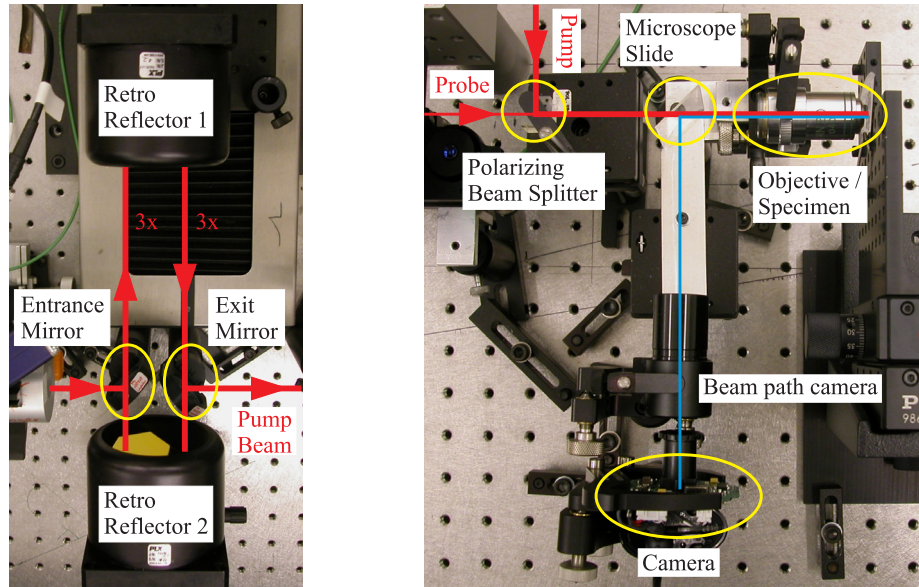


Figure 3.4: Left: 3x delay line with two retroreflectors. Retroreflector 1 is mounted on the translation table. Retroreflector 2 is mounted in a fixed position. Right: Realignment of the pump and the probe beams by the polarizing beam splitter and the coupling of the camera.

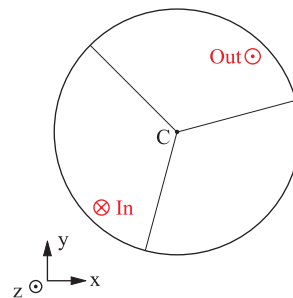


Figure 3.5: Frontal view on a schematic retroreflector: The position of the outgoing beam (*Out*) corresponds to the position of the incident beam (*In*) mirrored at the center of the retroreflector (*C*).

Fig. 3.3 and Fig. 3.4 on the right. With the specimen positioned in the focal plane of the objective, the pump and probe beam can comfortably be aligned by aligning their diffraction patterns on the camera image.

3.2.3 Delay line

The translation table of the delay line has a maximum travel distance of 250 mm. Using the delay line as in the basic setup delivers a maximum variation in the pump beam path of 500 mm, which corresponds to temporal delay of 1.7 ns. In order to increase the maximum temporal delay a setup with multiple reflections on the delay line is introduced. Therefore, the mirrors are replaced by two corner-type retroreflectors with a diameter of 63.5 mm. One of them is mounted on the translation stage, the other one is mounted in a fixed position as shown in Fig. 3.3

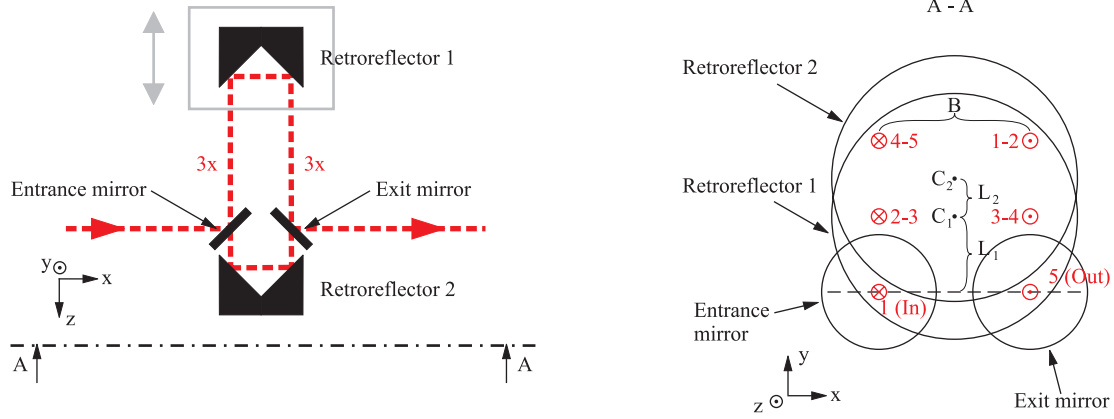


Figure 3.6: Left: Top view of the 3x delay line. Right: Side view of the 3x delay line. Relative positions of the incident beam (*In*), the outgoing beam (*Out*), the center of retroreflector 1 (C_1), and the center of retroreflector 2 (C_2) are shown in Fig. 3.6. L_1 is the vertical distance between the level of the incident and outgoing beams and the center of retroreflector 1, L_2 is the vertical distance between the center of retroreflector 1 and the center of retroreflector 2, and B is the horizontal distance between the incident and the outgoing beam see Fig. 3.6. C_1 and C_2 are positioned on the perpendicular bisector of the line between incident and outgoing mirror. The \otimes -vectors are mirrored at C_1 and the \odot -vectors are mirrored at C_2 . By choosing appropriate positions for the two retroreflectors, multiple reflections of the pump beam can be achieved. The number of roundtrips NR on the delay line is defined by the ratio of L_1 and L_2 .

and Fig. 3.4 on the left. A corner-type retroreflector consists of the inner surfaces of a corner with three mutually perpendicular faces. It reflects an incident beam in a parallel way with an offset depending on the entrance position of the beam. The position of the outgoing beam corresponds to the position of the incident beam mirrored at the center of the retroreflector, see Fig. 3.5. The relative positions of the incident beam (*In*), the outgoing beam (*Out*), the center of retroreflector 1 (C_1), and the center of retroreflector 2 (C_2) are shown in Fig. 3.6. L_1 is the vertical distance between the level of the incident and outgoing beams and the center of retroreflector 1, L_2 is the vertical distance between the center of retroreflector 1 and the center of retroreflector 2, and B is the horizontal distance between the incident and the outgoing beam see Fig. 3.6. C_1 and C_2 are positioned on the perpendicular bisector of the line between incident and outgoing mirror. The \otimes -vectors are mirrored at C_1 and the \odot -vectors are mirrored at C_2 . By choosing appropriate positions for the two retroreflectors, multiple reflections of the pump beam can be achieved. The number of roundtrips NR on the delay line is defined by the ratio of L_1 and L_2 .

$$NR = 1 + L_1/L_2 \quad (3.1)$$

L_1/L_2 must be a natural number. The following ratio is needed for the 3x delay line shown in Fig. 3.6:

$$L_1 = 2L_2 \quad (3.2)$$

By choosing a ratio L_1/L_2 large enough, any number of delay line roundtrips can be achieved with only two retro reflectors, theoretically. The most limiting fact for the application is, that there is some space needed for the incident and the outgoing beam. In the configuration shown in Fig. 3.6 where in the top view the mirrors are positioned between retro reflector 1 and 2, the mirrors and their mountings must not cut the lowest beams (beam 2-3 and beam 3-4). For the realized 3x delay line the following parameters are used (see Fig. 3.6): $B \cong 30$ mm, $L_1 \cong 20$ mm, and $L_2 \cong 10$ mm. With the 3x delay line a maximum time shift between pump and

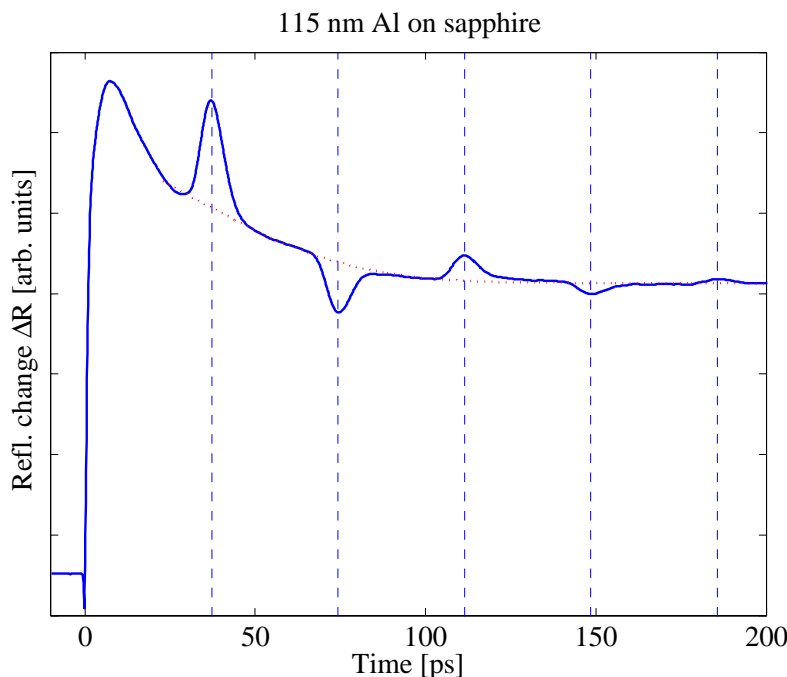


Figure 3.7: Measurement of the total reflectance change of a 115 nm Al film deposited by e-beam evaporation on a sapphire wafer (solid line). The dotted line corresponds to the thermal contribution to the reflectance change (empirical polynomial fit).

probe beam of 5 ns can be reached. This corresponds to the roundtrip time of a longitudinal wave in a silicon [100] specimen with a thickness of 21.1 μm .

In addition to the simple realization of multiple reflections on the delay line, the use of retro reflectors instead of single mirrors minimizes also the beam walking to a very small level. Assuming perfectly manufactured retro reflectors, the beam walking is governed by the quality of the adjustment of the entrance mirror only, whereas in the setup with two moving single mirrors on the delay line, the adjustment of the angles of these two mirrors additionally influenced the beam walking.

3.3 Typical characteristics of a reflectance measurement

In Fig. 3.7 a reflectance measurement of a 115 nm Al film deposited by e-beam evaporation on a sapphire wafer is shown. The overall shape of the measurement curve is mainly determined by the influence of the temperature on the reflectance: A sharp increase of the signal at time zero (fast heating by the laser pulse) followed by a relatively slow decay (cooling-down of the surface). Superimposed to this, several equidistant peaks can be recognized, denoted by vertical lines. These peaks are part of the acoustic contribution to the reflectance change and correspond to mechanical pulses being reflected at the free surface of the Al film. Information about the propagation of the mechanical waves is obtained by the acoustic contribution to the reflectance change. For this reason in this thesis for most of the measurements only

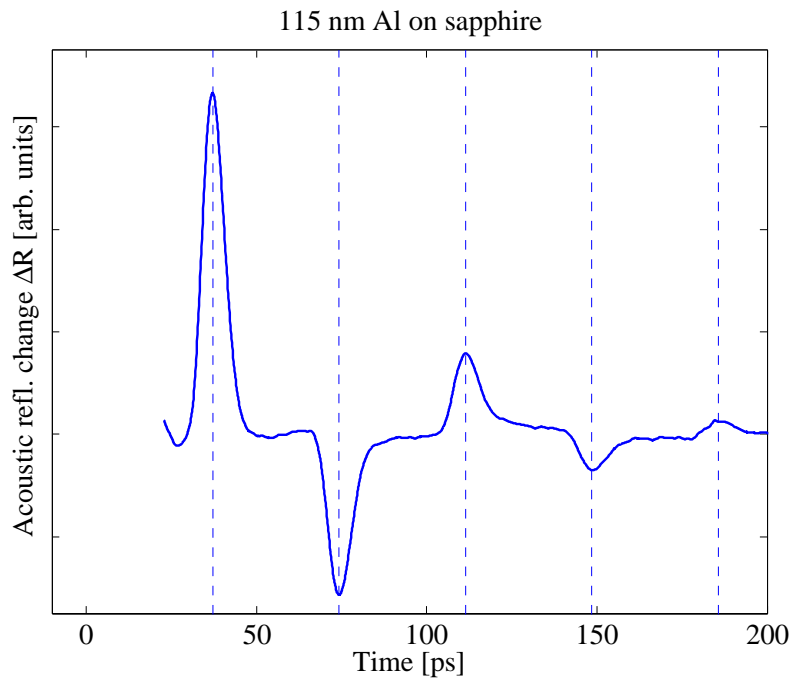


Figure 3.8: Acoustic contribution to the reflectance change of a 115 nm Al film deposited by e-beam evaporation on a sapphire wafer.

the acoustic contribution is discussed. The acoustic contribution corresponds to the total reflectance (solid line in Fig. 3.7) with the thermal part (dotted line in Fig. 3.7, based on a polynomial fitting) subtracted. The acoustic contribution of the measurement in Fig 3.7 is shown in Fig. 3.8. The roundtrip time of a mechanical wave packet in the Al film is determined by the temporal difference of two subsequent peaks in the acoustic contribution to the reflectance change. These peaks are getting weaker because of two reasons: First, with every reflection at the interface to the substrate a part of the energy is transmitted into the substrate. Second, energy is lost during the propagation within the Al layer due to attenuation.

The polarization of the peaks in the reflectance curve is governed by the values of the photoelastic constants (wavelength dependent material property, experimentally determined) and the polarization of the mechanical wave packet heading back to the surface, see equation (2.117). So, for Al single layer specimens (Al thin film on a substrate) measured with the pump probe setup presented in this thesis, only two cases can be distinguished regarding the polarization of these peaks:

- Case 1: The acoustic impedance (see equation 4.3) in the thin film is smaller than in the substrate.
- Case 2: The acoustic impedance (see equation 4.3) in the thin film is larger than in the substrate.

An example for case 1 is given in Fig. 3.8, meaning the first peak in the reflectance curve is positive and then alternates every time. Here the polarization of the mechanical wave packet changes only once per roundtrip, namely at the free surface.

In case 2 all peaks have a negative polarization because the polarization of the mechanical wave packet changes twice per roundtrip, at the free surface and at the interface.

The shape of the peaks in Fig. 3.8 is a bit different compared to the peaks of the measurements considered in chapter 4.1: The side peaks with opposite polarizations are missing here in chapter 3.3. Since the measurements presented here are done with a higher laser pulse intensity, nonlinear optical effects are a possible explanation for this difference.

4 Results

4.1 Aluminum thin films

4.1.1 Introduction

Al films are often used as top layer of specimens for laser acoustic measurements because they have a strong photoelastic effect and a high optical absorption in the near infrared range. If the behavior of the top layer of a specimen is well known, it is possible to estimate very accurately the properties of the underlying films of interest. Often there is a difference of the wave velocity in Al thin films compared to bulk material. The deposition process can strongly influence the wave velocity. Chinmulgund et al. [16] report that the gas pressure during the sputter process strongly influences the Young's Modulus of the Al thin film. They measured values between 47 and 74 GPa. Additionally, the Young's Modulus of Al thin films is influenced by the film thickness. Several publications report on decreasing values of the Young's modulus for decreasing thin film thicknesses, Profunser [60] and Mizubayashi et al. [53], [52]. In conclusion, the properties of Al layers can vary over a wide range and they have to be known in order to determine accurately properties of underlying films. This is especially important for cases where the attenuation of mechanical waves is investigated, because the decrease of the acoustic echoes after every roundtrip also depends on the force reflection coefficient, which is a function of the bulk wave velocities and thus of the Young's moduli (see equation (4.2)).

The frequency dependent attenuation behavior within homogeneous films is a very important parameter for the analysis of functionally graded materials. Functionally graded materials have interfaces between two layers with gradually varying mechanical properties instead of hard interfaces (see Vollmann et al. [83] and Aebi et al. [2]). In functionally graded specimens the frequency selective response of acoustic echoes is influenced not only by the graded interface but also by the frequency dependent attenuation behavior of the homogeneous top layer of the specimen.

Here, two different Al thin films are investigated regarding their attenuation of acoustic pulses in the GHz regime.

4.1.2 Specimens

One specimen is a 304 nm thick Al film deposited by electron beam (e-beam) evaporation and the second specimen is a 319 nm thick sputtered Al film. Both Al films are deposited on sapphire wafers. The process parameters for the depositions are listed in tables 4.1 and 4.2. The bulk wave velocities of the two Al types are calculated with the measured thickness at a reference point (profilometry measurements) and the measured time-of-flight at the same point (measurements with the pump

Pressure chamber	0.015 mTorr
Current e-beam	80 mA
Deposition rate	$\sim 300 \text{ \AA}/\text{min}$

Table 4.1: Listing of the deposition process parameters for the e-beam evaporated Al film.

Pressure	3 mTorr
Power	2250 W
Deposition rate	$\sim 1000 \text{ \AA}/\text{min}$

Table 4.2: Listing of the deposition process parameters for the sputtered Al film.

probe setup). The bulk wave velocity of the e-beam deposited Al film is determined to be 6200 m/s and the velocity of the sputtered Al film is determined to be 5873 m/s. The other parameters used for the analysis are the following: The density of Al 2700 kg/m³ *, the density of sapphire 3980 kg/m³ †, and the bulk wave velocity of sapphire 11476 m/s †.

4.1.3 Direct analysis of the attenuation from measurements

The measurement data of the e-beam evaporated Al-film are shown in Fig. 4.1. The acoustic contribution to the reflectance change is plotted in the upper diagram of Fig. 4.1. The first and the second echo are named $\Delta R_1(t)$ and $\Delta R_2(t)$, respectively. The magnitudes of the Fourier transforms of the two echoes $\Delta R_1(f)$ and $\Delta R_2(f)$ are plotted in the lower diagram of Fig. 4.1. Before the Fourier transformations are done, the 100 ps sequences (the sequences are colored red and blue in the upper plots of Figs. 4.1 and 4.2) are windowed with a symmetric 100 ps rectangle signal whose edges are rounded with 5 ps half hanning windows. Additionally the windowed signal then is elongated with a zero-signal of duration 400 ps.

Thomsen et al. [76] introduced the following formula for the determination of the attenuation α directly from the data in Fig. 4.1:

$$\alpha(f) = \frac{1}{2d} \ln \left(\frac{r_{FS} \Delta R_1(f)}{\Delta R_2(f)} \right) \quad (4.1)$$

α is the attenuation, f is the frequency, d is the film thickness, and r_{FS} is the bulk force reflection coefficient. r_{FS} is calculated with the acoustic mismatch theory using the acoustic impedances Z of the film and the substrate, respectively:

$$r_{FS} = \left| \frac{Z_{sub} - Z_{film}}{Z_{sub} + Z_{film}} \right| \quad (4.2)$$

The acoustic impedance of a material is defined by equation (4.3):

$$Z = \rho c_p \quad (4.3)$$

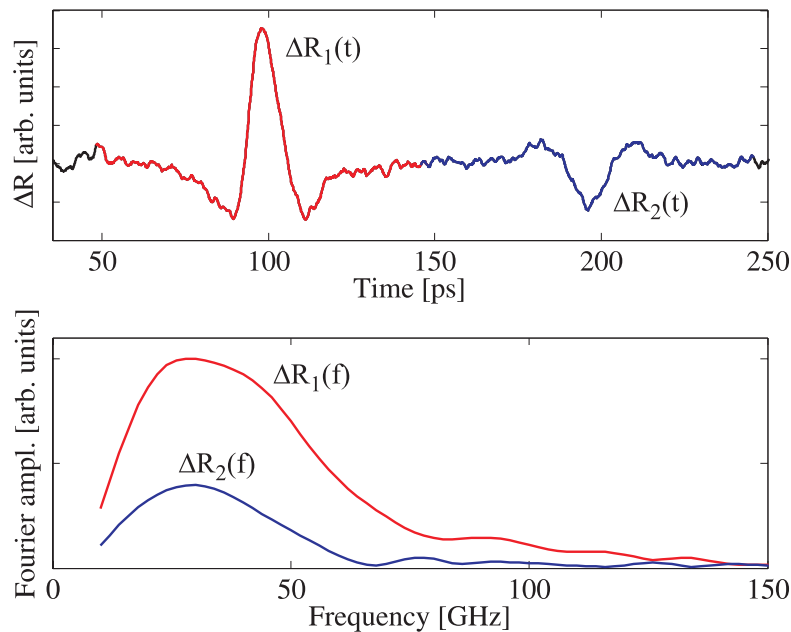


Figure 4.1: Upper diagram: Acoustic contribution to the reflectance change versus time for a 304 nm Al film deposited by e-beam evaporation on a sapphire substrate. Lower diagram: Magnitudes of the Fourier transforms of the two echoes in the upper diagram.

ρ is the density and c_p is the bulk wave velocity. The application of formula (4.1) is simple but requires two successive echoes and there must be no overlap between them. These conditions are satisfied for the measurements of the single Al layers with thicknesses in the range of 300 nm. The measurement data of the sputtered Al-film are shown in Fig. 4.2. Evaluating formula (4.1) at 30 GHz, α is found to be 2600 cm^{-1} for the e-beam deposited Al and 8900 cm^{-1} for the sputtered Al film. A series of measurements confirms that the attenuation α in the sputtered Al film is about 3 times larger than in the Al film deposited by e-beam evaporation for frequencies in the range of 30 GHz. These results show that in Al thin films there is a significant attenuation in this frequency range. An α of 2600 cm^{-1} means that during a roundtrip through a 300 nm thick film a stress wave packet loses 14.4% of its amplitude by attenuation. An α of 8900 cm^{-1} even yields a loss of 41.4 %. So in order to determine attenuations of underlying layers the attenuation in the Al transducer layer must not be neglected. Note that in α also beam spreading (spreading of the mechanical waves) is included, but assumed to be negligible, since the mechanical wavelength is much smaller than the laser spot size (see chapter 2).

4.1.4 Analysis with the viscoelastic simulation

Instead of applying formula (4.1) directly on the measurement data, the attenuation also can be determined by fitting a simulation of the entire pump probe measurement (including the viscoelastic wave propagation) to the measurement curve, as discussed

*www.webelements.com

†Guild optical associates, sapphire manufacturer

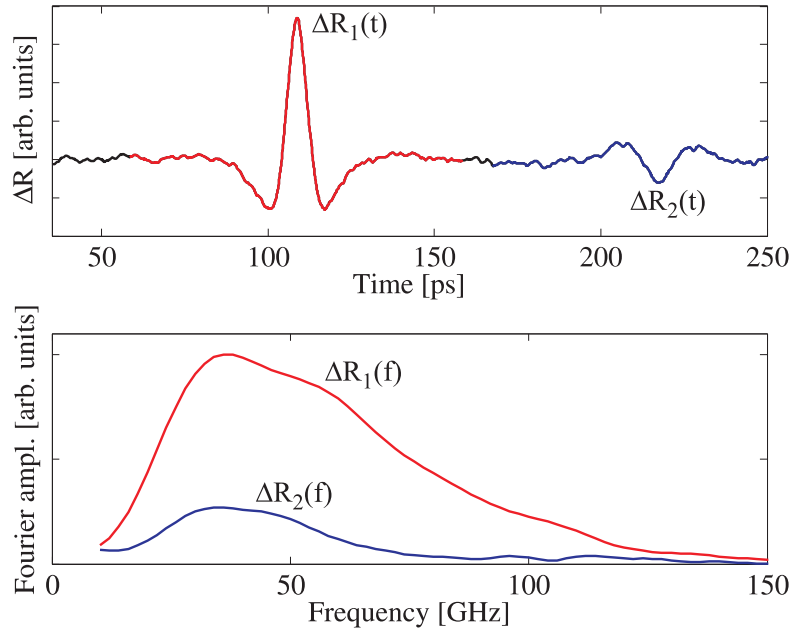


Figure 4.2: Upper diagram: Acoustic contribution to the reflectance change versus time for a 319 nm Al film sputtered on a sapphire substrate. Lower diagram: Magnitudes of the Fourier transforms of the two echoes in the upper diagram.

in chapter 2. This method is very powerful, since it can also be applied if the echoes arriving at the surface are overlapped, whereas the method used in chapter 4.1.3 does not work for these cases. Analyses of measurements with overlapping echoes are presented in chapter 4.2.4. Here the simulation fitting method is applied to the specimen with the 304 nm Al film deposited by e-beam evaporation on sapphire substrate. The simulation of the stress field for this specimen is shown in Fig. 4.3 on the left. At time 0 the mechanical pulse starts to propagate at the surface. After approximately 100 ps the first echo is back at the surface. The echoes coming back at the surface are getting weaker because of two reasons: First, with every reflection at the interface to the sapphire substrate a part of the energy is transmitted into the substrate. Second, energy is lost during the propagation within the Al layer due to attenuation. For the simulation on the left hand side in Fig. 4.3 the Mur's law (Equation (2.43)) is implemented in order to save computation time. The maximum stress values for excitation conditions as described in chapter 3.2.1 are estimated by numerical simulations to be in the order of 30 N/mm^2 which is in the elastic regime.

The fitting procedure is done by comparing the measured and the simulated curves of the reflectance change, see Fig. 4.4. Usually, the three independent parameters E_1 , E_2 , and T_0 of the viscoelastic standard linear solid are used for the fitting process according to chapter 2.3.3: They are chosen in a way to fit the attenuation, the bulk wave velocity, and the frequency dependent attenuation behavior. Here, a case is considered where the attenuation is already determined by a direct analysis of the measurement (chapter 4.1.3). In order to validate the simulation, the same value for the attenuation α is used for the viscoelastic simulation: $\alpha = 2600 \text{ cm}^{-1}$. The rest of the mechanical properties for the simulation is taken from chapter 4.1.2.

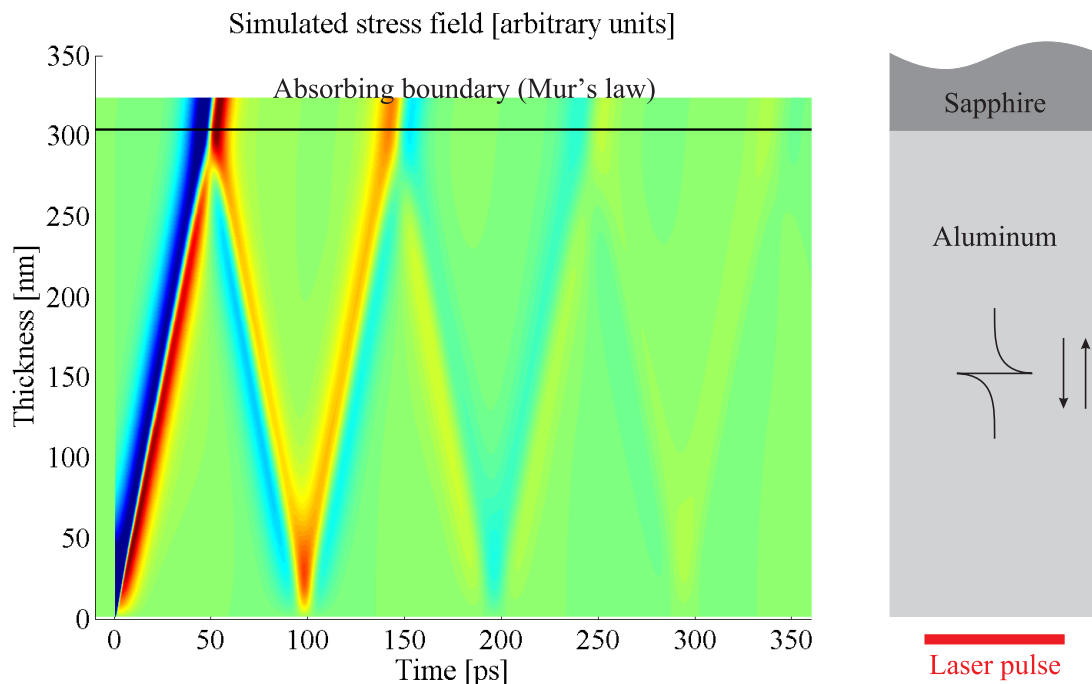


Figure 4.3: Left: Viscoelastic simulation of the stress field in the 304 nm Al film deposited by e-beam evaporation on a sapphire substrate. Right: Schematic sketch of the specimen.

The frequency dependent attenuation behavior is chosen to be quadratic, meaning that there is a quadratic relation between attenuation and frequency (Kelvin-Voigt material). The parameters used for the two temperature model are listed in appendix A.1. The simulated curve of the acoustic contribution of the reflectance change shown in Fig. 4.4 (middle curve) matches very well the measured curve (upper curve). The lower curve in Fig. 4.4 corresponds to a pure elastic simulation. The elastic simulation underestimates the decrease of the amplitudes of the echoes. Additionally, since the higher frequencies are not attenuated stronger than the lower frequencies (i.e. there is no attenuation for any frequencies), the shape of the echoes is too sharp.

In Fig. 4.5 (middle row) the frequency content of the measurement and the viscoelastic simulation is compared. In the range of the main frequency content (30 GHz) there is a very good match between measurement and simulation. In the lower row in Fig. 4.5 the frequency dependent attenuation behavior is compared. In the simulation it is perfectly quadratic since a Kelvin-Voigt like material is implemented. The measurement shows a slightly stronger increase of the attenuation with higher frequencies.

In conclusion, a viscoelastic simulation with the attenuation taken from the measurement in chapter 4.1.3 is presented ($\alpha = 2600 \text{ cm}^{-1}$ at 30 GHz, which is the frequency range with the largest energy content). The simulation yields a good match of the amplitudes of the echoes in the time domain (upper and middle curve in Fig. 4.4) and therefore is excellently suited for investigations of attenuation in thin films.

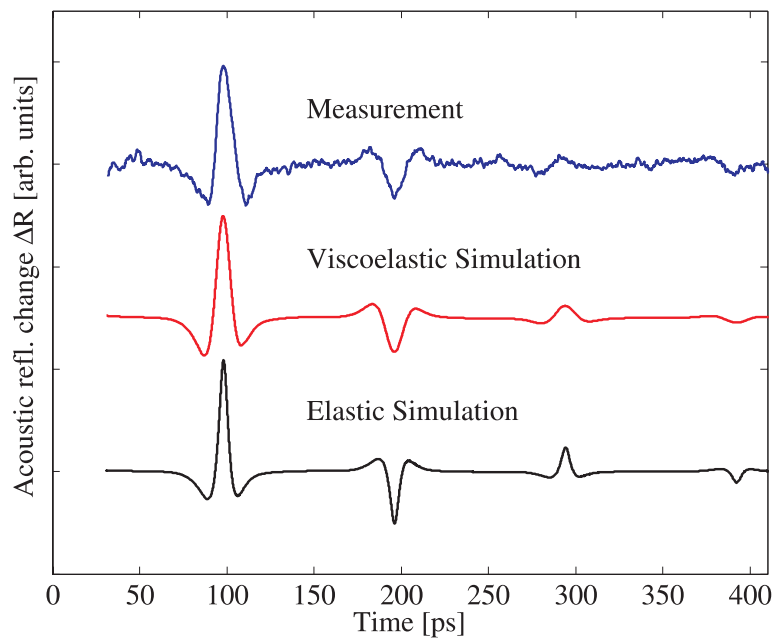


Figure 4.4: Acoustic contribution to the reflectance change of the 304 nm Al film deposited by e-beam evaporation on a sapphire substrate: Measurement, simulation with viscoelastic wave propagation, and simulation with elastic wave propagation.

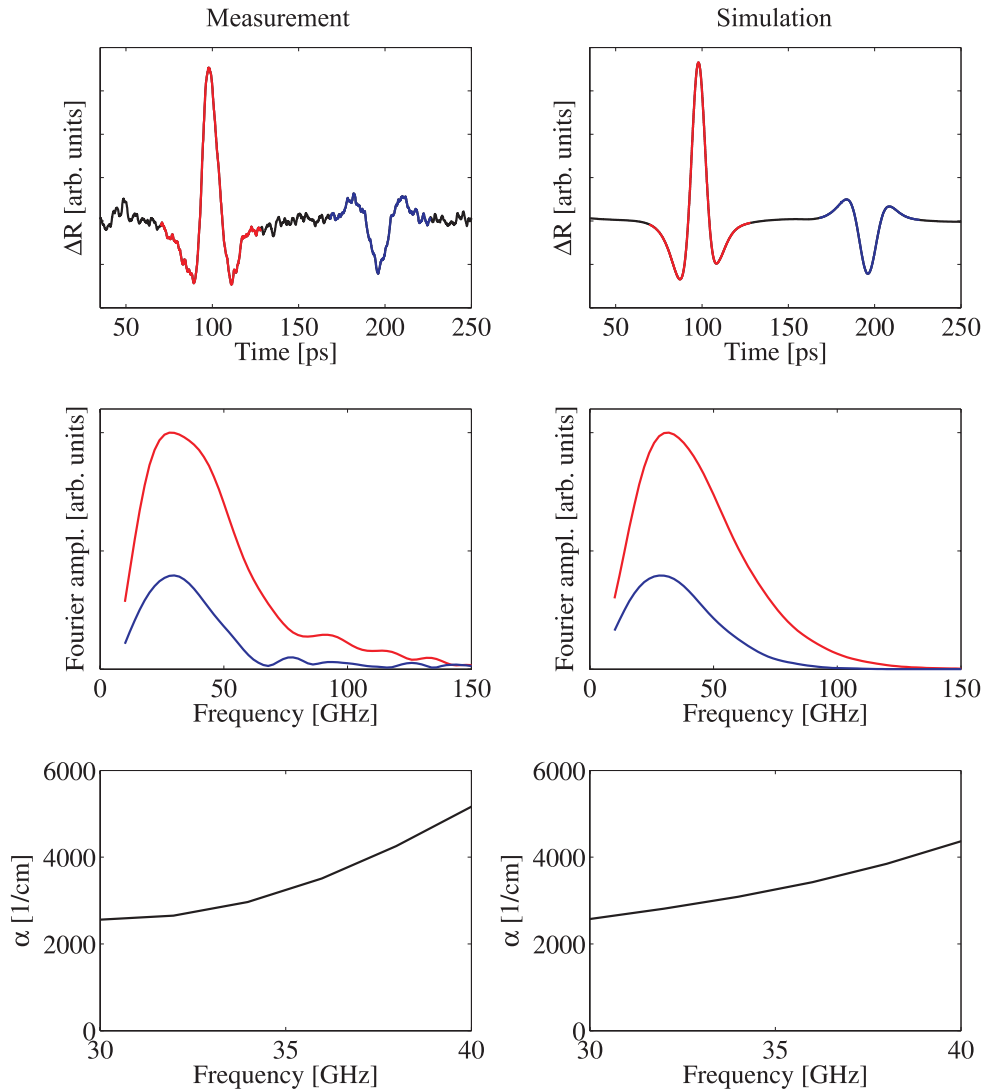


Figure 4.5: Reflectance change and attenuation of the 304 nm Al film deposited by e-beam evaporation on a sapphire substrate: Comparison between measurement (left) and viscoelastic simulation (right). Time domain (upper row), frequency domain (middle row), and frequency dependent attenuation (lower row).

4.2 Polymer films used for nanoimprint lithography

4.2.1 Introduction

Nanoimprint lithography (NIL) is a technique to imprint features with dimensions down to 10 nm into polymers, see Chou et al. [18], [17]. The patterned polymer can be used for devices such as photonic crystal structures, Schiff et al. [66], Belotti [6], linear wave guides, Ahn et al. [3], fluidic channels, Dumond et al. [26], Kehagias et al. [42], and surfaces of biological cell growth, Hu et al. [38]. All these applications depend on the very accurate reproduction of spatial patterns. Alternatively the patterned polymer is used as a resist layer. The pattern is transferred into the underlying material as in the case of semiconductor processing. Nanoimprint technology is targeted as a lithography technique for the 32 and 22 nm nodes of the International Roadmap for Semiconductors (ITRS) [1].

The implementation of nanoimprint lithography as a nanoscale manufacturing technique for features below 50 nm requires accurate values for the physical properties of the polymers, such as Young's modulus, used in this fabrication process. These affect the flow of polymer during imprinting, and determine the strength and stability of the polymer structures that are produced, Kehoe et al. [43]. A lot of relevant properties are taken from measurements of macroscopic bulk material specimens. However for thin films, physical properties can change significantly due to the increased importance of surface and interface effects, and the confinement of polymer molecules, Kehoe et al. [43]. Here the pump probe setup is used to measure the properties directly on polymer thin films.

4.2.2 Specimens and typical characteristics of the measurements

All specimens considered in chapter 4.2 have the same design and are manufactured by Tim Kehoe and coworkers at the Tyndall National Institute and at the Catalan Institute of Nanotechnology. The polymer layer of interest is spin coated onto a Silicon wafer. On top of the polymer layer there is an aluminum layer which is used as transducer for the excitation and detection with the laser. This design is shown in Fig. 4.6 on the right. In Fig. 4.6 on the left the viscoelastic simulation of the stress field is shown for a typical polymer specimen with an Al layer of ~ 65 nm and a PMMA layer of ~ 340 nm. At time zero at the surface of the aluminum layer (denoted by '1') the pump pulse arrives and launches a wave packet. After 10 ps the wave packet arrives at the interface Al/PMMA (denoted by '2'). One part of the packet is reflected and one part is transmitted into the PMMA layer. After 20 ps the first reflected wave packet returns to the surface (denoted by '3'), then every 20 ps another wave packet arrives at the surface. After 285 ps the first wave packet that traveled through the PMMA layer arrives back at the surface (denoted by '4'). The roundtrip time through the PMMA layer, denoted by Δt_{PMMA} in Fig. 4.6, is given by the difference of this arrival and the arrival of the first reflection after 20 ps. In Fig. 4.7 the measurement of the acoustic reflectance change of the same typical specimen (sputtered Al layer ~ 65 nm, PMMA layer ~ 340 nm) is shown. By comparison with the simulation in Fig. 4.6 it is obvious that the first group of peaks corresponds to the wave packets which traveled through the Al layer only (these

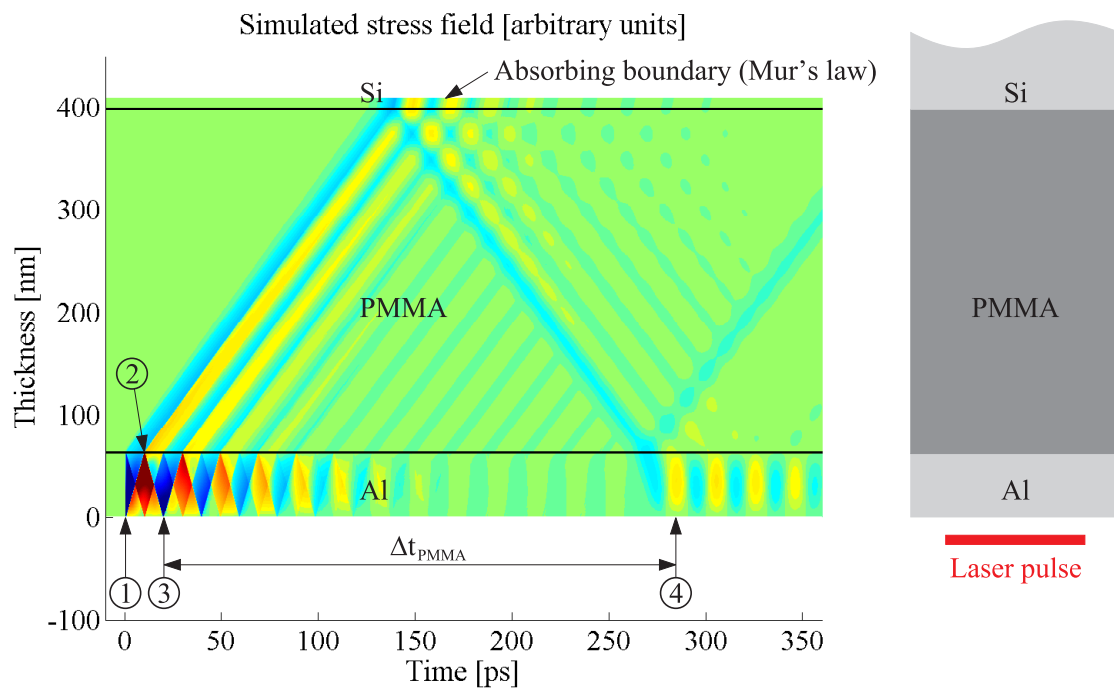


Figure 4.6: Left: Viscoelastic simulation of the stress field in a typical polymer specimen: Excitation at time zero (denoted by '1'), first partial reflection of the wave packet at the interface Al/PMMA after 10 ps (denoted by '2'), wave packet back at the surface after 20 ps (denoted by '3'), and first wave packet that traveled through the PMMA back to the surface after 285 ps (denoted by '4'). Δt_{PMMA} is the roundtrip time for the mechanical wave packet within the PMMA layer. Right: Schematic sketch of the specimen.

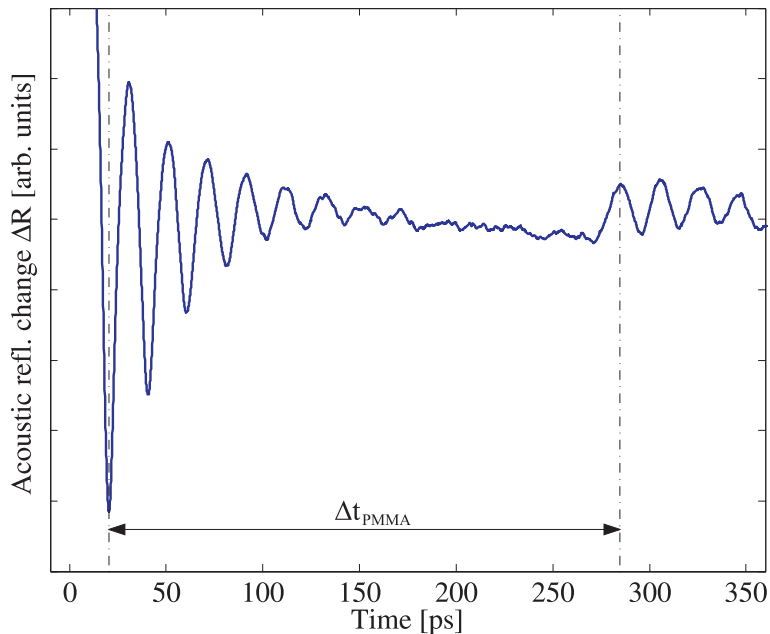


Figure 4.7: Measurement of the acoustic contribution to the reflectance change of a typical polymer specimen. Δt_{PMMA} is the roundtrip time for the mechanical wave packet within the PMMA layer.

peaks are called Al peaks in the following), the peaks after 285 ps are caused by wave packets which traveled once through the PMMA layer (these peaks are called polymer peaks in the following). The Al peaks have a negative polarization, the PMMA peaks have a positive polarization.

In addition to the just discussed wave packets there is another group of wave packets. They originate from a packet which is launched at time zero at the interface between the Al and the PMMA film, see Fig. 4.6. This packet is launched due to a temperature increase at the interface Al - PMMA. Although the absorption length of the laser pulses in Al films is in the range of only 10 nm, a part of the heat is distributed within the Al layer within a fraction of a picosecond and causes a temperature increase at the interface Al - PMMA. This characteristic is incorporated in the two temperature model in chapter 2.2. The waves originating from the packet launched at the interface have the opposite polarization and they arrive with a phase shift of 180° at the surface compared to the packets discussed above. Their Al peaks have a positive polarization, their PMMA peaks have negative a polarization. Some measurements show the tendency that the PMMA peaks (signal between 285 ps and 350 ps in Fig. 4.7) have a slight offset towards the positive direction. The reason for this is not yet fully understood.

If the polymer layer is clearly thicker than the Al layer Δt_{PMMA} can be directly determined by the measurement of the reflectance change, see Fig. 4.7. For specimens with the thickness of the polymer in the same range or even smaller than the thickness of the Al layer it is difficult or impossible to read Δt_{PMMA} directly from the measurement curve. The reason for this are the early arriving polymer peaks which interfere with the Al peaks. In these cases Δt_{PMMA} is determined by fitting the simulated reflectance change to the measured reflectance change. The simula-

tion is done using the viscoelastic model for the wave propagation as presented in chapter 2.3. For a known thickness of the polymer layer, the bulk wave velocity (and thus the p-wave modulus) is the fitting parameter, whereas for a known bulk wave velocity the layer thickness is the fitting parameter. In Fig. 4.8 the fitting is shown for a specimen discussed in chapter 4.2.6 with an Al layer of 35 nm (determined by profilometry) deposited by e-beam evaporation and a PMMA layer of 30 nm (determined by ellipsometry). The bulk wave velocity of the Al layer is determined by the arrival time of the first Al peak to be 6100 m/s. Since the thicknesses of the layers and the bulk wave velocity of the Al layer are known the bulk wave velocity of the PMMA is used as the only fitting parameter. In Fig. 4.8 three simulations with values 2650 m/s, 2700 m/s, and 2750 m/s for the bulk wave velocity of the PMMA layer are compared to the measurement. The simulation with the bulk wave velocity of 2700 m/s yields the best fit with the peak times in very good agreement to the measured data. With the 3 plots in Fig. 4.8 (2650 m/s, 2700 m/s, and 2750 m/s) it is estimated that with the fitting procedure the bulk wave velocity c_p can be determined with an accuracy of better than $\pm 2\%$ ($\sim \pm 50$ m/s). With the known thickness (30 nm) and the bulk wave velocity determined by the fitting procedure (2700 m/s) the roundtrip time Δt_{PMMA} is calculated to be 22.2 ps. In the plot of the simulation with 2700 m/s Δt_{PMMA} is drawn (middle plot in Fig. 4.8). Since the Al peaks and the PMMA peaks interfere, the time of arrival of the first PMMA peak does not correspond to a peak in the reflectance curve (unlike the case of thicker PMMA layers as in Fig. 4.7).

4.2.3 Bulk wave velocity

Two different types of imprinting polymers are investigated regarding their bulk wave velocities: mr-I PMMA 75k 300 and mr-NIL 6000. The thicknesses of the polymer layers have been determined by profilometry before the deposition of the Al layer. For mr-I PMMA 75k 300 a series of 8 specimens with thicknesses between 329 nm and 374 nm is measured, for mr-NIL 6000 a series of 5 specimens with thicknesses between 267 nm and 298 nm is measured. The measured bulk wave velocities c_p are summarized in table 4.3. The Young's moduli E are then calculated with equation (4.4) using the densities ρ given by the manufacturer (Micro Resist Technology) and the poisson's ratio ν assumed to be 0.4 (value taken from [79]).

$$E = \rho c_p^2 \frac{(1 + \nu)(1 - 2\nu)}{1 - \nu} \quad (4.4)$$

4.2.4 Attenuation

The attenuation in PMMA specimens is investigated using the simulation fitting method discussed in chapters 2.3.3 and 4.1.4. Two specimens are investigated: A PMMA layer with thickness 346 nm covered by a sputtered Al layer with thickness 59nm and a PMMA layer with thickness 590 nm covered by an sputtered Al layer with thickness 58nm. The material properties used for the simulation of the excitation by the two temperature model are given in appendix A.1. The bulk wave

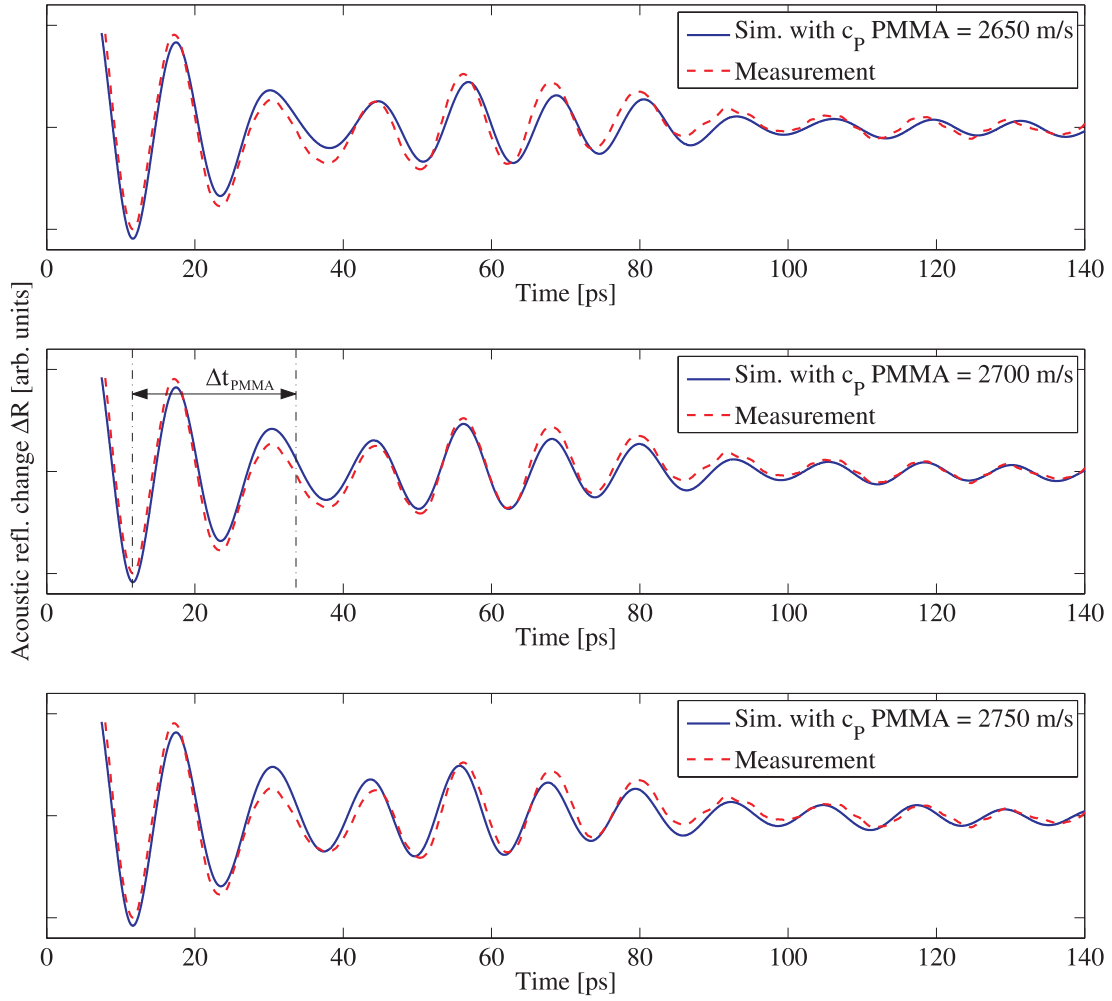


Figure 4.8: Acoustic contribution to the reflectance change of a specimen with an Al layer of 35 nm and a PMMA layer of 30 nm. Three simulations with different bulk wave velocities are compared to the measurement curve. 2700 m/s gives the best fit (central plot). Δt_{PMMA} is calculated to be 22.2 ps starting from the first Al peak (central plot).

Specimen	c_p [m/s]	std. dev. [m/s]	ν [-]	ρ [kg/m ³]	E [GPa]
mr-I PMMA	2644	79.7	0.4	1012	3.30
mr-NIL 6000	2503	55.2	0.4	1008	2.95

Table 4.3: Bulk wave velocity measurements of polymer specimens with thicknesses in the range of 300 nm: Bulk wave velocity c_p , standard deviation of the measured velocities, Poisson's ratio ν (assumption), density ρ (given by the manufacturer), and Young's modulus E (calculated).

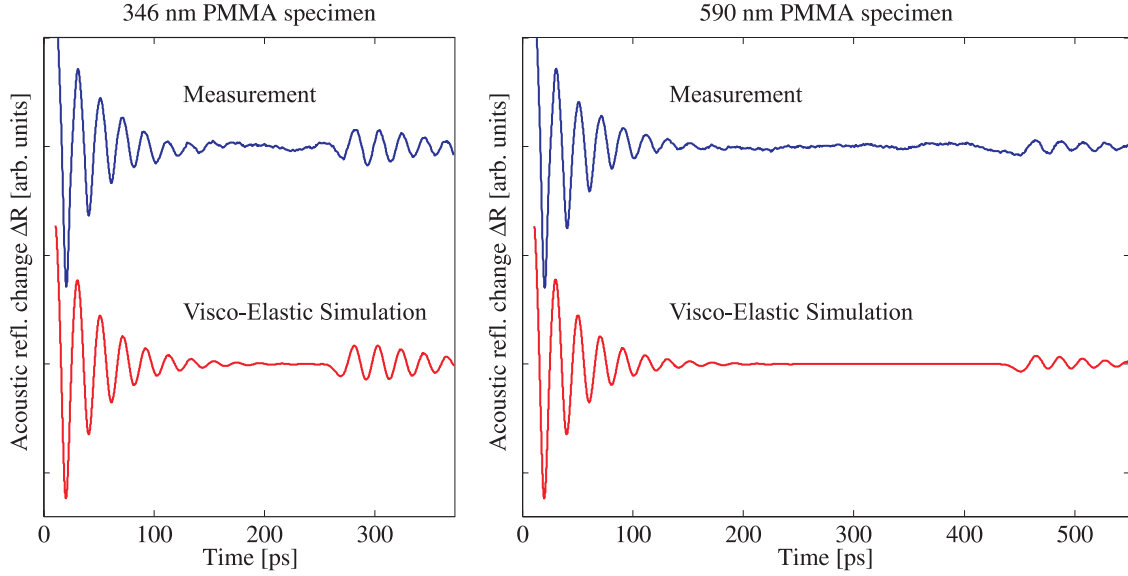


Figure 4.9: Acoustic contribution to the reflectance change: Measurements and viscoelastic simulations for the fitting of attenuation α . Left: 346 nm PMMA specimen. Right: 590 nm PMMA specimen.

velocity of the Al layers is determined on a reference specimen: With a pump probe measurement the time of flight is determined and with a scanning electron microscope (SEM) the thickness of the same layer is determined yielding to a bulk wave velocity of 5737 m/s. For the PMMA layers the value of 2644 m/s for the bulk wave velocity is taken from chapter 4.2.3. The other parameters used for the analysis are given in the following: The density of Al 2700 kg/m³ *, the density of PMMA 1012 kg/m³ † the bulk wave velocity of Silicon [100] 8432 m/s ‡, and the density of Silicon 2329 kg/m³ §. Using these parameters the simulations are fitted to the measurements using the attenuation α as fitting parameter, see Fig. 4.9. Both measurements are optimally fitted by using the same value for the attenuation α . A Kelvin-Voigt like behavior is simulated which is in agreement with the measurement series for PMMA done by Morath et al. [54] showing a quadratic relation between attenuation and frequency. For the sputtered Al top layers the attenuation α is found to be 20500 cm⁻¹ at 50 GHz. For the PMMA layers of both specimens (346 nm and 590 nm) α is found to be 22600 cm⁻¹ at 50 GHz. Assuming a quadratic relation between attenuation and frequency this result is in good agreement with the measurements done by Morath et al. [54] for frequencies between 90 and 320 GHz.

4.2.5 Effect of thickness on bulk wave velocity

For thin mr-I PMMA 75k 300 specimens the influence of the layer thickness on the bulk wave velocity is investigated. The bulk wave velocity is measured for specimens

*www.webelements.com

†Micro Resist Technology, manufacturer

‡calculated from values given by Royer et al. [65]

§Royer et al. [65]

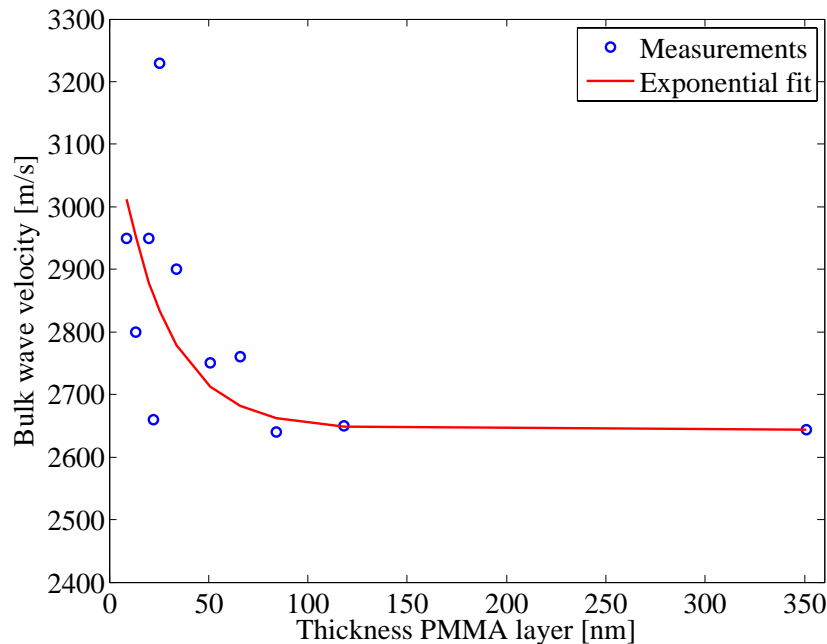


Figure 4.10: Bulk wave velocity in PMMA layers as a function of thickness: Measurements and an exponential fit.

with layer thicknesses between 9 nm and 118 nm. The thicknesses are determined by ellipsometry. The measured velocities of these specimens and the averaged value of chapter 4.2.3 for PMMA (c_p 2644 m/s at thickness 351 nm) are shown in Fig. 4.10. Although the measured values have a certain scattering, probably due to the uncertainty of the thickness measurements of the thinnest specimens by ellipsometry, there is a tendency: It turns out that the specimens with thicknesses smaller than about 80 nm have higher bulk wave velocities. Taking the exponential fit in Fig. 4.10 an increase of 10% of the bulk wave velocity is expected for a layer thickness of 17 nm. Due to the quadratic relation between bulk wave velocity and Young's modulus (see equation (4.4)) this corresponds to an increase of the Young's modulus of about 20 % assuming constant density and constant Poisson's ratio. Possible reasons for this increase are discussed in chapter 4.2.6.

4.2.6 Effect of surface material on bulk wave velocity

4 specimens were coated with a monolayer of Hexamethyldisilazane (HDMS) before spin coating of the PMMA. First it was thought necessary to use this primer layer in order to get a continuous film of PMMA for thicknesses of less than 30 nm, although in the end it was not required. The measured bulk wave velocities of the specimens with HDMS are found to be smaller than the velocities of specimens with similar thicknesses without HDMS (same measurements as in chapter 4.2.5). The measurements are compared in Fig. 4.11. The average of the bulk wave velocities of the HDMS specimens is 6% lower. This decrease of the bulk wave velocity may be due to the reduction in surface energy of the silicon caused by adding the HDMS layer to it, Kehoe et al. [43]. Fryer et al. [33] report that they measured a decrease in the glass transition temperature for surfaces with lower interface energy. This

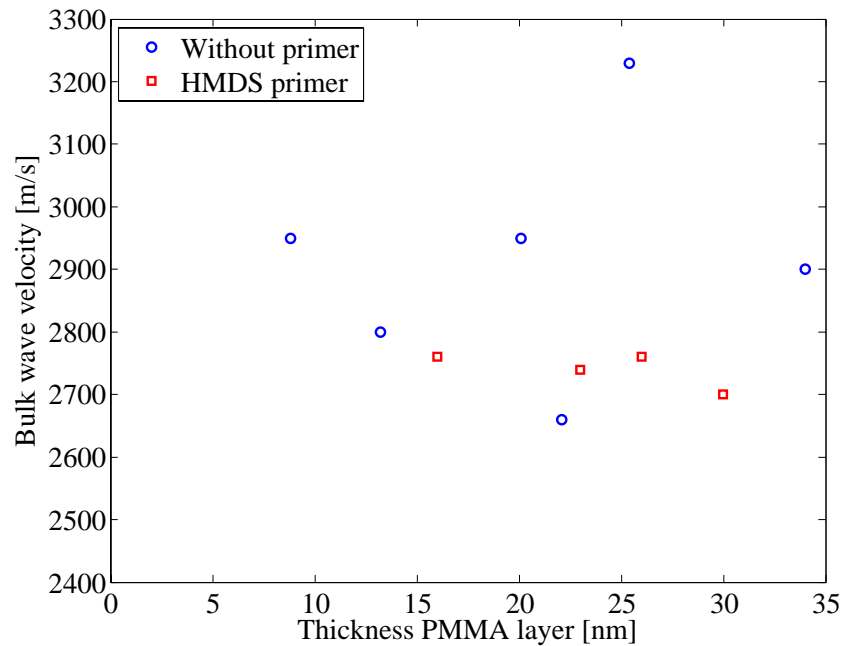


Figure 4.11: Bulk wave velocity in thin PMMA layers with and without HMDS primer.

fact also suggests that the increase in Young's modulus for thinner PMMA layers is due to the greater importance of interface effects over volume effects at reduced dimensions, rather than to confinement of the PMMA molecules at this scale [43]. The molecular confinement should have an effect at rather approximately twice the radius of gyration than at 80 nm. The radius of gyration is approximately 7 nm for PMMA 75k, Zhou et al. [90].

4.3 Structured polymer specimens

4.3.1 Introduction

In chapter 4.2 plain polymer films were investigated. The goal was to determine physical properties such as Young's modulus and attenuation and to investigate the influence on these properties of factors such as thickness or surface material. The motivation for the considerations in this chapter is to characterize or to check the geometry of the specimens with the assumption of known material properties. In contrast to AFM measurements here not only the topography is analyzed but also the thickness of the different layers.

4.3.2 100 μm line structures

The investigated specimen has imprinted lines into PMMA with a width of 100 μm on a silicon wafer. On the top of the PMMA lines there is a sputtered Al transducer layer. An image of the specimen taken with a confocal light microscope is shown in Fig. 4.12. Since the laser beams of the pump probe setup can be focused down to a spot size of 3-5 μm it is possible to do scans across the lines. Like this the thickness

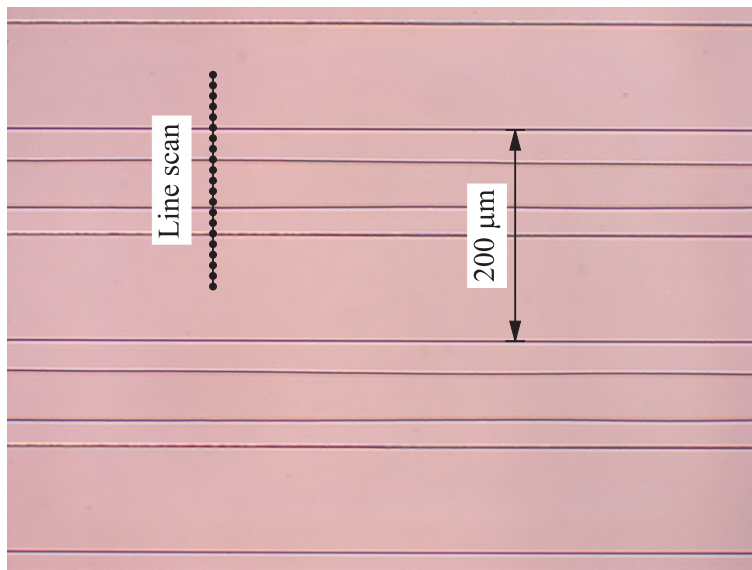


Figure 4.12: Structured polymer specimen with $100\ \mu\text{m}$ line structures. The image is taken with a confocal light microscope.

profile is recorded. For the calculation of the thickness the bulk wave velocity of $2644\ \text{m/s}$ is taken from chapter 4.2.3. In Fig. 4.13 the results of a line scan are plotted. A distance of $200\ \mu\text{m}$ is scanned with steps of $10\ \mu\text{m}$, see Fig. 4.12. The walls in the thickness profile show that there has been a problem during the imprinting process. The groove in the stamp was not fully filling to make a perfect line. This effect is a known problem with larger dimensions. Since filling starts at the edges of the line, closest to the polymer being imprinted, there are walls at the edges. The thickness of the residual layer which is a key parameter for the nanoimprinting process is in the range of $290\ \text{nm}$.

4.3.3 $10\ \mu\text{m}$ square dots

Laterally resolved thickness measurements are possible for structures with feature sizes down to the range of the spot size of the laser. This is demonstrated with two pump probe measurements on a PMMA structure with imprinted square dots. On the top of the PMMA dots there is a sputtered Al transducer layer. An image of the specimen taken with a confocal light microscope is shown in Fig. 4.14. In Fig. 4.15 on the left a measurement done between the dots is shown. On the right a measurement done on a dot is shown. Taking the bulk wave velocity value of $2644\ \text{m/s}$ from chapter 4.2.3 the PMMA thickness between the dots is determined to be $292\ \text{nm}$ and the thickness on the dots is determined to be $469\ \text{nm}$. Thus, the dots have a height of $177\ \text{nm}$.

4.3.4 Submicron patterns

For specimens with patterns in the submicron range, the single features cannot be resolved with the pump probe setup presented in chapter 3. Nevertheless the quality or the evenness of a specimen can be inspected by measurements of resonance

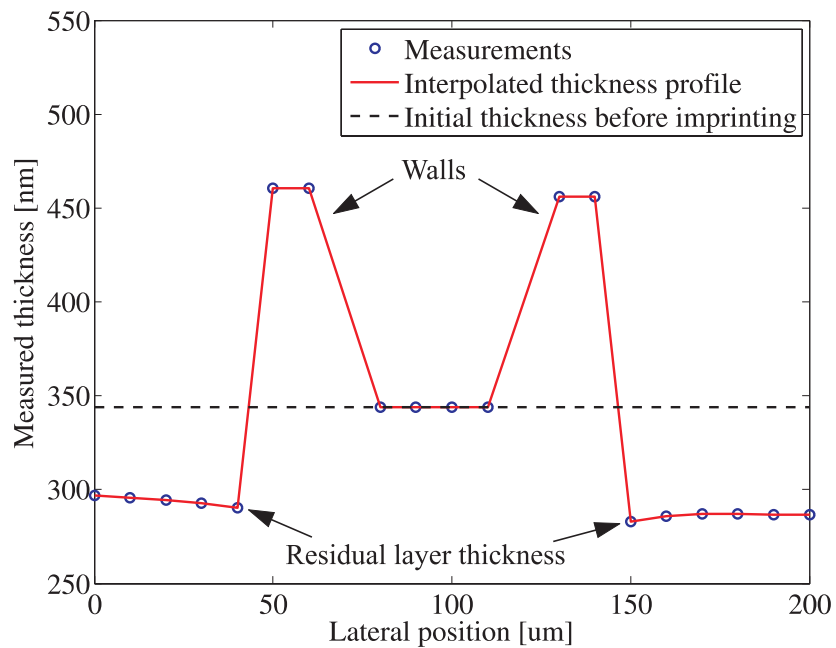


Figure 4.13: Thickness measurements ($200\ \mu\text{m}$ line scan) on the specimen shown in Fig. 4.12. Due to a imperfect imprinting there are walls at the edges of the line.

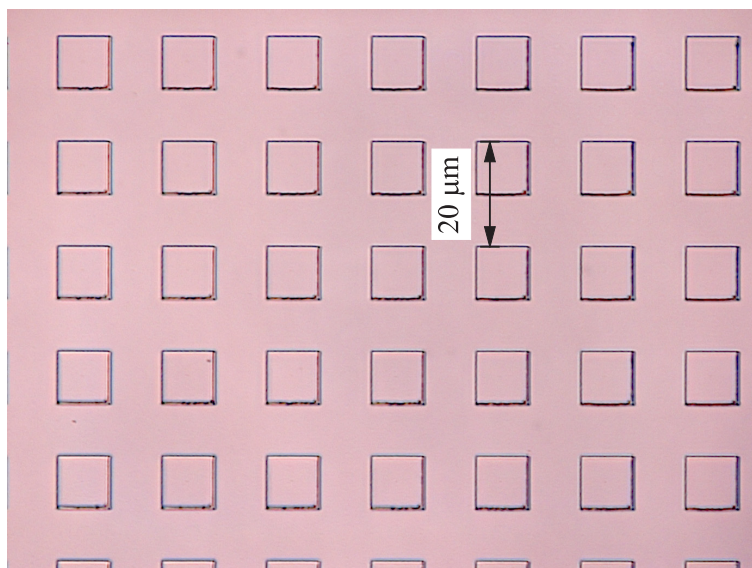


Figure 4.14: Structured polymer specimen with $10\ \mu\text{m}$ square dots. The image is taken with a confocal light microscope.

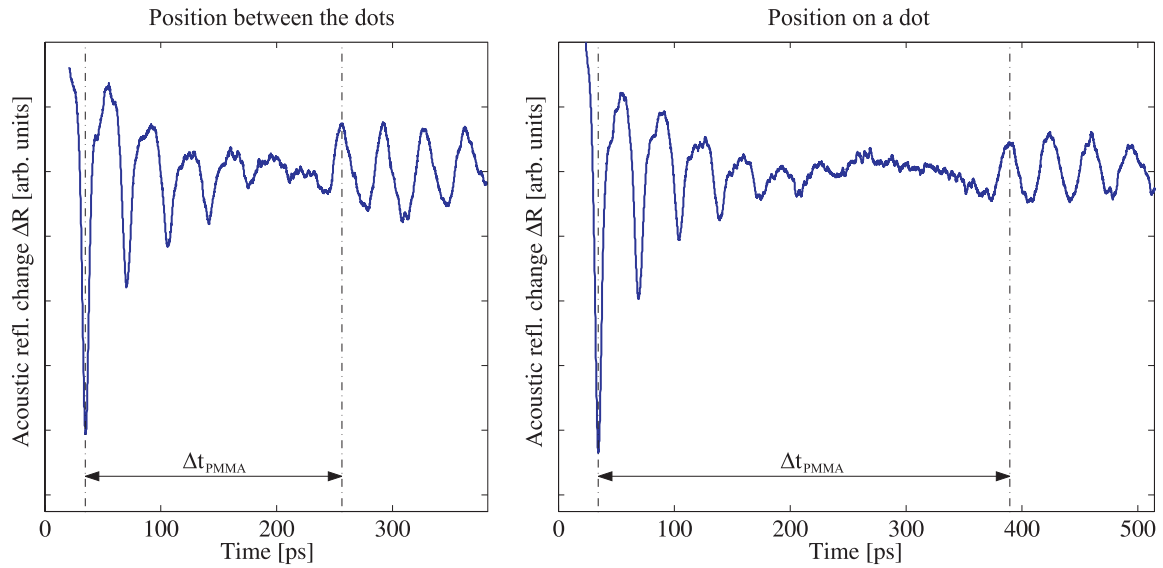


Figure 4.15: Specimen with $10\ \mu\text{m}$ square dots: Measurements of the acoustic contribution to the reflectance change at two different positions. Left: Position between the dots. Right: Position on a dot.

frequencies. This is shown for a PMMA specimen which has imprinted holes with a nominal diameter of $350\ \text{nm}$ and a distance between the holes of $1\ \mu\text{m}$. On the top of the PMMA layer there is a sputtered Al transducer layer. Due to problems during the imprinting process the holes of the investigated specimen are distorted in different ways depending on the lateral position on the wafer. In Fig. 4.16 SEM images of the specimen in two different lateral positions are shown. In the following the two regions on the specimen are named area 1 and area 2 according to Fig. 4.16. Area 1 and area 2 are 5 millimeters apart. For both areas three measurements are done with a distance of $50\ \mu\text{m}$ between them. Measurement 1 on area 1 is shown in Fig. 4.17. On the left the acoustic contribution of the reflectance change is plotted. It has to be noticed that the time scale is larger than in the measurements

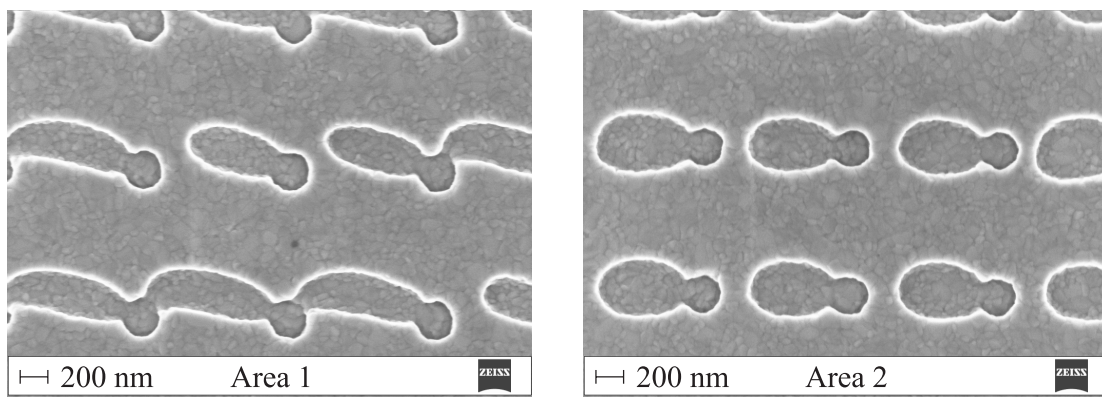


Figure 4.16: SEM top view images of Area 1 and Area 2. Depending on the lateral position the holes with nominal diameter $350\ \text{nm}$ are distorted differently due to problems during the imprinting process.

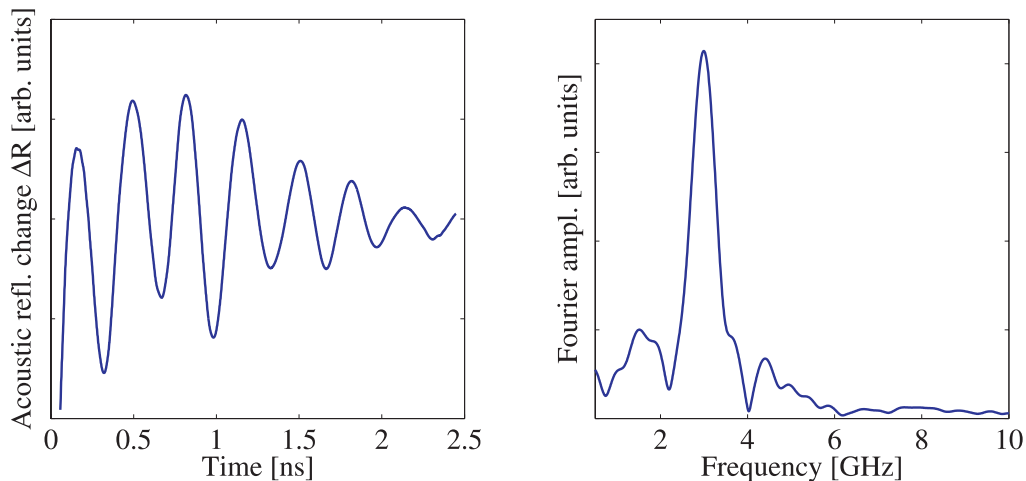


Figure 4.17: Specimen with submicron holes measured at point 1 of area 1 (see also table 4.4). Left: Measurement of the acoustic contribution to the reflectance change. Right: Magnitude of the Fourier transform with the maximum value at 2.99 GHz.

Measurement Position	Point 1 Area 1	Point 2 Area 1	Point 3 Area 1	Point 1 Area 2	Point 2 Area 2	Point 3 Area 2
Resonance Frequency	2.99 GHz	3.01 GHz	2.97 GHz	3.18 GHz	3.17 GHz	3.18 GHz

Table 4.4: Specimen with submicron holes: Resonance frequencies in areas 1 and 2.

in the previous chapters. The signal expresses an acoustic resonance of the hole structure. The magnitude of the Fourier transform is plotted in Fig. 4.17 on the right, having the maximum value at 2.99 GHz. Before the Fourier transformation is done, the 2.4 ns sequence shown in Fig. 4.17 on the left is windowed with a symmetric 2.4 ns rectangle signal whose edges are rounded with 50 ps half hanning windows. Additionally the windowed signal then is elongated with a zero-signal of duration 93.2 ns.

The results of all resonance frequency measurements are summarized in table 4.4. The average of the measured resonance frequencies of area 2 is 6.2 % higher than that of area 1. By such measurements specimens with submicron patterns can be checked regarding the quality of the imprinting.

4.4 Materials for thin film solar cells

4.4.1 Introduction

Photovoltaics is a sustainable technology for energy production and will have an increasing importance in the coming years. In order to be an alternative to fossil fuel technologies the costs of photovoltaic needs to be reduced by a factor 2-5 (Catchpole et al. [15]). The price of silicon (Si) causes a big part of the costs of conventional solar cells which are based on silicon wafers with thicknesses in the range of some hundred microns. For this reason in the recent years a lot of research has been done in the field of Si thin film solar cells. In thin film solar cells the thickness of the Si layer(s) is in the order of some hundred nanometers up to several microns. The thin Si layers are deposited on substrates of cheaper materials as for example glass. a-Si:H (hydrogenated amorphous Silicon) and μc -Si:H (hydrogenated microcrystalline Silicon) are often used as active area materials. The contacting is done by transparent conductive oxide materials (TCO) as for example SnO₂ (tin oxide) or ZnO (zinc oxide).

A lot of research has been done on optical and electronic properties of thin film solar cell materials but only little information is available about mechanical properties and the mass density of these materials, Caglar [14]. Additionally, their mechanical properties are strongly dependent on the specific deposition processes and conditions. This makes it difficult to find reliable values in literature. This lack of knowledge on the mechanical properties and the difficulty to gain information of layer and interface properties in a solar cell stack are the main motivations for the following investigations of typical materials used in thin film solar cells. All specimens investigated in this chapter have been deposited by Oerlikon Solar AG.

4.4.2 Layout of the specimens

The specimens have a similar design as the polymer specimens in chapter 4.2: The layer of interest is between a substrate and an Al top layer which is used as transducer for the pump probe measurements. Here, float glass plates are used as substrate. The layer of interest is deposited on the float glass with the same equipment from Oerlikon Solar AG as it is used for the commercial production of thin film solar cells. Finally an Al layer with thickness between 40 and 60 nm is sputtered onto the layer of interest. A schematic sketch of a specimen is shown in Fig. 4.18.

Since the thickness of the layer of interest is at least in the range of 200 nm it is possible to read the corresponding roundtrip time directly from the measurement curves, similar to Fig. 4.7. The thickness of the Al layer and the underlying layer of interest are measured by profilometry. Like this the pump probe measurements directly yield a value for the bulk wave velocity.

4.4.3 Determination of Young's modulus with nanoindentation

In order to get additional information about the Si thin films, the specimens in chapters 4.4.4 and 4.4.5 are also investigated with nanoindentation measurements. For this reason in this chapter the nanoindentation method is briefly discussed.



Figure 4.18: Schematic sketch of the specimens with layers from photovoltaics.

The nanoindentation measurements were done with a Hysitron Triboindenter with a Berkovich diamond tip at the Laboratory for Nanometallurgy at the ETH Zurich. During the nanoindentation process the diamond is pressed into the surface of the specimen and then released, and the load-displacement data are recorded. 9-10 indentations are done per specimen. One indentation consists of six partial load cycles with increasing indentation forces. Every unloading curve determines a E_r , a so called reduced modulus, see Oliver and Pharr [56]. This reduced modulus is a function of the elastic properties (Young's modulus E and Poisson's ratio ν) of the specimen and of the indentation tip as defined in equation (4.5):

$$\frac{1}{E_r} = \frac{1 - \nu_{specimen}^2}{E_{specimen}} + \frac{1 - \nu_{tip}^2}{E_{tip}} \quad (4.5)$$

Solved for the Young's modulus of the specimen equation (4.5) yields equation (4.6):

$$E_{specimen} = \frac{1 - \nu_{specimen}^2}{\frac{1}{E_r} - \frac{1 - \nu_{tip}^2}{E_{tip}}} \quad (4.6)$$

The parameters for the diamond tip are chosen to be $E_{tip} = 1141$ GPa and $\nu = 0.07$ according to Oliver and Pharr [55].

In Fig. 4.19 the hemisphere of influence is shown for a single thin film on a substrate which is indented by a tip with load P . a is the contact radius, h is the maximum penetration depth, and d is the thickness of the film. Already for very small ratios h/d the deformation field is influenced not only by the properties of the film but also by the properties of the substrate. Consequently nanoindentation data of thin films in the range of 200 nm always have to be considered as bilayer data being influenced by the film and the substrate. Jung et al. [41] introduced an empirical model which estimates the modulus E_r measured with nanoindentation

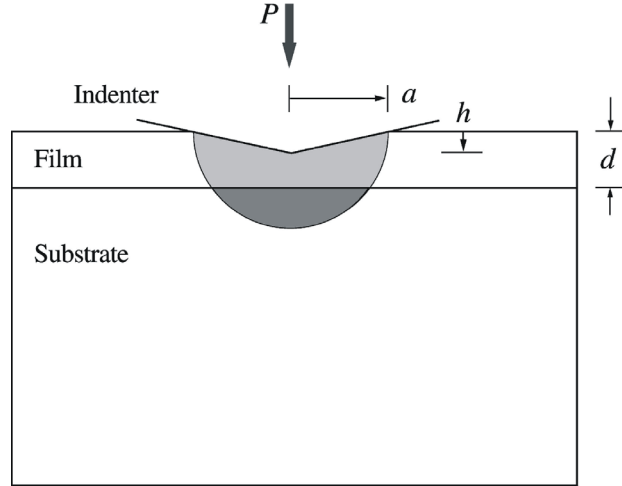


Figure 4.19: Hemisphere of influence for the deformation field during nanoindentation, figure taken from Jung et al. [41].

depending on the ratio h/d and the moduli of the film and the substrate:

$$E_r = E_{r,substrate} \left(\frac{E_{r,film}}{E_{r,substrate}} \right)^L \quad (4.7)$$

with

$$L = \frac{1}{1 + A\left(\frac{h}{d}\right)^C} \quad (4.8)$$

A and C are parameters of the empirical model. A is determined to be 3.76 and C is determined to be 1.38, Jung et al. [41]. By fitting this empirical model with fitting parameter $E_{r,film}$ to measurement series with varying h/d the Young's modulus of the film can be estimated.

4.4.4 Hydrogenated amorphous silicon (a-Si:H)

a-Si:H is one of the most used active area materials in thin film solar cells. It is an amorphous isotropic material without periodicity and long distance order. The average bond angles of the atoms are distorted compared to crystalline Si and some bonds are broken leading to the so-called dangling bonds. Pure a:Si without hydrogen has a very high density of dangling bonds and is therefore not usable as active area material in solar cells, Senoussaoui [69]. The density of dangling bonds can be reduced by addition of hydrogen during the deposition process in order to enable doping, Spear [71]. This leads to the a-Si:H which is usable as active area material. In Fig. 4.20 the structures of a-Si:H and crystalline Si are compared.

The a-Si:H layers investigated here are deposited by HF-PECVD (high frequency plasma enhanced chemical vapor deposition) on commercial equipment by Oerlikon Solar AG (OC Oerlikon KAI-1200). Typical process parameter ranges used for the deposition of the a-Si:H layers are listed in table 4.5. Details about the solar cells can be found in Caglar [14].

Since the mechanical properties of a-Si:H depend strongly on the deposition process and its parameters the values reported in the literature have a large variation.

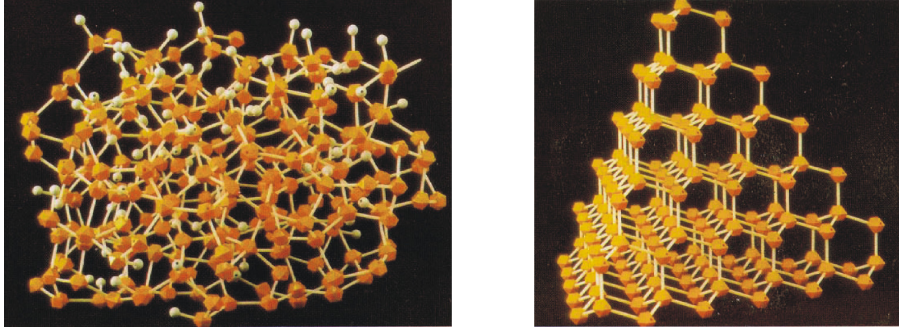


Figure 4.20: Left: Structure of a-Si:H. Right: Structure of crystalline Si. In crystalline Si there is long range order whereas in a-Si:H not even short range order is present. Figures taken from Meilloud [51].

Plasma excitation frequency	40 MHz
Deposition temperature	< 220 °C
Chamber pressure	0.1-0.9 mBar
Silane concentration	40-60%
Plasma excitation power	250-500 W

Table 4.5: Listing of the deposition process parameters for the a-Si:H layers.

For example, values between 1470 and 2300 kg/m³ can be found for the mass density of a-Si:H deposited by the PECVD technique, Searle [68]. For the Young's modulus values between 55 and 150 GPa are reported with the tendency of smaller values for higher hydrogen contents [68].

Four a-Si:H specimens are measured with the pump probe setup. In all four specimens the Al layers have thicknesses in the range of 40 nm and the a-Si:H layers have thicknesses in the range of 200 nm. One representative pump probe measurement is shown in Fig. 4.21. After approximately 15 ps the first wave packet is back at the surface being reflected at the interface Al-Si (denoted by '1'). After approximately 64 ps the first echo coming from the Si-Glass interface is back at the surface (denoted by '2'). The roundtrip time in the a-Si:H layer $\Delta t_{a-Si:H} = 49$ ps is given by the time difference of peak 2 and peak 1. With the measured roundtrip time and the thickness determined by profilometry the bulk wave velocity c_p then can be calculated directly with equation (2.2). The mean value and the standard deviation of c_p of the four measurements are presented in table 4.6.

The reason for the double peak structure after peak 2 (circled in Fig. 4.21) is not fully understood. A probable explanation is the presence of an interlayer between the a-Si:H layer and the glass substrate.

Additionally the Young's modulus of one a-Si:H specimen is measured with nanoindentation as described in chapter 4.4.3. The measurements and an empirical fit are shown in Fig. 4.22. The black dots correspond to reduced Young's moduli measured by single indentations. The circles represent the averaged values at the 6 measured indentation depths h/d . The solid line is the empirical fit according to equation (4.7). For a large ratio h/d the empirical fit must correspond to the

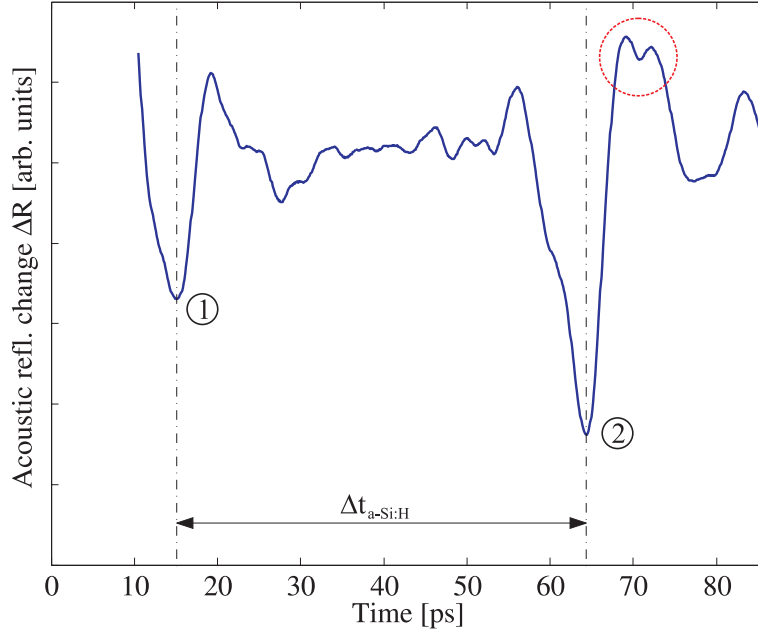


Figure 4.21: Measurement of the acoustic contribution to the reflectance change of a typical a-Si:H specimen. Thickness Al layer 42 nm, thickness a-Si:H layer 186 nm. $\Delta t_{a-Si:H}$ is the roundtrip time for the mechanical wave packet within the a-Si:H layer. Peak 1 corresponds to the first echo coming back from the Al-Si interface, peak 2 corresponds to the first echo coming back from the Si-Glass interface.

reduced Young's modulus of the glass substrate which is measured separately to be 73.8 GPa. The empirical fit shown in Fig. 4.22 yields a reduced Young's modulus E_r for the a-Si:H film of 99 GPa. Assuming the Poisson's ratio ν of a-Si:H to be 0.22 corresponding to the average crystalline value [68], the Young's modulus of a-Si:H is calculated using equation (4.6) to be 103 GPa.

This value should be considered as a rough estimation, since the accuracy of nanoindentation measurements is limited for thin films with thicknesses in the range of 200 nm. On one hand a small ratio h/d is preferable in order to measure mainly the properties of the film and not of the substrate. On the other hand a certain penetration depth h is necessary in order to limit errors caused by the surface roughness of the specimen. In table 4.6 a standard deviation of 10% is assumed for the Young's modulus.

With known bulk wave velocity c_p and known Young's modulus E the mass density can be calculated with equation (4.9):

$$\rho = \frac{E}{c_p^2} \frac{1 - \nu}{(1 + \nu)(1 - 2\nu)} \quad (4.9)$$

The value of the Poisson ratio ν for a-Si:H is again assumed to be 0.22 [68]. The calculated value for the density of a-Si:H (1973 kg/m³) is clearly smaller than the value for crystalline Si (2329 kg/m³). This result seems to be plausible due to the higher disorder of a-Si:H and due to its hydrogen content. A summary of all considered physical properties of a-Si:H is given in table 4.6.

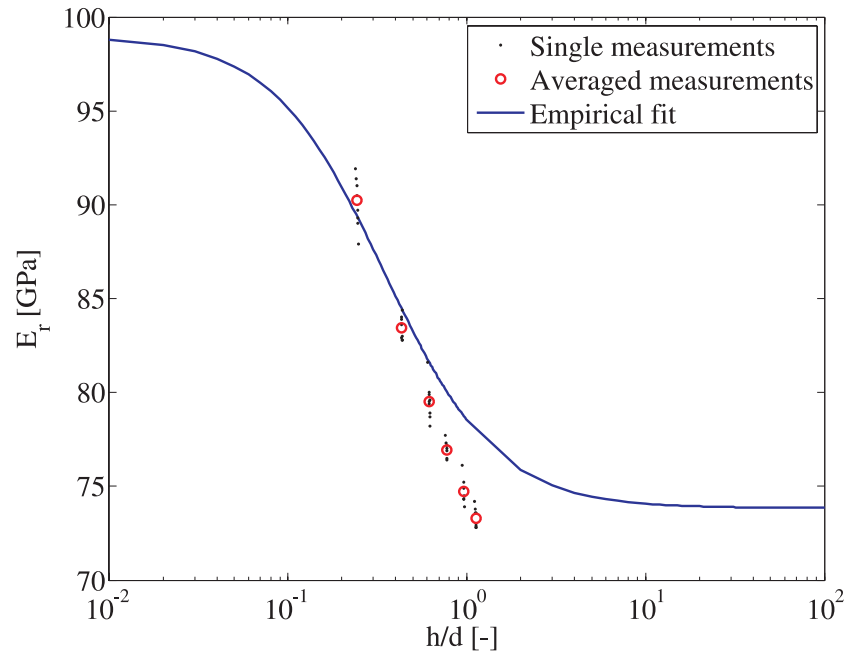


Figure 4.22: Nanoindentation measurements of a 192 nm a-Si:H layer on a float glass substrate: Reduced Young's modulus E_r for different penetration depths h . The black dots correspond to reduced Young's moduli measured by single indentations. The circles are the averaged values at 6 different indentation depths h/d . The solid line is the empirical fit (equation (4.7)) yielding a reduced Young's modulus E_r of 99 GPa for a-Si:H. For a large ratio h/d the empirical fit must correspond to the reduced Young's modulus of the glass substrate which is 73.8 GPa.

Property	c_p [m/s]	E [GPa]	ν [-]	ρ [kg/m ³]
Value	7721±132	103±10.3	0.22	1973±265
Source	Pump probe measurements	Nano-indentation	Literature [68]	Calculated with Eq. (4.9)

Table 4.6: Summary of the properties of a-Si:H films with thicknesses in the range of 200 nm.

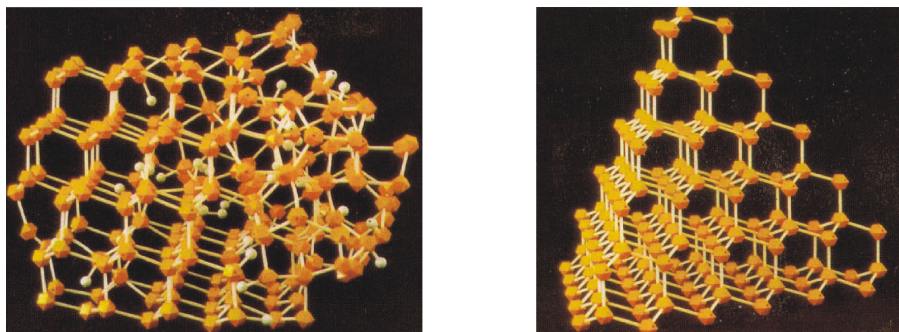


Figure 4.23: Left: Structure of μc -Si:H. Right: Structure of crystalline Si. In crystalline Si there is long range order whereas in μc -Si:H only short range order (some tens of Nanometers) is present. Figures taken from Meilloud [51].

Plasma excitation frequency	40 MHz
Deposition temperature	160-220 °C
Chamber pressure	2-3 mBar
Silane concentration	<10%
Plasma excitation power	2000-4000 W

Table 4.7: Listing of the deposition process parameters for the μc -Si:H layers.

The negative polarization of the peak of the first wave packet after 15 ps (see Fig. 4.21) means that the acoustic impedance Z (see equation 4.3) of the Al top layer is larger than the acoustic impedance of the buried a-Si:H layer which amounts to $1.52e7 \text{ kg/m}^2\text{s}$ (calculated with c_p and ρ taken from table 4.6). Since the bulk wave velocity in the Al layer could not be determined accurately (technical problems with the profilometer), no direct condition to the mass density of the Al layer can be established.

4.4.5 Hydrogenated microcrystalline silicon (μc -Si:H)

μc -Si:H is also used as active area material in thin film solar cells. Since it covers a different absorption spectrum than a-Si:H there is a large potential for solar cells having these two materials combined. μc -Si:H is a complex material consisting of crystalline and amorphous phases and grain boundaries. In Fig. 4.23 the structures of μc -Si:H and crystalline Si are shown.

The μc -Si:H layers are deposited with the same equipment as the a-Si:H layers investigated in chapter 4.4.4: High frequency plasma enhanced chemical vapor deposition in a OC Oerlikon KAI-1200 system. Only the deposition process parameters are changed. Typical ranges for the deposition parameters are listed in table 4.7. Decreasing the silane concentration and increasing the plasma excitation power forces a transition from amorphous to microcrystalline structures and thus increases the crystalline volume fraction, Droz [25]. In Fig. 4.24 the structural transition from amorphous to microcrystalline silicon depending on the crystalline volume fraction is illustrated schematically. For higher crystalline volume fractions the amorphous incubation layer vanishes almost completely. Typical μc -Si:H solar grade material

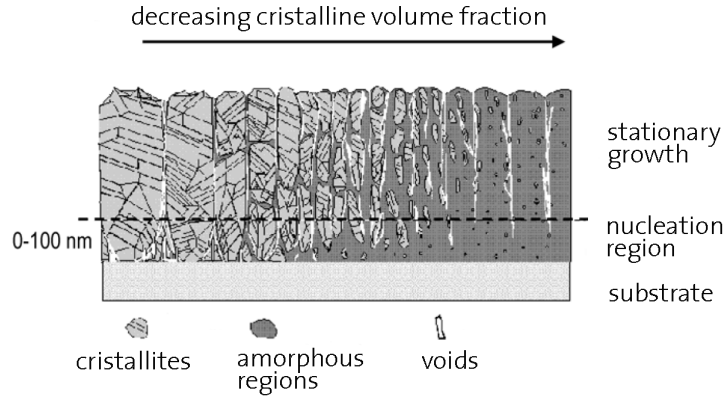


Figure 4.24: Structure of a $\mu\text{c-Si:H}$ film depending on the crystalline volume fraction. Figure taken from Senoussaoui et al. [69].

comprises a crystalline volume fraction of about 60% measured with Raman spectroscopy. The layers investigated in this chapter are deposited in high power regimes in order to have microcrystalline structures even for films with thicknesses of only 200 nm.

Similar to a-Si:H, the values of the physical properties of $\mu\text{c-Si:H}$ are influenced strongly by the deposition process and its parameters. Bursikova et al. [13] measured 125 ± 4 GPa for the Young's modulus of a 850 nm thick $\mu\text{c-Si:H}$ layer deposited on Pyrex substrate. They used the nanoindentation technique but did not mention the value of Poisson's ratio they used for the calculations. Zhou et al. [89] measured with small angle X-ray scattering 2280 kg/m^3 for the density of $\mu\text{c-Si:H}$ deposited by PECVD.

Four $\mu\text{c-Si:H}$ specimens are measured with the pump probe setup. In all four specimens the Al layers have thicknesses in the range of 40 nm and the $\mu\text{c-Si:H}$ layers have thicknesses in the range of 200 nm. One representative pump probe measurement is shown in Fig. 4.25. After approximately 14 ps the first wave packet is back at the surface being reflected at the interface Al-Si (denoted by '1'). After approximately 66 ps the first echo coming from the Si-Glass interface is back at the surface (denoted by '2'). The roundtrip time in the $\mu\text{c-Si:H}$ layer $\Delta t_{\mu\text{c-Si:H}} = 52$ ps is given by the time difference of peak 2 and peak 1. With the measured roundtrip time and the thickness determined by profilometry the bulk wave velocity c_p then can be calculated directly with equation (2.2). The mean value and the standard deviation of c_p of the four measurements are presented in table 4.8.

The Young's modulus of one $\mu\text{c-Si:H}$ specimen is measured with nanoindentation as described in chapter 4.4.3. The measurements and an empirical fit are shown in Fig. 4.26. The black dots correspond to reduced Young's moduli measured by single indentations. The circles represent the averaged values at the 6 measured indentation depths h/d . The solid line is the empirical fit according to equation (4.7). For a large ratio h/d the empirical fit must correspond to the reduced Young's modulus of the glass substrate which is measured separately to be 73.8 GPa. The empirical fit shown in Fig. 4.22 yields a reduced Young's modulus E_r for the $\mu\text{c-Si:H}$ film of 111 GPa. Assuming the Poisson's ratio ν of $\mu\text{-Si:H}$ to be 0.22 corresponding

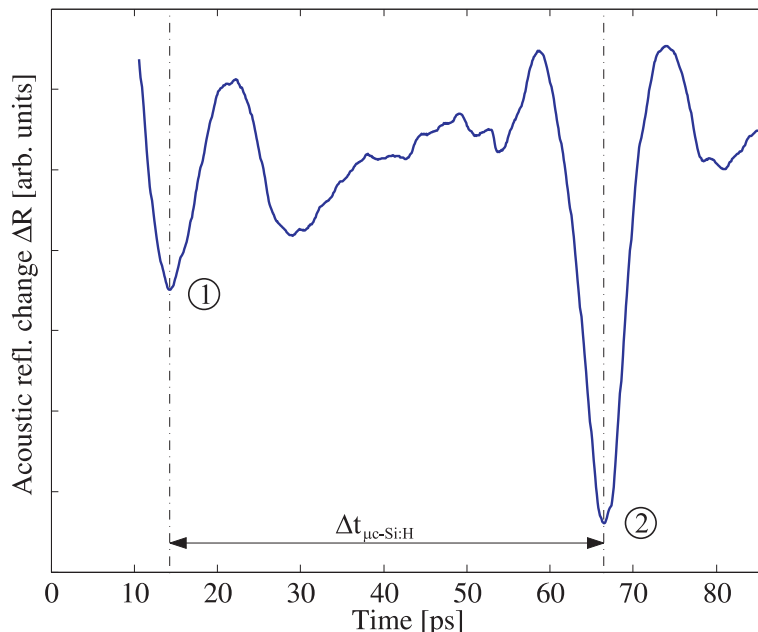


Figure 4.25: Measurement of the acoustic contribution to the reflectance change of a typical $\mu\text{c-Si:H}$ specimen. Thickness Al layer 41 nm, thickness $\mu\text{c-Si:H}$ layer 208 nm. $\Delta t_{\mu\text{c-Si:H}}$ is the roundtrip time for the mechanical wave packet within the $\mu\text{c-Si:H}$ layer. Peak 1 corresponds to the first echo coming back from the Al-Si interface, peak 2 corresponds to the first echo coming back from the Si-Glass interface.

Property	c_p [m/s]	E [GPa]	ν [-]	ρ [kg/m ³]
Value	8119±38	117±11.7	0.22	2026±222
Source	Pump probe measurements	Nano-indentation	Literature [68]	Calculated with Eq. (4.9)

Table 4.8: Summary of the properties of $\mu\text{c-Si:H}$ films with thicknesses in the range of 200 nm.

to the average crystalline value, Searle [68], the Young's modulus of $\mu\text{c-Si:H}$ is calculated using equation (4.6) to be 117 GPa.

As discussed in chapter 4.4.4 this value should be considered as a rough estimation. In table 4.8 a standard deviation of 10% is assumed for the Young's modulus. With known bulk wave velocity c_p and known Young's modulus E the density can be calculated with equation (4.9). The value of the Poisson ratio ν for $\mu\text{c-Si:H}$ is again assumed to be 0.22 [68]. This yields a density of 2026 kg/m³. A summary of all considered physical properties of $\mu\text{c-Si:H}$ is given in table 4.8.

The bulk wave velocity in $\mu\text{c-Si:H}$ (8119 m/s) is about 5% higher than in a-Si:H (7721 m/s) and 3.7% smaller than in crystalline Si[100] (8432 m/s). These results seem to be very plausible looking at the independently measured values of the Young's moduli by nanoindentation. Although the absolute accuracy of the nanoindentation measurements is not very good, the results of the $\mu\text{c-Si:H}$ and the a-Si:H specimens can be compared relative to each other. This shows that

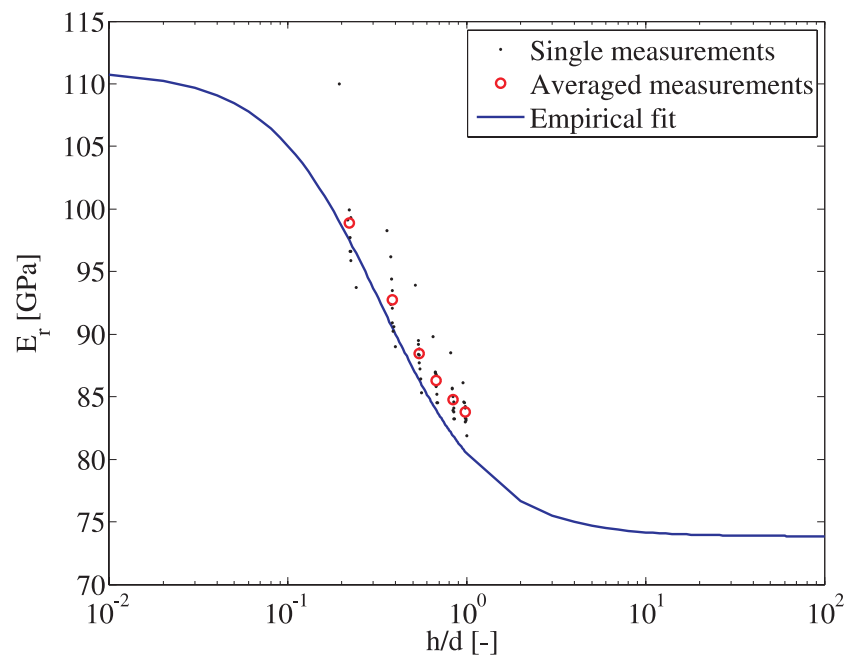


Figure 4.26: Nanoindentation measurements of a 208 nm $\mu\text{c-Si:H}$ layer on a float glass substrate: Reduced Young's modulus E_r for different penetration depths h . The black dots correspond to reduced Young's moduli measured by single indentations. The circles are the averaged values at 6 different indentation depths h/d . The solid line is the empirical fit (equation (4.7)) yielding a reduced Young's modulus E_r of 111 GPa for $\mu\text{c-Si:H}$. For a large ratio h/d the empirical fit must correspond to the reduced Young's modulus of the glass substrate which is 73.8 GPa.

the Young's modulus of $\mu\text{c-Si:H}$ (117 GPa) is estimated to be 13.6% larger than the Young's modulus of a-Si:H (103 GPa). With the quadratic relation between Young's modulus and bulk wave velocity (see equation (4.4)) this means that the increased bulk wave velocity in $\mu\text{c-Si:H}$ compared to a-Si:H is mainly caused by the increased Young's modulus and thus the densities of the two materials are very similar. They are calculated to be 2026 kg/m^3 for $\mu\text{c-Si:H}$ and 1973 kg/m^3 for a-Si:H.

The negative polarization of the peak of the first wave packet after 14 ps (see Fig. 4.25) means that the acoustic impedance Z (see equation 4.3) of the Al top layer is larger than the acoustic impedance of the buried $\mu\text{c-Si:H}$ layer which amounts to $1.64\text{e}7 \text{ kg/m}^2\text{s}$ (calculated with c_p and ρ taken from table 4.8). Since the bulk wave velocity in the Al layer could not be determined accurately (technical problems with the profilometer), no direct condition to the mass density of the Al layer can be established.

4.4.6 Influence of crystalline volume fraction in $\mu\text{c-Si:H}$

A series of three $\mu\text{c-Si:H}$ specimens with increasing crystalline volume fractions are investigated and also compared with an a-Si:H specimen. All four specimens have Si layers with thicknesses in the range of 200 nm (measured by profilometry) and are deposited with the same equipment. Only the plasma excitation power is varied in order to get different crystalline volume fractions: The crystalline volume fraction of $\mu\text{c-Si:H}$ increases with increasing plasma excitation power. In the following the specimens are named a-Si:H, $\mu\text{c-Si:H}$ low power, $\mu\text{c-Si:H}$ medium power, and $\mu\text{c-Si:H}$ high power.

The crystalline volume fraction ϕ of the four specimens is measured with Raman spectroscopy, Caglar [14]. The deconvolution of the Raman peaks into their crystalline and amorphous contributions results in crystalline volume fraction values of 0%, 13%, 34%, and 58% for the a-Si:H, $\mu\text{c-Si:H}$ low power, $\mu\text{c-Si:H}$ medium power, and $\mu\text{c-Si:H}$ high power specimen, respectively.

Additionally the optical absorption, characterized by the imaginary part κ of the complex refractive index, is measured by ellipsometry at an optical wavelength of 500 nm. Since a-Si:H is a better absorber at 500 nm than $\mu\text{c-Si:H}$ the value κ is also a quantity for the crystallinity of a specimen. The measured values for κ are 0.572, 0.330, 0.284 and 0.190 for the specimens with increasing crystalline volume fractions.

The bulk wave velocities of the four specimens are measured with the pump probe setup. The measurements are shown in Fig. 4.27. The values for the bulk wave velocity c_p are determined to be 7759 m/s (a-Si:H), 8156 m/s ($\mu\text{c-Si:H}$ low power), 8263 m/s ($\mu\text{c-Si:H}$ medium power), and 8344 m/s ($\mu\text{c-Si:H}$ high power). The difference of the bulk wave velocities between the a-Si:H and the $\mu\text{c-Si:H}$ specimens is quite large as also seen in chapters 4.4.4 and 4.4.5. But also within the $\mu\text{c-Si:H}$ specimens c_p is increasing for specimens with increasing crystalline volume fractions. Hence the pump probe setup is capable to determine qualitatively the crystalline volume fraction.

Additionally, there is a very good agreement between the measured bulk wave velocities in this chapter (a-Si:H and $\mu\text{c-Si:H}$ low power) and the values measured

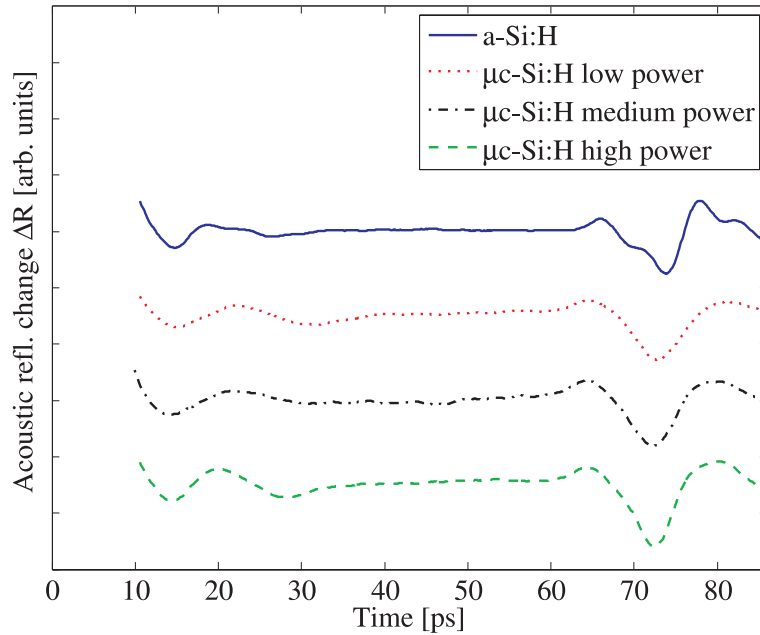


Figure 4.27: Measurement of the acoustic contribution to the reflectance change of the series with increasing crystalline volume fraction.

Specimen	d [nm]	ϕ [-]	κ [-]	c_p [m/s]
a-Si:H	230	0%	0.572	7759
μ c-Si:H low power	236	13%	0.330	8156
μ c-Si:H medium power	240	34%	0.284	8263
μ c-Si:H high power	242	58%	0.190	8344

Table 4.9: Results of the series with different crystallinity: Thickness d , crystalline volume fraction ϕ , imaginary part of complex refractive index κ , and bulk wave velocity c_p .

in chapters 4.4.4 and chapter 4.4.5, where the specimens have been deposited with similar PECVD parameters. The results of the series with different crystallinity are summarized in table 4.9.

4.4.7 Low pressure chemical vapor deposited (LPCVD) ZnO

Zinc oxide is a transparent conductive metal oxide (TCO) which is used in photovoltaics as a transparent contact layer in solar cells. LPCVD ZnO is used in solar cells due to its excellent high optical transparency, the low material costs, and the easy scalability of the LPCVD process to large areas. Device grade LPCVD ZnO is deposited with a rough surface in order to enable multiple reflections of the incident light (light trapping) in the solar cell, Kluth [44]. Device grade layers could not be measured with the pump probe setup because the roughness of the surface causes too much light scattering. Instead a different specimen with a LPCVD ZnO layer

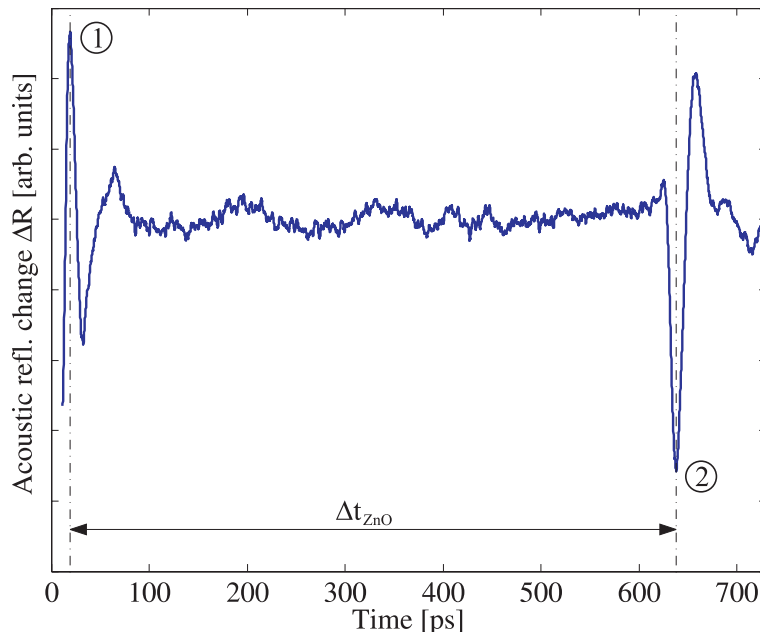


Figure 4.28: Measurement of the acoustic contribution to the reflectance change of the LPCVD ZnO specimen with flat surface and a thickness of 1716 nm. Δt_{ZnO} is the roundtrip time for the mechanical wave packet within the ZnO layer. Peak 1 corresponds to the first echo coming back from the Al-ZnO interface, peak 2 corresponds to the first echo coming back from the ZnO-Glass interface.

with flat surface is measured with the pump probe setup. By changing the parameters of the LPCVD process also flat surfaces can be achieved. By profilometry the thickness of the ZnO layer is determined to be 1716 nm and the thickness of the Al top layer is determined to be 50 nm. The pump probe measurement is shown in Fig. 4.28. After 19.3 ps the first wave packet is back at the surface being reflected at the interface Al-ZnO (denoted by '1'). Contrary to the measurements in chapters 4.4.4 to 4.4.6 here the first peak is polarized in positive direction. The reason for this is the higher acoustic impedance of the ZnO layer compared to the Al top layer. After 637.9 ps the first echo coming from the ZnO-Glass interface is back at the surface (denoted by '2'). The roundtrip time in the ZnO layer $\Delta t_{\text{ZnO}} = 618.6$ ps is given by the time difference of peak 2 and peak 1. With the measured roundtrip time the bulk wave velocity c_p of LPCVD ZnO is calculated with equation (2.2) to be 5548 m/s.

4.4.8 Sputtered ZnO

Sputtered ZnO is also a transparent conductive layer which is used in photovoltaics. The sputtering process produces layers with a flat surface. For the application in solar cells an anisotropic etching process is applied after the ZnO deposition in order to get a rough surface.

Four sputtered ZnO specimens are measured with the pump probe setup. In all four specimens the Al layers have thicknesses in the range of 50 nm and the ZnO layers have thicknesses of 210 nm. One representative pump probe measurement is

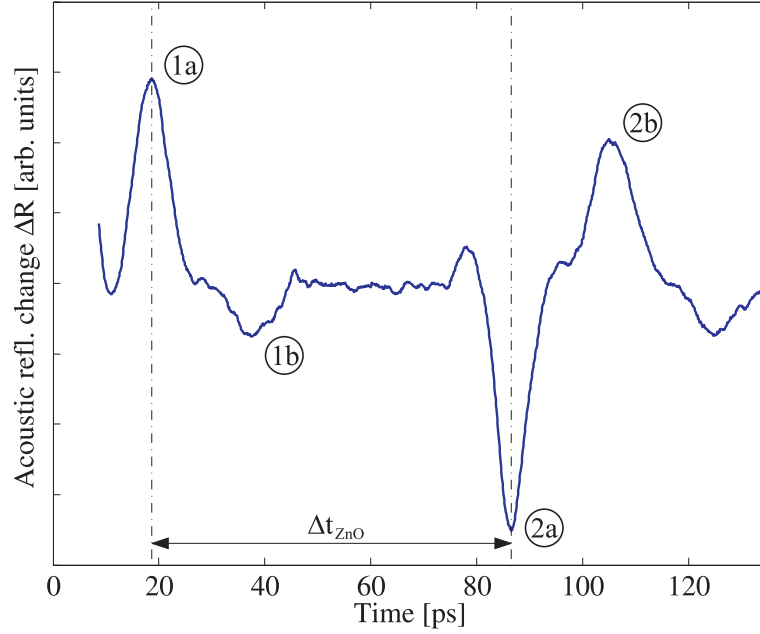


Figure 4.29: Measurement of the acoustic contribution to the reflectance change of a typical sputtered ZnO specimen. Thickness Al layer 54 nm, thickness ZnO layer 211 nm. Δt_{ZnO} is the roundtrip time for the mechanical wave packet within the ZnO layer. Peak 1a corresponds to the first echo coming back from the Al-ZnO interface, peak 1b corresponds to the second echo coming back from the Al-ZnO interface, peak 2a corresponds to the first echo coming back from the ZnO-Glass interface, peak 2b corresponds to a superposition of two wave packets described more in detail in the text.

shown in Fig. 4.29. At approximately 19 ps the first wave packet is back at the surface being reflected at the interface Al-ZnO (denoted by '1a'). Another 19 ps later, at 38 ps the second wave packet is back at the surface being reflected twice at the interface Al-ZnO (denoted by '1b'). At approximately 87 ps the first echo coming from the ZnO-Glass interface is back at the surface (denoted by '2a'). 19 ps later, at 106 ps another wave packet (denoted by '2b') is back at the surface consisting of two wave trains: Wave train one is first reflected at the Al-ZnO interface, coming back to the surface, then propagating back into the specimen and being reflected at the ZnO-Glass interface. Wave train two is first reflected at the ZnO-Glass interface, coming back to the surface, then propagating back into the specimen and being reflected at the Al-ZnO interface. The roundtrip time in the ZnO layer $\Delta t_{ZnO} = 68$ ps is given by the time difference of peak 2a and peak 1a (and also by the difference of peak 2b and peak 1b). With the measured roundtrip time and the thickness determined by profilometry the bulk wave velocity c_p then can be calculated directly with equation (2.2). The four measurements yield a bulk wave velocity of 6146 ± 74 m/s for sputtered ZnO. This value is more than 10% larger than the velocity measured in LPCVD ZnO in chapter 4.4.7. This shows that the mechanical properties of ZnO are strongly dependent on the deposition process.

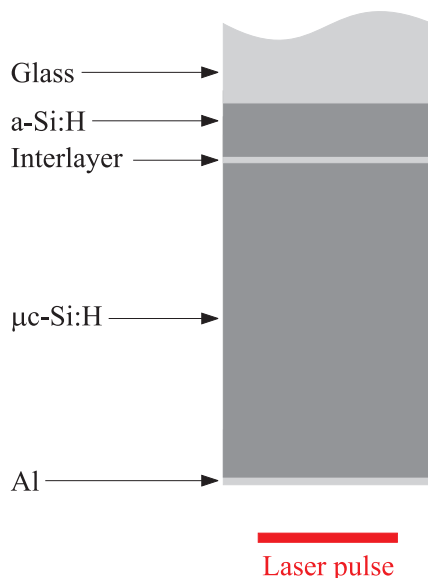


Figure 4.30: Schematic sketch of the multilayer specimen.

4.4.9 Silicon multilayer stack

In this chapter the application of pump probe measurements on a multilayer specimen containing an a-Si:H and a $\mu\text{c-Si:H}$ layer is investigated. The motivation for this investigation is the development of so called tandem solar cells consisting of two active area layers, e.g. one layer of a-Si:H and one layer of $\mu\text{c-Si:H}$. With this configuration the different absorption spectra of the two materials can be combined.

The layout of the investigated specimen is shown in Fig. 4.30: In addition to the expected layers, the pump probe measurement reveals that there must be an additional interlayer between the a-Si:H and the $\mu\text{c-Si:H}$ layers with a lower acoustic impedance than the two surrounding layers. The pump probe measurement is shown in Fig. 4.31 (upper curve). The four relevant peaks for the interpretation of the measurement are indicated with numbers from 1 to 4. Peak number 1 corresponds to the echo coming back from the interface Al - $\mu\text{c-Si:H}$, peak number 2 corresponds to the echo coming back from the interface $\mu\text{c-Si:H}$ - interlayer, peak number 3 corresponds to the echo coming back from the interface interlayer - a-Si:H, and peak number 4 corresponds to the echo coming back from the interface a-Si:H - glass. Without an interlayer peak 3 would not exist and peak 2 would be very weak because of the similar mechanical properties of a-Si:H and $\mu\text{c-Si:H}$. The pump probe experiment of this specimen is numerically simulated in order to validate this interpretation of the different peaks in the reflectance curve. The simulated reflectance is also plotted in Fig. 4.31 (lower curve). The wave propagation part of the simulation is calculated with a purely elastic model without attenuation. For this reason the shapes of the peaks and amplitude ratios of the peaks of the simulation are not perfectly matching the measurement. Nevertheless, the above interpretation is strongly confirmed. For a better understanding of the different wave trains causing the peaks in the reflectance curve, the corresponding stress field of the simulation is shown in Fig. 4.32.

For the numerical simulation the mechanical properties of a-Si:H and $\mu\text{c-Si:H}$

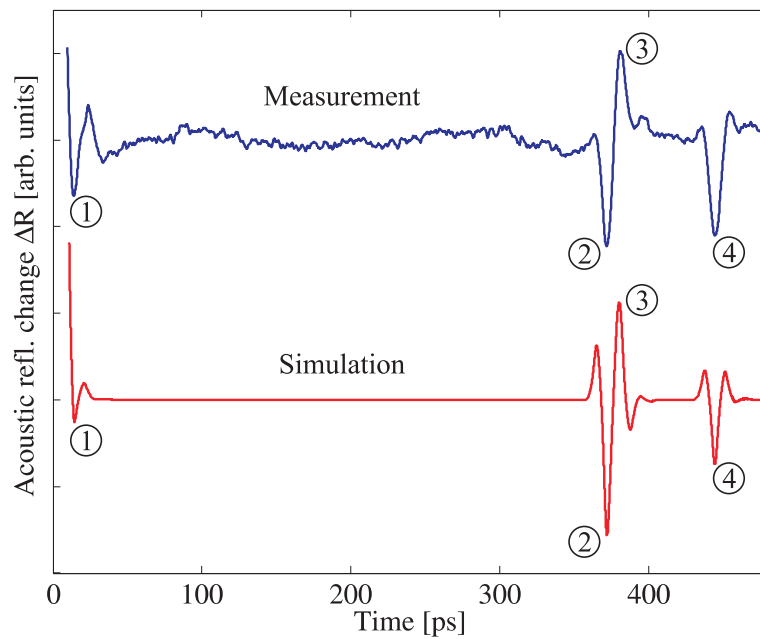


Figure 4.31: Acoustic contribution to the reflectance change of the multilayer stack shown in Fig. 4.30: Measurement and simulation with a pure elastic model for the wave propagation. The numbering of the peaks corresponds to the numbers in Fig. 4.32 where they are explained.

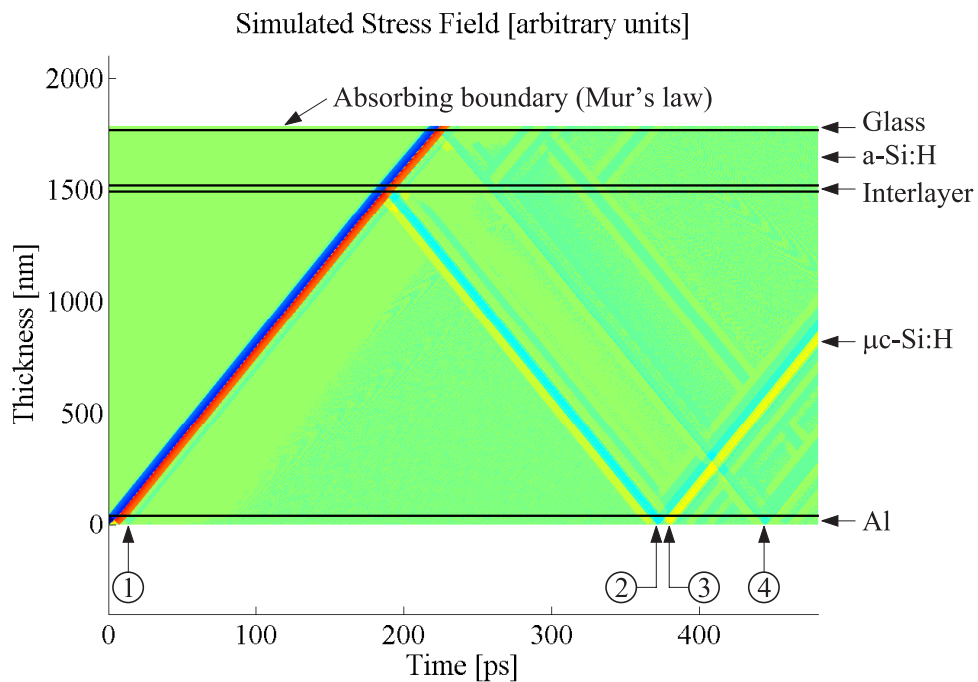


Figure 4.32: Elastic simulation of the stress field in the multilayer specimen: Excitation at time zero. Number 1: Echo coming back from the interface Al - $\mu\text{c-Si:H}$. Number 2: Echo coming back from the interface $\mu\text{c-Si:H}$ - interlayer. Number 3: Echo coming back from the interface interlayer - a-Si:H. Number 4: Echo coming back from the interface a-Si:H - glass.

given in tables 4.6 and 4.8 are used. For Al and glass the following values are taken: $E_{Al} = 71$ GPa^{*}, $\nu_{Al} = 0.34$ ^{*}, $\rho_{Al} = 2700$ kg/m³^{*}, $E_{glass} = 70$ GPa[†], $\nu_{glass} = 0.2$ [†], and $\rho_{glass} = 2500$ kg/m³[†]. The interlayer properties are chosen arbitrarily in order to have a smaller acoustic impedance than a-Si:H and μ c-Si:H: $E = 86$ GPa, $\nu = 0.22$, and $\rho = 1980$ kg/m³. Using these mechanical properties the layer thicknesses d can be calculated knowing the arrival times of the above mentioned peaks: $d_{Al} = 44$ nm, $d_{\mu c-Si:H} = 1452$ nm, $d_{Interlayer} = 32$ nm, and $d_{a-Si:H} = 245$ nm.

The interlayer could be interpreted as a transition layer created at the beginning of the μ c-Si:H deposition onto the a-Si:H layer. At this interface a tunnel recombination junction has to be created, which enables an efficient recombination of the photogenerated electrons in the top cell and the holes generated in the bottom cell. This is usually realized by defects introduced at the inner contact between the top and the bottom cell. It is quite interesting that this thin interlayer can be clearly detected. The measurement presented in Fig. 4.31 underlines the high sensitivity of the pump probe setup and its potential to gain information about both, the properties of the individual layers in a solar cell layer stack, and also about individual interfaces when combined with numerical simulations.

^{*}Hütte [20]

[†]DIN norm for float glass

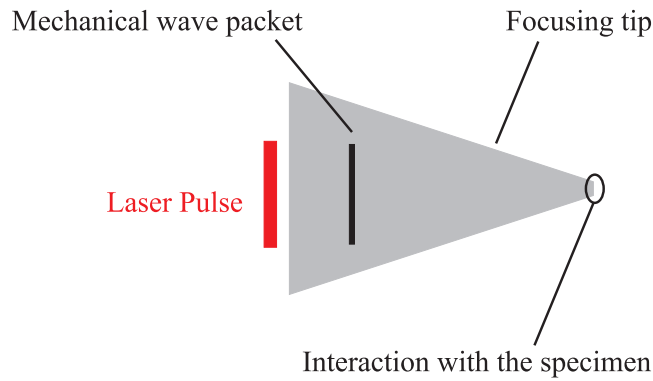


Figure 4.33: Focusing tip acting as an acoustic lens.

4.5 Wave focusing in silicon microstructures

4.5.1 Introduction

The laser acoustic pump probe technique as used in this thesis and described in chapter 3 has an excellent temporal resolution and an excellent spatial resolution in thickness direction. The temporal resolution with the 3x delay line presented in chapter 3.2.3 amounts to 20 fs. The spatial resolution in thickness direction is directly related to the wavelength of mechanical waves excited by the laser pulse. Since the duration of the laser pulses is only about 100 fs, the wavelength of the mechanical waves is governed only by the absorption length of the top layer of the specimens. Typical absorption lengths for metallic thin films are in the range of 10 to 20 nm.

On the other hand the lateral resolution of classical laser acoustic pump probe setups is limited by the wave length of the laser. In the best case the laser spot can be focused to a spot size in the order of the wave length of the laser which is 800 nm in the setup used in this thesis. Therefore, the lateral resolution is orders of magnitude larger than the resolution in thickness direction.

A focusing tip according to Fig. 4.33 acting as an acoustic lens can be a solution to enhance the lateral resolution, Profunser et al. [61], [60]. Depending on the application of a focusing tip, different criteria regarding the wave propagation properties have to be analyzed and optimized. In chapters 4.5.2 to 4.5.4 the investigations are done using numerical simulations using the 3-dimensional model presented in chapter 2.4. In chapters 4.5.6 and 4.5.7 pump probe measurements are done on silicon micro structures. This is done in order to test the feasibility regarding the monitoring of wave propagation with the collinear pump probe setup presented in chapter 3.2.

4.5.2 Focusing properties of a tip

If a tip is used as an energy focusing tool in order to transfer energy as localised as possible, the goal of the tip design is to obtain large displacements in the axial direction (z -direction in Fig. 4.34) at the sharp end for a given excitation at the base area. In this section a pyramidal structure with a quadratic base of 498x498

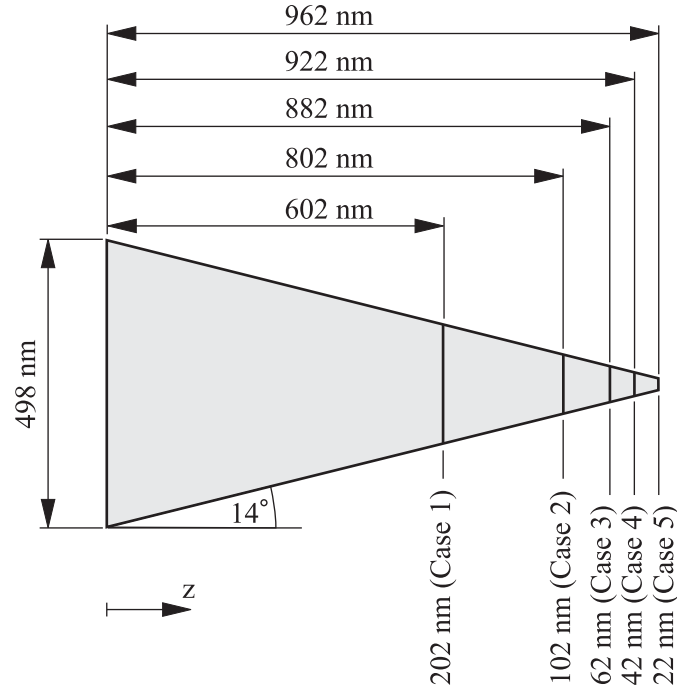


Figure 4.34: Cross-sections of the five investigated tips.

nm² and a taper angle of 14 degree is investigated. The z-axis is parallel to the [001] direction of the Si crystal. The edges of the base area are parallel to the [100] and [010] directions, respectively. The edge length at the sharp end is the variable parameter of this study. This parameter directly determines the length of the structure for a given base area and a given taper angle. Five tips (cases 1-5) with the following edge lengths at the sharp end are investigated: 202 nm, 102 nm, 62 nm, 42 nm, and 22 nm. Their cross-sections and lengths are shown in Fig. 4.34. The following parameters are used for the simulations in this section. The simulated material consists of silicon with the cubic orthotropic material properties described in section 2.4.3. The spatial discretisation is done with a step size of 2 nm in all three cartesian directions, the temporal discretisation is done with a time step of 0.1 ps. The excitation of the mechanical waves takes place at the base surface and is done by an isostatic stress field. In the middle part of the base area the lateral distribution of the excitation intensity is uniform. Towards the edges on the outermost 42 nm a hanning shaped decrease towards zero intensity is implemented. The temporal shape of the stress excitation is one sinusoidal oscillation at 80 GHz multiplied with a Hanning window. Consequently the wavelength of the primary waves is in the order 100 nm.

The laterally averaged displacement in z-direction at the sharp end of the tip is used as the criterion for the focusing quality. In Fig. 4.35 the displacement curves are plotted. The amplitudes of all cases are normalized to the maximum value of case 1. In case 1 the primary waves arrive at the sharp end mainly as plane waves because the lateral dimensions at the sharp end are larger than the wavelength of the primary waves. In contrast, in case 2 the lateral dimensions at the sharp end are of the same order as the wavelength of the primary waves and thus lead

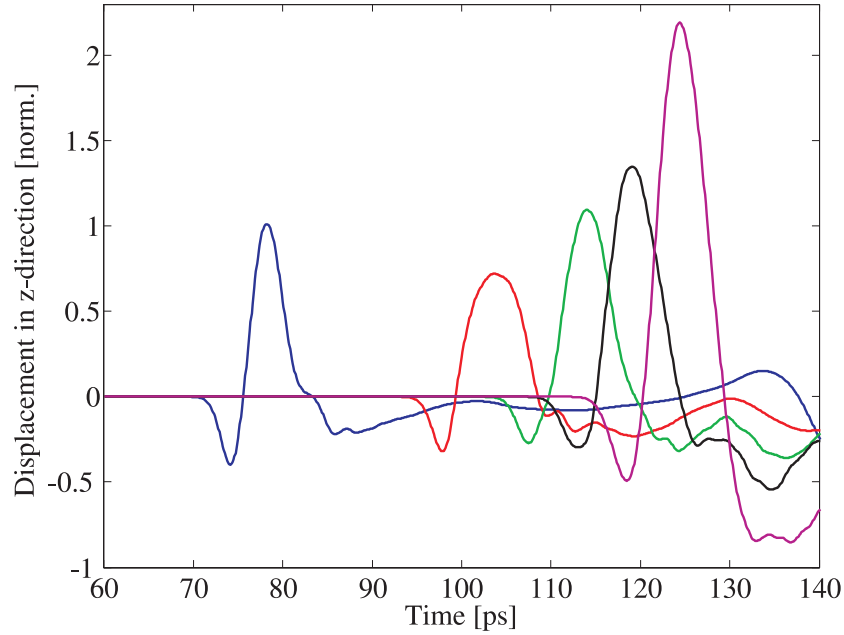


Figure 4.35: Averaged displacements in z-direction (see Fig. 4.34) at the sharp end of the tips.

to transverse resonance effects. In this case, the surface at the sharp end is not moving homogeneously. Therefore the averaged displacement of case 2 has a lower peak value and is broader. The non-uniform lateral displacement distribution at the sharp end in case 2 is shown in Fig. 4.36 for two representative time steps. For the cases 3, 4, and 5 the lateral dimensions at the sharp end are smaller than the wavelength of the primary waves. Correspondingly the displacements are more homogeneous and getting larger for smaller dimensions. Additionally, the wave front is expected to propagate slower in the areas with cross sections in the range of the dominant wave length or smaller. In the 3-dimensional continuum the velocity of longitudinal plane waves is governed by the elastic constant C_{11} , leading to a value of 8432 m/s, see table 2.2. For small cross sections the velocity is governed by the

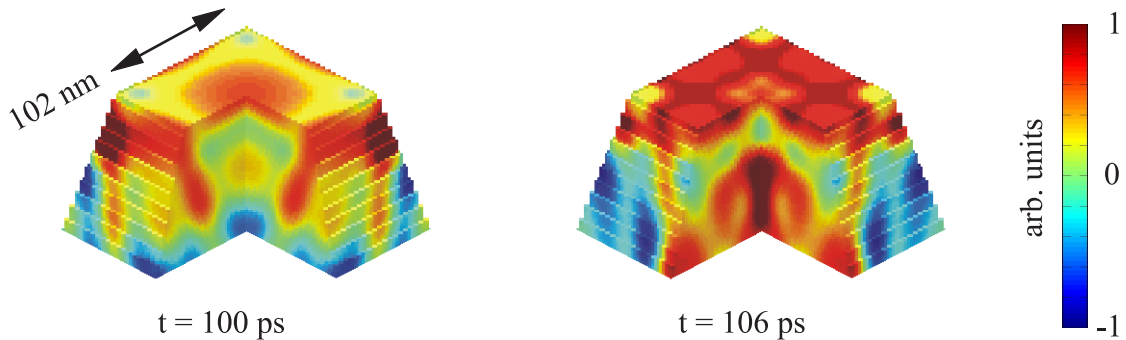


Figure 4.36: The non-uniform displacement distributions at the sharp end after 100 ps and 106 ps for case 2. The shadings correspond to the displacement in z-direction. For illustration purpose one quarter is cut out in order to see also into the structure.

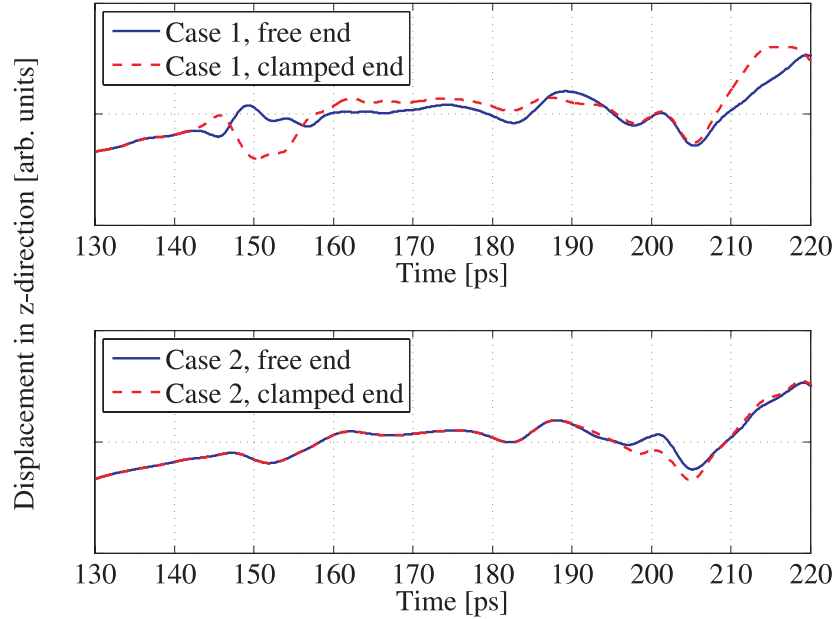


Figure 4.37: Averaged displacements in z-direction at the base surface of the tips for cases 1 and 2 as described in Fig. 4.34.

Young's modulus, leading to a value of 7472 m/s. The averaged velocities for the cases 1 to 5 calculated from the times of the peaks in Fig. 4.35 are between these two values, getting smaller for the longer pyramids: $c_{case1} = 8364$ m/s, $c_{case2} = 8235$ m/s, $c_{case3} = 8183$ m/s, $c_{case4} = 8167$ m/s, and $c_{case5} = 8139$ m/s.

In conclusion, a focusing effect for the primary waves is observed for dimensions at the sharp end which are clearly smaller than the dominant wave length.

4.5.3 Detection properties of a tip

If a tip is used as an energy focusing tool and as a detection tool at the same time, there is another important criterion for the design of the tip: The wave patterns reflected back to the base surface should be sensitive to the boundary conditions at the sharp end. Like this a measured change of these patterns (e.g. by a laser acoustic Pump-Probe experiment) can directly be related to some effects occurring at the sharp end of the tip. The sensitivity of the laser acoustic detection is related to the magnitude of strains ε_{zz} and thus related to the z-displacement at the base surface. Therefore, the change of the averaged z-displacement at the base surface for different boundary conditions at the sharp end is taken as an optimization criterion. For the cases 1 and 2 from above, the averaged z-displacements at the base surfaces are calculated for two different boundary conditions at the sharp end: The stress free boundary condition and a clamping in z-direction. These are the two extreme boundary conditions which can occur. The clamping in z-direction is implemented simply by setting the z-component of the particle velocity to zero. The results are shown in Fig. 4.37. In case 1 (upper part of Fig. 4.37) a change of the polarization can be observed between 140 and 160 ps for the free and the clamped case. These

are the primary waves reflected at the sharp end of the tip. In case 2 (lower part of Fig. 4.37) only a slight difference between the two signals is observed after about 195 ps. Such a weak variation is difficult to be reliably detected. For the cases 3, 4, and 5 the variation is even smaller (not plotted).

In conclusion only focusing tips with lateral dimensions at the sharp end which are larger than the dominant wavelength of the acoustic pulse are expected to be sensitive at the base surface to changes of the boundary conditions at the sharp end.

4.5.4 Influence of the crystallographic orientation

For the cases 1 and 5 (see Fig. 4.34) the influence of the crystallographic orientation is investigated. Taylor, Maris, and Elbaum [74] have investigated the focusing behavior of phonons in cubic orthotropic crystals. They calculated the direction dependent energy density for longitudinal phonons of a point source in lithium fluoride. Since Si has a similar ratio of the elastic constants $C_{11}:C_{12}:C_{44}$ as lithium fluoride they argue that the results are also valid for Si. They found that the focusing of longitudinal phonons is best for directions near the [111] direction and is still good for the [110] direction whereas it is weak for the [100] direction. Here, two crystallographic orientations are compared for the cases 1 and 5 (see Fig. 4.34). One configuration has the [001] direction along the z-axis (as in sections 4.5.2 and 4.5.3), the other configuration has the [011] direction along the z-axis (meaning that the crystal is rotated 45 degree around one edge of the base surface of the pyramid). The results are plotted in Fig. 4.38. The amplitudes of all cases are normalized to the maximum value of case 1 [001]. It turns out that for case 1, where the reflections at the lateral boundaries have not a big influence on the displacements at the tip, there is almost no increase of the displacements for the [011] orientation. Only the plane wave packet arrives earlier due to the faster group velocity in the [011] direction compared to the [001] direction. In case 5 the boundaries have a big influence and there is an increase of the displacements of about 50 % between the [011] and the [001] orientation. As soon as scattering at boundaries is important it seems to be an advantage to have a main plane wave propagation direction ([011] in the considered case) with a good energy density according to Taylor et al. [74].

4.5.5 Strategies for future simulations

There are various promising ideas in order to get more knowhow about the optimal tip design. Most of them require enhancements of the numerical code used for the simulations presented in the previous chapters 4.5.2 to 4.5.4. The ideas themselves and the necessary requirements for the simulation tool are shortly discussed in the following.

Arbitrary crystallographic orientations

As seen in chapter 4.5.4 the orientation of the crystallographic axes may strongly influence the focusing in the tip. The numerical code described in chapter 2.4 is limited to orientations where the stiffness coefficient tensor has the form of the matrix in equation (2.60). But for instance, the interesting configuration with the

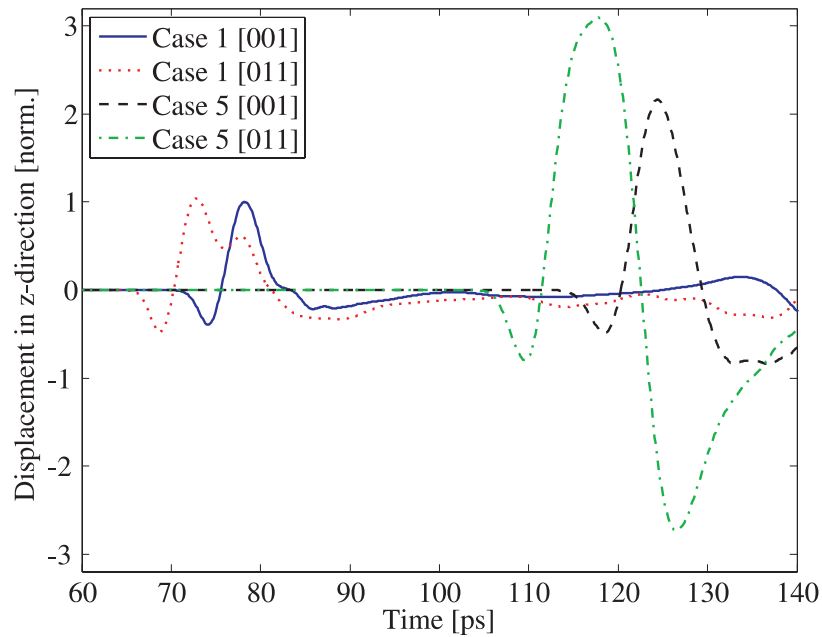


Figure 4.38: Averaged displacements in z-direction (see Fig. 4.34 for geometries) at the sharp end of the tips. The z-axis of the pyramid is either parallel to the [001] or to the [011] crystal axis.

[111] direction parallel to the z-axis has additional non-zeros entries in the stiffness coefficient tensor. For the simulation of such configurations the present FDTD code must be enhanced considerably. A step towards the simulation of arbitrary crystallographic orientations was presented by Bryner et al. [12]. As an alternative, commercial finite element (FE) tools can be used. Since for the commercial FE tool Abaqus a successful validation similar to the one in chapter 2.4.3 has been done, Abaqus is recommended for such investigations, Bochud [8].

More complex geometries

Concave or convex geometries have the potential to enhance the focusing properties of a tip. Profunser et al. showed an improvement of the focusing properties for an isotropic tip with a parabolic shape, [61]. Such simulations are possible with the code presented in chapter 2.4 as shown by Bryner et al. [11]. Nevertheless, since Abaqus offers the possibility to import CAD geometry files, Abaqus could be a more efficient alternative for parameter studies including a large amount of different geometries.

Larger geometries

The tips simulated in chapters 4.5.2 to 4.5.4 have a base area with a side length in the order of $0.5 \mu\text{m}$ and thus correspond only to the front part of real specimens. Since the wavelength of the investigated waves is in the order of 100 nm , the above simulated tips are large enough to investigate focusing phenomena of bulk waves. However, especially regarding the detection properties of a tip, it would be interest-

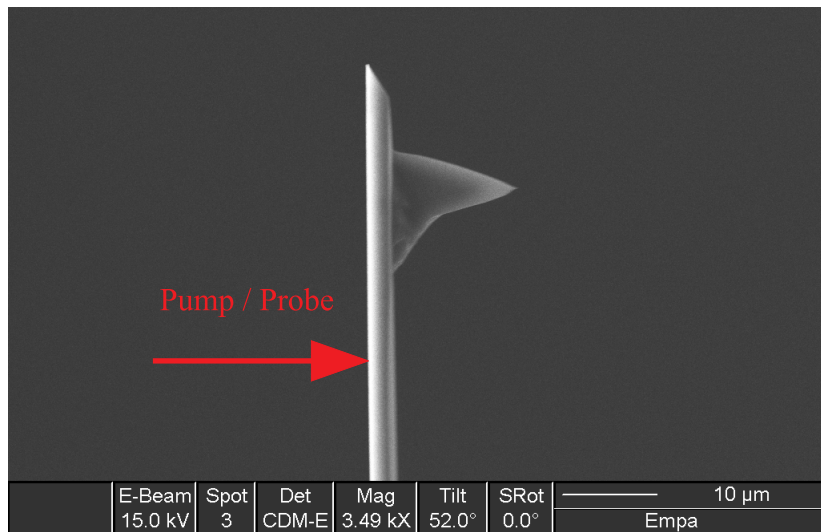


Figure 4.39: SEM image (done at the EMPA in Dübendorf) of a cantilever with AFM tip. The upper side of the cantilever (left hand side in the image) is coated with an approximately 35 nm thick Al layer.

ing to calculate the wave propagation in tips with dimensions in the range of the real specimens. For instance, the specimens investigated experimentally in chapter 4.5.7 have a side length at the base of about 5-10 μm . Numerical simulations of tips with side lengths at the base of some microns are possible with a parallelized implementation of the code presented in chapter 2.4. A C++ version parallelized with the message passing interface (MPI) has been implemented and validated on a computer cluster by Arbenz et al. [4].

4.5.6 Measurements on a cantilever

The use of micro structures as a focusing and also as a detecting tool as proposed by Profunser et al. [61], [60] requires a material in which the attenuation of the mechanical waves in the GHz regime is very small. Since due to its crystalline structure a very low attenuation is expected, silicon is a promising candidate. Additionally, there are a lot of AFM (atomic force microscopy) tips available made of Si. Here the wave propagation is investigated experimentally in the cantilever of a commercially available AFM tip (model PPP-CONTR from Nanosensors) as shown in Fig. 4.39. The cantilever has a thickness of 1.9 μm (measured by the manufacturer with 0.1 μm resolution), a width of 50 μm , and a length of 450 μm . The [100] direction of the Si crystal is parallel to the tip direction and thus parallel to the wave propagation direction of the pump probe measurement. On the top of the cantilever (Fig. 4.39 on the left) there is an approximately 35 nm thick Al layer which is optimally suited for the pump probe measurements. The measurements are performed with the collinear setup presented in chapter 3.2. A typical measurement is shown in Fig. 4.40. The equally spaced vertical lines denote the times of arrival of the wave packets back at the top surface. The main frequency content of the packets is in the range of 58 GHz. The time between two packets amounts to 456.5 ps. The single wave packets consist of an increasing number of multiple oscillations. These oscil-

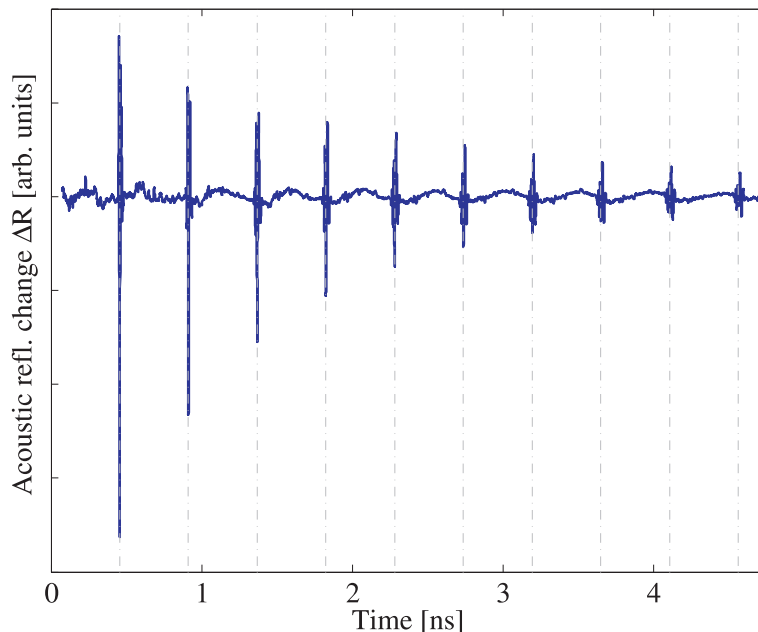


Figure 4.40: Measurement of the acoustic contribution to the reflectance change of a Si cantilever with a thickness in the range of $2\ \mu\text{m}$ and an approximately $35\ \text{nm}$ thick Al top layer. The equally spaced vertical lines denote the times of arrival of the wave packets at the surface.

lations are caused by multiple reflections within the top Al layer. They are quite weak due to the similar acoustic impedance of Si and Al. The $456.5\ \text{ps}$ correspond to the travel time through both the Al layer and the Si structure. The travel time through the Al layer can be determined by looking at the first $25\ \text{ps}$ of the pump probe measurement. In Fig. 4.41 the first $25\ \text{ps}$ are plotted of the measurement of Fig. 4.40. The travel time through the Al layer amounts to $11.3\ \text{ps}$. By subtracting this value from the total travel time through both materials the travel time for the Si part is calculated to be $445.2\ \text{ps}$. Taking $8432\ \text{m/s}$ for the bulk wave velocity in Si [100] (table 2.2), the thickness of the cantilever is calculated to be $1.88\ \mu\text{m}$. This corresponds very well to the $1.9\ \mu\text{m}$ measured by the manufacturer.

As can be seen in Fig. 4.40, ten packets can be detected without any problems. The tenth packet traveled in total through approximately $19\ \mu\text{m}$ Si and $350\ \text{nm}$ Al and still provides a clear signal. Therefore AFM tips made of crystalline Si with lengths in the range of 15 to $20\ \mu\text{m}$ seem to be optimally suited for investigating wave propagation phenomena in the GHz regime.

4.5.7 Measurements in cut AFM tips

In this chapter measurements in cut AFM tips are presented. Similar to the tips used and described by Profunser [60], these tips are cut with the FIB (focused ion beam) technique, Gasser et al. [34]. The FIB cutting was done at the EMPA Dübendorf at the department of electronics, metrology, and reliability. In contrast to the work of Profunser [60], here a collinear pump probe setup as presented in chapter 3.2 is applied for the measurements. So, as a step towards the setup shown in Fig. 4.33,

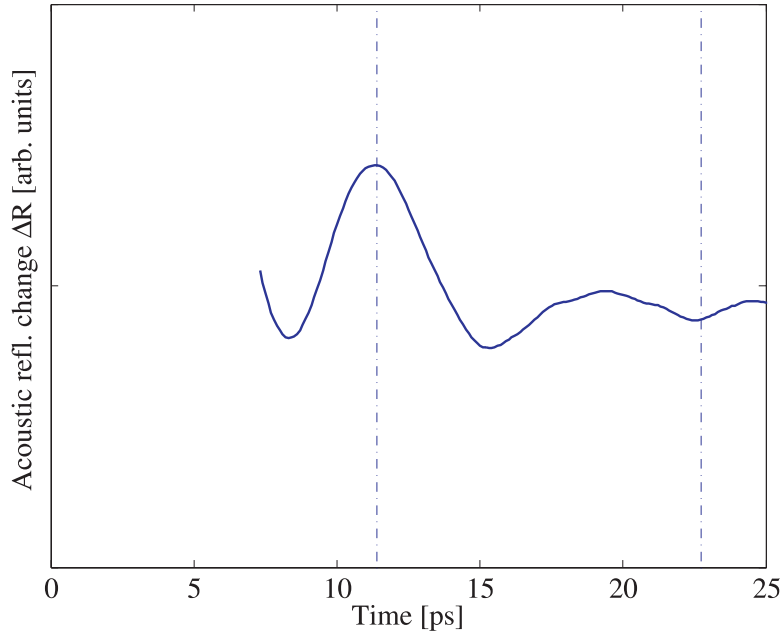


Figure 4.41: Measurement of the acoustic contribution to the reflectance change of a Si cantilever with a thickness in the range of $2\ \mu\text{m}$ and an approximately $35\ \text{nm}$ thick Al top layer. Zoomed view of the first 25 ps. The vertical lines denote the first and the second Al peak.

the excitation and the detection of the mechanical waves is done on the same side of the specimen. A typical cut AFM tip and the configuration of the measurement is shown in Fig. 4.42. 4 specimens are measured with increasing tip lengths, see Fig. 4.43. They have the following lengths including the cantilever thickness: Tip 1: $5.50\ \mu\text{m}$. Tip 2: $8.21\ \mu\text{m}$. Tip 3: $10.41\ \mu\text{m}$. Tip 4: $12.46\ \mu\text{m}$. The corresponding sizes of the cross sections at the cutting positions are given directly in Fig. 4.43 on the right.

For tip number 1 three echoes are recorded within a time window of 4.8 ns, for tip 2 two echoes are recorded, and for tip 3 and 4 one echo is recorded. With increasing length of the tips the measured signal of the echoes is getting weaker (all 4 measurements are done with the same settings). One reason for this is the attenuation of the mechanical waves. Another reason is the diameter of the laser spot which is estimated to be in the range of $3\text{-}5\ \mu\text{m}$. This means for the longer tips with cross sections at the sharp end smaller than $3\text{-}5\ \mu\text{m}$, that not the entire plane wave is reflected at a plane surface. A part of the wave is reflected at the flanks of the tip and thus not coming back at the same time as the first packet reflected at the sharp end of the tip. In Fig. 4.44 zoomed views of the first echoes from the measurements in Fig. 4.43 are shown. They are all normalized to their maximum amplitude. The shape of all four echoes is very similar. This indicates that in all four tips the wave packets reflected at the cut surface still propagate mainly as plane waves. The reflections from the flanks mentioned above are too weak or too much scattered and could therefore not be detected with the presented measurements.

Nevertheless, even for the longest tip (number 4) a clear signal of the main echo is recorded. This clearly indicates the feasibility of launching mechanical waves and

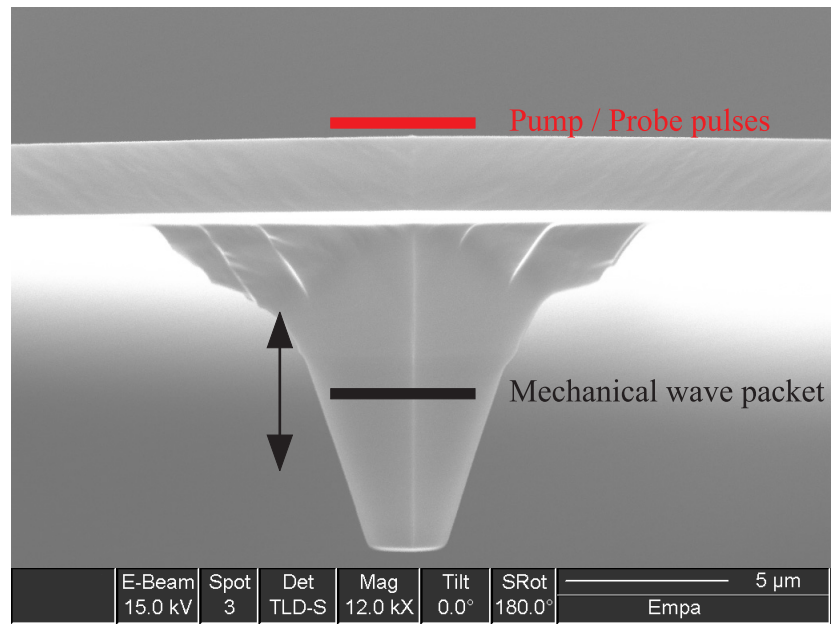


Figure 4.42: SEM image (done at the EMPA in Dübendorf) of a cut AFM tip.

detecting their reflections in the GHz regime in cut silicon AFM tips.

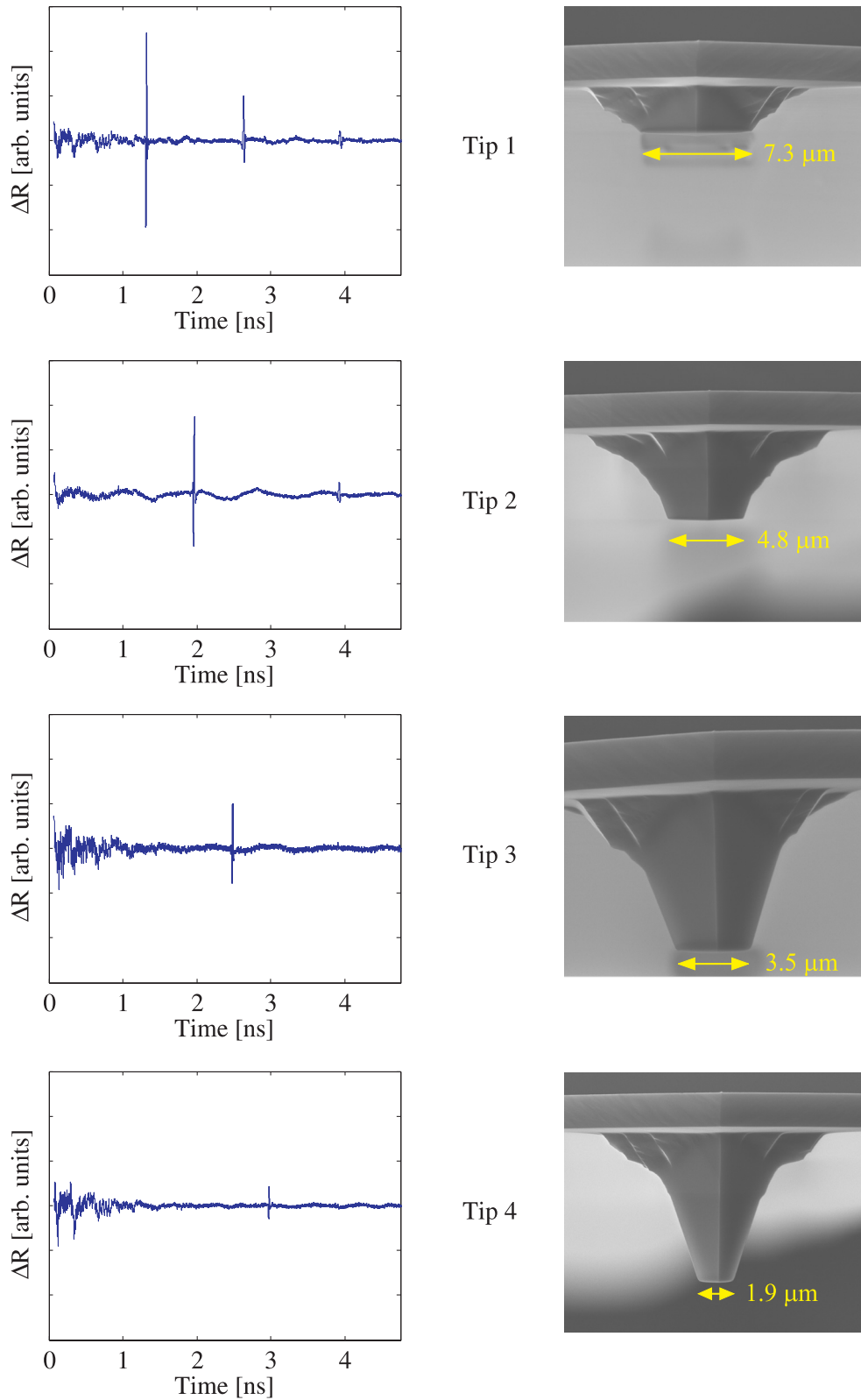


Figure 4.43: Left: Measurements of the acoustic contribution to the reflectance change of 4 cut AFM tips with different lengths. The same scaling is used for all 4 cases. Right: SEM images of the 4 corresponding tips. They have the following lengths including the cantilever thickness: Tip 1: 5.61 μm . Tip 2: 8.36 μm . Tip 3: 10.58 μm . Tip 4: 12.66 μm .

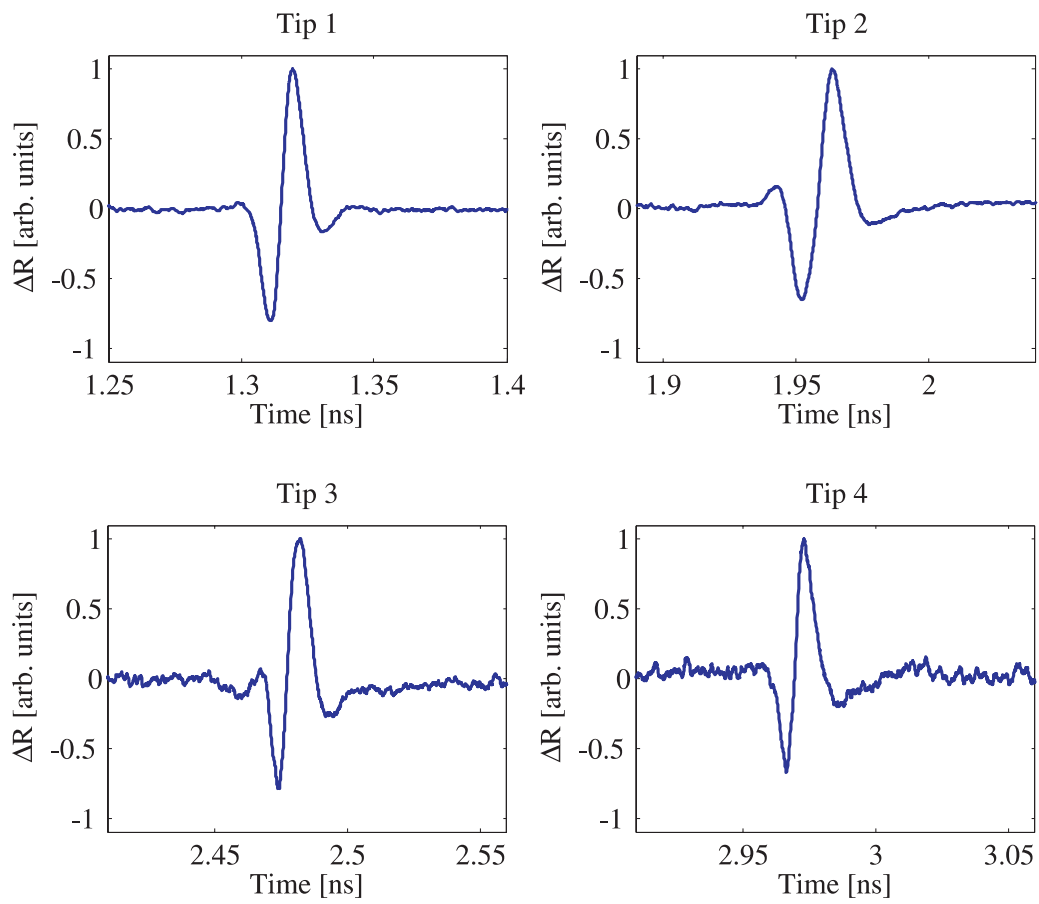


Figure 4.44: Zoomed views of the first echoes of the measurements shown in Fig. 4.43. The signals are normalized to their maximum amplitude.

5 Conclusions and outlook

5.1 Theory and modeling

A complete model for the simulation of pump probe measurements is presented including the excitation, the wave propagation, and the detection. The wave propagation part is modeled with a viscoelastic model based on the standard linear solid. Compared to the purely elastic model the viscoelastic model increases the field of applications of the simulation tool. By fitting such simulations to measurements it is possible to quantify the attenuation in specimens where various reflectance peaks are superimposed to each other, for instance in polymer films buried under an Al top layer. Additionally, the fitting procedure with the viscoelastic model enables a reliable thickness measurement of specimens where the layer of interest has a similar thickness as the Al top layer. In these cases the peaks in the reflectance measurements are not isolated and therefore cannot directly be assigned to certain wave packets. By fitting the viscoelastic simulation to such measurements the times of arrival of the different wave packets can reliably be determined.

For the wave propagation part also a 3-dimensional model is presented. With this model the wave propagation in elastic cubic orthotropic materials as for example crystalline Si can be simulated. The numerical code is validated successfully for 3 different test criteria. First the wave velocities of plane waves with different propagation directions and different polarizations are compared with analytical results. The energy is used as a second criterion. Long term simulations show that the energy remains constant. This indicates that the code is stable and physically reasonable. A third validation is done for an isotropic pyramid. For long wavelengths the displacement amplitudes are successfully compared with an analytical model. However, the code in its present form has some limitations regarding the flexibility of the orientation of the orthotropic axes. Strategies for future approaches are discussed in detail in chapter 4.5.5.

The influence of the temperature distribution within a specimen on the reflectance change at the surface is a topic which could be incorporated in the simulation tool in future. Whereas this thesis focused mainly on the mechanical characterization of specimens, such an enhancement of the simulation tool could lead to additional opportunities in the field of thermo-acoustic characterization.

5.2 Experimental setup

The former basic setup with convex lenses and a delay line with two single mirrors is enhanced regarding three properties: The focusing is improved, the maximum time window of a measurement is increased, and the beam walking is reduced.

The focusing of the laser is improved with a reduction of the spot size from 100 μm to 3-5 μm . This is achieved by a collinear beam guidance and the use of a microscope objective instead of two simple convex lenses. By the replacement of the two single mirrors of the translation stage with two retroreflectors the maximum time window of a measurement is increased by a factor of 3 and simultaneously the beam walking is reduced significantly. Additionally the adjustment procedure of the pump and probe beam is simplified by the use of a camera which is coupled into the microscope objective.

The nature of future improvements of the experimental setup is directly coupled to the required maximum time window of a measurement. For shorter time windows in the range of up to 2 ns there is the asynchronous optical sampling technique (ASOPS) which enables pump probe measurements without a mechanical delay line. ASOPS works with two mode locked lasers operated with two slightly different repetition rates, Bartels et al. [5], Dekorsy et al. [23]. One of the lasers is used as pump beam, the other laser is used as probe beam, both of them are guided with fixed optical paths to the specimen. The temporal shift is achieved by the different repetition rates. The elimination of the delay line eliminates any variations of the beam positions during a measurement and thus increases the accuracy. Additionally, the measurements are faster since no movements of mechanical parts are involved. Additionally, an online optimization of the measurement parameters for the whole time window of the measurement is possible since the time window is scanned with several kHz. In the paper of Dekorsy et al. [23] pump probe measurements are reported with a time window of 1 ns and a temporal resolution of 200 fs. In the meantime systems with time windows of 2 ns are available.

For future investigations of multiple reflections of mechanical waves in micro structures such as AFM tips a larger time window for the measurements could be of interest. For the increase of the present maximum time window of 5 ns the use of a delay line with more than 3 roundtrips is a straight forward approach. By changing the position of the retroreflectors, the number of roundtrips can be increased, see chapter 3.2.3.

5.3 Experimental results

Aluminum thin films

Al thin films are investigated regarding their attenuation behavior in the GHz regime. It turned out that there is a significant attenuation and it is strongly dependent on the thin film deposition process. The attenuation α measured in a sputtered Al film is about 3 times higher than in an Al film deposited by e-beam evaporation. These facts have an impact on the analysis of functionally graded layers buried under an Al transducer layer. Since the Al transducer layer influences the frequency dependent behavior of the system, the attenuation behavior of the specific transducer layers must be first analyzed separately. Then the frequency dependent properties of the underlying functionally graded layers can be analyzed.

Polymer films

Several polymer films are analyzed regarding their bulk wave velocity and their attenuation. An interesting result is that in the range of 50 GHz the attenuation in PMMA films is not significantly higher than in Al films. Therefore PMMA films with thicknesses of up to 600 nm are measured without any problems. At the other end of the thickness range specimens with film thicknesses down to 9 nm are measured with the pump probe setup in combination with the fitting procedure of the viscoelastic simulation. For these very thin films the highest uncertainty lies in the thickness measurements by profilometry or ellipsometry.

For PMMA films thinner than approximately 80 nm an increase of the bulk wave velocity is observed. Additionally, the underlying layer has an influence on the bulk wave velocity of very thin PMMA films: The use of a HDMS primer layer reduces the bulk wave velocity. Additional measurements of such specimens would be very interesting in order to get more quantitative results.

The glass transition temperature of thin PMMA films used for nanoimprinting is a very important parameter for the imprinting process. As a future project, by a combination of the pump probe setup and a regulated temperature stage the glass transition temperature could be directly determined on thin films.

Structured polymer specimens

For structured specimens with lateral feature sizes down to several microns the pump probe setup can be used for thickness determination. This is shown for line structures with a width of 100 μm and for 10 μm square dots. By a scanning process a thickness map can be created for the area of interest.

The pump probe setup can also be applied to specimens with submicron patterns in order to check the quality of the imprinted features. The single features cannot be resolved, but nevertheless the resonance frequencies of different areas of the specimen can be monitored and be used as a relative criterion for the quality of the specimen. This is shown for imprinted holes with a nominal lateral size in the range of 250 nm.

Solar cell materials

The pump probe setup is successfully used for the determination of the bulk wave velocity in thin film layers used for solar cells.

For both, amorphous and microcrystalline silicon films, the determined mechanical properties as bulk wave velocity, Young's modulus, and density significantly differ from the values for crystalline bulk material. The bulk wave velocity of the amorphous silicon films is found to be 8.4% smaller, and that of microcrystalline silicon films is found to be 3.7% smaller than the value for crystalline silicon [100]. Additionally, for a-Si:H and $\mu\text{c-Si:H}$ the Young's modulus is measured by nanoindentation. The Young's modulus is found to be more than 13% higher for the $\mu\text{c-Si:H}$ film than for the a-Si:H film. A pump probe measurement series of $\mu\text{c-Si:H}$ specimens with varying crystalline volume fraction shows a relation between the bulk wave velocity and the crystalline volume fraction: The bulk wave velocity increases with increasing crystalline volume fraction.

Measurements of differently deposited ZnO layers show the strong influence of the deposition process on their mechanical properties. The bulk wave velocity of sputtered ZnO is more than 10% larger than the value of LPCVD ZnO.

For a multilayer specimen it has been shown that the a-Si:H and the $\mu\text{c-Si:H}$ layers can be measured individually with a single pump probe measurement and interface layers can be detected. As a future project, the photovoltaic performance of tandem stacks consisting of a-Si:H and $\mu\text{c-Si:H}$ could be related to the mechanical properties of the individual layers by pump probe measurements directly on the multilayer. Such measurements could be used for quality inspection purposes on solar cells.

Silicon microstructures

With the collinear pump probe setup it is possible to excite and to measure Si cantilevers and AFM tips from the same side. Ten roundtrips of a mechanical wave packet can easily be detected with a very good signal quality in a cantilever with a thickness of 1.9 μm . For a series of four cut AFM tips with different lengths a mechanical wave packet is excited and its reflections are detected. Again, the signal of the reflected waves has a very good quality. This shows the feasibility of launching and detecting waves in the GHz regime in 3-dimensional micro structures.

As a next step, measurements of tips with cross sections at the sharp end in the sub micron range should be performed in order to go towards smaller lateral dimensions. Measurements with tips being in contact with an object should yield indications about the sensitivity regarding changes of the boundary conditions at the sharp end of the tip.

A Appendix

A.1 Parameters used for the two temperature model

	Al film simulated in chapter 4.1.4	Al film simulated in chapter 4.2.4
Heat capacity of the lattice C_l [J/m ³ K]	2.39×10^6 ^a	2.39×10^6 ^a
Heat capacity of the electrons C_e [J/m ³ K]	2.76×10^4 ^a	2.76×10^4 ^a
Thermal conductivity of the electrons K_e [W/mK]	237 ^a	237 ^a
Electron-phonon coupling factor G [W/m ³ K]	4.35×10^{17} ^b	4.35×10^{17} ^b
Thermal expansion coefficient α_{th} [1/K]	23.1×10^{-6} ^a	23.1×10^{-6} ^a
Complex refraction index n^* [-]	$1.30 + 5.75i$ ^c	$1.72 + 6.46i$ ^c

Table A.1: Al films simulated in chapters 4.1.4 and 4.2.4: Material properties used for the simulations of the excitation with the two temperature model.

^aProfunser [60]

^bRichardson et al. [64]

^cMeasured by ellipsometry

References

- [1] International technology roadmap for semiconductors 2005 edition. <http://www.itrs.net/LINKS/2005ITRS/LITHO2005.pdf>.
- [2] AEBI, L., SCHWANK, L., VOLLMANN, J., BRYNER, J., WENKE, I., AND DUAL, J. High resolution measurement of fgm thin films using picosecond ultrasonics. *Conference proceeding, International Congress on Ultrasonics, Santiago* (2009).
- [3] AHN, S. W., LEE, K. D., KIM, D. H., AND LEE, S. S. Polymeric wavelength filter based on a bragg grating using nanoimprint technique. *Ieee Photonics Technology Letters* 17, 10 (2005), 2122–2124.
- [4] ARBENZ, P., BRYNER, J., AND TOBLER, C. Parallelized transient elastic wave propagation in orthotropic structures. *Conference proceeding, PPAM2009, Wroclaw* (2009).
- [5] BARTELS, A., HUDERT, F., JANKE, C., DEKORSY, T., AND KOHLER, K. Femtosecond time-resolved optical pump-probe spectroscopy at kilohertz-scan-rates over nanosecond-time-delays without mechanical delay line. *Applied Physics Letters* 88, 4 (2006).
- [6] BELOTTI, M., TORRES, J., ROY, E., PEPIN, A., GERACE, D., ANDREANI, L. C., GALLI, M., AND CHEN, Y. Fabrication of soi photonic crystal slabs by soft uv-nanoimprint lithography. *Microelectronic Engineering* 83, 4-9 (2006), 1773–1777.
- [7] BIENVILLE, T., ROBILLARD, J. F., BELLIARD, L., ROCH-JEUNE, I., DEVOS, A., AND PERRIN, B. Individual and collective vibrational modes of nanostructures studied by picosecond ultrasonics. *Ultrasonics* 44 (2006), E1289–E1294. Suppl. 1.
- [8] BOCHUD, N. *Investigations of the wave propagation in tip-like structures*. Master Thesis ETH. Zurich, 2008.
- [9] BRETZ, K. C., LEE, Y. C., KRAUSS, T. D., WISE, F. W., AND SACHSE, W. H. Picosecond acoustics for the characterization of sub-micron polymeric films. *Ultrasonics* 34, 2-5 (1996), 513–515.
- [10] BRYNER, J., KEHOE, T., VOLLMANN, J., AEBI, L., WENKE, I., AND DUAL, J. Phonon attenuation in the ghz regime: Measurements and simulations with

- a visco-elastic material model. *Conference proceeding, International Congress on Ultrasonics, Santiago* (2009).
- [11] BRYNER, J., VOLLMANN, J., AEBI, L., AND DUAL, J. Wave propagation in pyramidal tip-like structures with cubic material properties. *Accepted for publication, Wave Motion* (2009).
- [12] BRYNER, J., VOLLMANN, J., BUGNARD, G., AND DUAL, J. 3-d wave propagation in anisotropic microstructures with tilted orthotropic axes. *Conference proceeding, International Congress on Ultrasonics, Vienna* (2007).
- [13] BURSIKOVA, V., SLADEK, P., ST'ACHEL, P., AND BURSIK, J. Mechanical properties of thin silicon films deposited on glass and plastic substrates studied by depth sensing indentation technique. *Journal of Non-Crystalline Solids* 352, 9-20 (2006), 1242–1245.
- [14] CAGLAR, O. *Mechanical characterization of thin-film materials used in photovoltaics*. Master Thesis ETH. Zurich, 2008.
- [15] CATCHPOLE, K. R., AND POLMAN, A. Plasmonic solar cells. *Optics Express* 16, 26 (2008), 21793–21800.
- [16] CHINMULGUND, M., INTURI, R. B., AND BARNARD, J. A. Effect of ar gas pressure on growth, structure, and mechanical properties of sputtered ti, al, tial, and ti3al films. *Thin Solid Films* 270, 1-2 (1995), 260–263.
- [17] CHOU, S. Y., AND KRAUSS, P. R. Imprint lithography with sub-10 nm feature size and high throughput. *Microelectronic Engineering* 35, 1-4 (1997), 237–240.
- [18] CHOU, S. Y., KRAUSS, P. R., AND RENSTROM, P. J. Imprint of sub-25 nm vias and trenches in polymers. *Applied Physics Letters* 67, 21 (1995), 3114–3116.
- [19] CHRISTENSEN, R. *Theory of Viscoelasticity*. Academic Press, 1971.
- [20] CZICHOS, H. *Hütte: Die Grundlagen der Ingenieurwissenschaften*, vol. 31. Springer, 2000.
- [21] DECREMPS, F., BELLIARD, L., PERRIN, B., AND GAUTHIER, M. Sound velocity and absorption measurements under high pressure using picosecond ultrasonics in a diamond anvil cell: Application to the stability study of alpdmn. *Physical Review Letters* 100, 3 (2008).
- [22] DEHOUX, T., CHIGAREV, N., ROSSIGNOL, C., AND AUDOIN, B. Three-dimensional elasto-optical interaction for reflectometric detection of diffracted acoustic fields in picosecond ultrasonics. *Physical Review B* 76, 2 (2007).
- [23] DEKORSY, T., HUDERT, F., CERNA, R., SCHAFER, H., JANKE, C., BARTELS, A., KOHLER, K., BRAUN, S., WIEMER, M., AND MANTL, S. Coherent

- acoustic phonons in nanostructures investigated by asynchronous optical sampling - art. no. 63930h. *Nanophotonics for Communication: Materials, Devices, and Systems III 6393* (2006), H3930–H3930.
- [24] DEKORSY, T., TAUBERT, R., HUDERT, F., BARTELS, A., HABENICHT, A., MERKT, F., LEIDERER, P., KOHLER, K., SCHMITZ, J., AND WAGNE, J. Coherent acoustic phonons in nanostructures - art. no. 68920e. *Ultrafast Phenomena in Semiconductors and Nanostructure Materials Xii 6892* (2008), E8920–E8920.
- [25] DROZ, C. *Thin Film Microcrystalline Silicon Layers and Solar Cells: Microstructure and Electrical Performances*. Doctoral Thesis, University of Neuchatel. Neuchatel, 2003.
- [26] DUMOND, J. J., LOW, H. Y., AND RODRIGUEZ, I. Isolated, sealed nanofluidic channels formed by combinatorial-mould nanoimprint lithography. *Nanotechnology 17*, 8 (2006), 1975–1980.
- [27] EVERY, A. G. General, closed-form expressions for acoustic-waves in cubic-crystals. *Physical Review Letters 42*, 16 (1979), 1065–1068.
- [28] EVERY, A. G., AND KIM, K. Y. Time-domain dynamic-response functions of elastically anisotropic solids. *Journal of the Acoustical Society of America 95*, 5 (1994), 2505–2516.
- [29] EVERY, A. G., AND SACHSE, W. Determination of the elastic-constants of anisotropic solids from acoustic-wave group-velocity measurements. *Physical Review B 42*, 13 (1990), 8196–8205.
- [30] EVERY, A. G., AND SACHSE, W. Imaging of laser-generated ultrasonic-waves in silicon. *Physical Review B 44*, 13 (1991), 6689–6699.
- [31] EVERY, A. G., SACHSE, W., KIM, K. Y., AND THOMPSON, M. O. Phonon focusing and mode-conversion effects in silicon at ultrasonic frequencies. *Physical Review Letters 65*, 12 (1990), 1446–1449.
- [32] FELLINGER, P., MARKLEIN, R., LANGENBERG, K. J., AND KLAHOLZ, S. Numerical modeling of elastic-wave propagation and scattering with efit - elastodynamic finite integration technique. *Wave Motion 21*, 1 (1995), 47–66.
- [33] FRYER, D. S., PETERS, R. D., KIM, E. J., TOMASZEWSKI, J. E., DE PABLO, J. J., NEALEY, P. F., WHITE, C. C., AND WU, W. L. Dependence of the glass transition temperature of polymer films on interfacial energy and thickness. *Macromolecules 34*, 16 (2001), 5627–5634.
- [34] GASSER, P., KLOTZ, U. E., KHALID, F. A., AND BEFFORT, O. Site-specific specimen preparation by focused ion beam milling for transmission electron microscopy of metal matrix composites. *Microscopy and Microanalysis 10*, 2 (2004), 311–316.

- [35] GRAFF, K. *Wave Motion in elastic solids*. 1975.
- [36] GSELL, D., LEUTENEGGER, T., AND DUAL, J. Modeling three-dimensional elastic wave propagation in circular cylindrical structures using a finite-difference approach. *Journal of the Acoustical Society of America* 116, 6 (2004), 3284–3293.
- [37] HOSTETLER, J. L., SMITH, A. N., CZAJKOWSKY, D. M., AND NORRIS, P. M. Measurement of the electron-phonon coupling factor dependence on film thickness and grain size in au, cr, and al. *Applied Optics* 38, 16 (1999), 3614–3620.
- [38] HU, W., YIM, E. K. F., REANO, R. M., LEONG, K. W., AND PANG, S. W. Effects of nanoimprinted patterns in tissue-culture polystyrene on cell behavior. *Journal of Vacuum Science and Technology B* 23, 6 (2005), 2984–2989.
- [39] HURLEY, D. H., AND WRIGHT, O. B. Detection of ultrafast phenomena by use of a modified sagnac interferometer. *Optics Letters* 24, 18 (1999), 1305–1307.
- [40] HURLEY, D. H., WRIGHT, O. B., MATSUDA, O., GUSEV, V. E., AND KOLOSOV, O. V. Laser picosecond acoustics in isotropic and anisotropic materials. *Ultrasonics* 38, 1-8 (2000), 470–474.
- [41] JUNG, Y. G., LAWN, B. R., MARTYNIUK, M., HUANG, H., AND HU, X. Z. Evaluation of elastic modulus and hardness of thin films by nanoindentation. *Journal of Materials Research* 19, 10 (2004), 3076–3080.
- [42] KEHAGIAS, N., CHANSIN, G., REBOUD, V., ZELSMANN, M., SCHUSTER, C., KUBENZ, M., REUTHER, F., GRUETZNER, G., AND TORRES, C. M. S. Embedded nano channels fabricated by non-selective reverse contact uv nanoimprint lithography technique. *Microelectronic Engineering* 84, 5-8 (2007), 921–924.
- [43] KEHOE, T., BRYNER, J., REBOUD, V., VOLLMANN, J., AND TORRES, C. M. S. Physical properties of thin nanoimprint polymer films measured by photoacoustic metrology. *Conference proceeding, SPIE Advanced Lithography, San Jose* (2009).
- [44] KLUTH, O. *Texturierte Zinkoxidschichten für Silizium-Dünnschichtsolarzellen*. Diss. RWTH Aachen. Berichte des Forschungszentrums Jülich, 3928, ISSN 0944-2952, Aachen, 2001.
- [45] LEE, Y. C., BRETZ, K. C., WISE, F. W., AND SACHSE, W. Picosecond acoustic measurements of longitudinal wave velocity of submicron polymer films. *Applied Physics Letters* 69, 12 (1996), 1692–1694.
- [46] LEUTENEGGER, T., AND DUAL, J. Detection of defects in cylindrical structures using a time reverse method and a finite-difference approach. *Ultrasonics* 40, 1-8 (2002), 721–725.

-
- [47] LIN, H. N., MARIS, H. J., FREUND, L. B., LEE, K. Y., LUHN, H., AND KERN, D. P. Study of vibrational-modes of gold nanostructures by picosecond ultrasonics. *Journal of Applied Physics* 73, 1 (1993), 37–45.
- [48] MADARIAGA, R. Dynamics of an expanding circular fault. *Bulletin of the Seismological Society of America* 66, 3 (1976), 639–666.
- [49] MATSUDA, O., WRIGHT, O. B., HURLEY, D. H., GUSEV, V., AND SHIMIZU, K. Coherent shear phonon generation and detection with picosecond laser acoustics. *Physical Review B* 77, 22 (2008).
- [50] MATSUDA, O., WRIGHT, O. B., HURLEY, D. H., GUSEV, V. E., AND SHIMIZU, K. Coherent shear phonon generation and detection with ultrashort optical pulses. *Physical Review Letters* 93, 9 (2004).
- [51] MEILLOUD, F. *Introduction to thin film silicon*. Powerpoint presentation, thin film PV school IMT. 2008.
- [52] MIZUBAYASHI, H., YAMAGUCHI, T., AND YOSHIHARA, Y. An elasticity study of al and ag nanometer films. *Journal of Alloys and Compounds* 212 (1994), 446–450.
- [53] MIZUBAYASHI, H., YOSHIHARA, Y., AND OKUDA, S. The elasticity measurements of aluminum nm-films. *Physica Status Solidi a-Applied Research* 129, 2 (1992), 475–481.
- [54] MORATH, C. J., AND MARIS, H. J. Phonon attenuation in amorphous solids studied by picosecond ultrasonics. *Physical Review B* 54, 1 (1996), 203–213.
- [55] OLIVER, W. C., AND PHARR, G. M. An improved technique for determining hardness and elastic-modulus using load and displacement sensing indentation experiments. *Journal of Materials Research* 7, 6 (1992), 1564–1583.
- [56] OLIVER, W. C., AND PHARR, G. M. Measurement of hardness and elastic modulus by instrumented indentation: Advances in understanding and refinements to methodology. *Journal of Materials Research* 19, 1 (2004), 3–20.
- [57] PERRIN, B., BONELLO, B., JEANNET, J. C., AND ROMATET, E. Interferometric detection of hypersound waves in modulated structures. *Progress in Natural Science* 6 (1996), S444–S448.
- [58] PERRIN, B., ROSSIGNOL, C., BONELLO, B., AND JEANNET, J. C. Interferometric detection in picosecond ultrasonics. *Physica B-Condensed Matter* 263 (1999), 571–573.
- [59] PEZERIL, T., CHIGAREV, N., RUELLO, P., GOUGEON, S., MOUNIER, D., BRETEAU, J. M., PICART, P., AND GUSEV, V. Laser acoustics with picosecond collimated shear strain beams in single crystals and polycrystalline materials. *Physical Review B* 73, 13 (2006).

- [60] PROFUNSER, D. M. *Laserbased Ultrasound for Characterization of Thin Films and Microstructures and Resulting Applications*. Diss. ETH No. 15728. Zurich, 2004.
- [61] PROFUNSER, D. M., VOLLMANN, J., AND DUAL, J. Ultrasonic wave propagation in focussing tips with arbitrary geometries. *Ultrasonics* 40, 1-8 (2002), 747–752.
- [62] PROFUNSER, D. M., WRIGHT, O. B., AND MATSUDA, O. Imaging ripples on phononic crystals reveals acoustic band structure and bloch harmonics. *Physical Review Letters* 97, 5 (2006).
- [63] QIU, T. Q., AND TIEN, C. L. Short-pulse laser-heating on metals. *International Journal of Heat and Mass Transfer* 35, 3 (1992), 719–726.
- [64] RICHARDSON, C. J. K., AND SPICER, J. B. Short-time thermoelastic contributions to picosecond-time scale reflectivity measurements of metals. *Applied Physics Letters* 80, 16 (2002), 2895–2897.
- [65] ROYER, D., AND DIEULESAINT, E. *Elastic Waves in Solids I*. Springer, 2000.
- [66] SCHIFT, H., PARK, S., JUNG, B. Y., CHOI, C. G., KEE, C. S., HAN, S. P., YOON, K. B., AND GOBRECHT, J. Fabrication of polymer photonic crystals using nanoimprint lithography. *Nanotechnology* 16, 5 (2005), S261–S265.
- [67] SCHUBERT, F., PEIFFER, A., KOHLER, B., AND SANDERSON, T. The elastodynamic finite integration technique for waves in cylindrical geometries. *Journal of the Acoustical Society of America* 104, 5 (1998), 2604–2614.
- [68] SEARLE, T. *Properties of amorphous silicon and its alloys*. INSPEC the Institution of Electrical Engineers, London, 1998.
- [69] SENOUSSAOUI, N. *Einfluss der Oberflächenstrukturierung auf die optischen Eigenschaften der Dünnschichtsolarzellen auf der Basis von a-Si:H und uc-Si:H*. Diss. Heinrich-Heine-Universität. Düsseldorf, 2003.
- [70] SHELTON, L. J., YANG, F., FORD, W. K., AND MARIS, H. J. Picosecond ultrasonic measurement of the velocity of phonons in water. *Physica Status Solidi B-Basic Solid State Physics* 242, 7 (2005), 1379–1382.
- [71] SPEAR, W. E., AND LECOMBER, P. G. Substitutional doping of amorphous silicon. *Solid State Communications* 17, 9 (1975), 1193–1196.
- [72] TAFLOVE, A., AND HAGNESS, S. C. *Computational electrodynamics, the finite-difference time-domain method*. Artech House, Boston, London, 2005.
- [73] TAS, G., AND MARIS, H. J. Electron-diffusion in metals studied by picosecond ultrasonics. *Physical Review B* 49, 21 (1994), 15046–15054.
- [74] TAYLOR, B., MARIS, H. J., AND ELBAUM, C. Focusing of phonons in crystalline solids due to elastic anisotropy. *Physical Review B* 3, 4 (1971), 1462–1472.

-
- [75] TEMPLE, J. A. G. Modeling the propagation and scattering of elastic-waves in inhomogeneous anisotropic media. *Journal of Physics D-Applied Physics* 21, 6 (1988), 859–874.
- [76] THOMSEN, C., GRAHN, H. T., MARIS, H. J., AND TAUC, J. Surface generation and detection of phonons by picosecond light-pulses. *Physical Review B* 34, 6 (1986), 4129–4138.
- [77] THOMSEN, C., MARIS, H. J., AND TAUC, J. Picosecond acoustics as a non-destructive tool for the characterization of very thin-films. *Thin Solid Films* 154, 1-2 (1987), 217–223.
- [78] TZOU, D. *Macro- to Microscale Heat Transfer - The lagging Behaviour*. Series in Chemical and Mechanical Engineering. Taylor and Francis, 1996.
- [79] VAN KREVELEN, D. W. *Properties of Polymers*, 3rd ed. Elsevier Science Publishing Company, 1990.
- [80] VIRIEUX, J. Sh-wave propagation in heterogeneous media - velocity-stress finite-difference method. *Geophysics* 49, 11 (1984), 1933–1942.
- [81] VIRIEUX, J. P-sv-wave propagation in heterogeneous media - velocity-stress finite-difference method. *Geophysics* 51, 4 (1986), 889–901.
- [82] VOLLMANN, J., PROFUNSER, D. M., AND DUAL, J. Sensitivity improvement of a pump-probe set-up for thin film and microstructure metrology. *Ultrasonics* 40, 1-8 (2002), 757–763.
- [83] VOLLMANN, J., PROFUNSER, D. M., MEIER, A. H., DOBELI, M., AND DUAL, J. Pulse laser acoustics for the characterization of inhomogeneities at interfaces of microstructures. *Ultrasonics* 42, 1-9 (2004), 657–663.
- [84] WENKE, I. *Laserbased Generation and Detection of Ultrasound Waves in Thin Films*. Diploma Thesis ETH. Zurich, 2007.
- [85] WRIGHT, O. B. Thickness and sound-velocity measurement in thin transparent films with laser picosecond acoustics. *Journal of Applied Physics* 71, 4 (1992), 1617–1629.
- [86] WRIGHT, O. B., AND KAWASHIMA, K. Coherent phonon detection from ultrafast surface vibrations. *Physical Review Letters* 69, 11 (1992), 1668–1671.
- [87] WRIGHT, O. B., PERRIN, B., MATSUDA, O., AND GUSEV, V. E. Optical excitation and detection of picosecond acoustic pulses in liquid mercury. *Physical Review B* 78, 2 (2008).
- [88] WRIGHT, O. B., SUGAWARA, Y., MATSUDA, O., TAKIGAHIRA, M., TANAKA, Y., TAMURA, S., AND GESEV, V. E. Real-time imaging and dispersion of surface phonons in isotropic and anisotropic materials. *Physica B-Condensed Matter* 316 (2002), 29–34.

- [89] ZHOU, B. Q., LIU, F. Z., GU, J. H., ZHANG, Q. F., ZHOU, Y. Q., AND ZHU, M. F. Nano-structure in micro-crystalline silicon thin films studied by small-angle x-ray scattering. *Thin Solid Films* 501, 1-2 (2006), 113–116.
- [90] ZHOU, Z., AND YAN, D. Mean-square radius of gyration of polymer chains. *Macromol. Theory Simul.* 6 (1997), 597–611.

Curriculum vitae

Jürg Bryner

Born on April 19, 1976 in Winterthur, Switzerland
Citizen of Kloten ZH, Switzerland

Education

1983 - 1989	Primary school in Winterthur, Switzerland
1989 - 1996	Gymnasium Rychenberg in Winterthur, Switzerland Graduation with a matura, type B
1996 - 2001	Studies in mechanical engineering at the Swiss Federal Institute of Technology (ETH) Zurich, Switzerland Graduation as Dipl. Masch.-Ing. ETH
2005 - 2009	Doctoral student at the Institute of Mechanical Systems (IMES, Center of Mechanics), Swiss Federal Institute of Technology (ETH) Zurich, Switzerland

Professional experience / practical trainings

Aug. - Oct. 1996	Practical training at Rieter AG, Winterthur, Switzerland
Jul. - Oct. 1999	Practical training at Mannesmann Dematic AG, Dietlikon, Switzerland
2001 - 2004	Development Engineer at Zuhlke Engineering AG, Schlieren, Switzerland
2005 - 2009	Research and teaching assistant at the Institute of Mechanical Systems (IMES, Center of Mechanics), Swiss Federal Institute of Technology (ETH) Zurich, Switzerland

List of publications

- Bryner J., Vollmann J., Aebi L., Dual J., *Wave propagation in pyramidal tip-like structures with cubic material properties*, Accepted for publication, Wave Motion Journal, Elsevier, 2009
- Bryner J., Kehoe T., Vollmann J., Aebi L., Wenke I., Dual J., *Phonon attenuation in the GHz regime: Measurements and simulations with a visco-elastic material model*, Proceedings of the International Congress on Ultrasonics, Santiago (Chile), 2009
- Bryner J., Kehoe T., Vollmann J., Aebi L., Sotomayor Torres C., Dual J., *Characterization of nanoimprinting polymers with laser ultrasonics*, Proceedings of the International Congress of Theoretical and Applied Mechanics, Adelaide (Australia), 2008
- Bryner J., Vollmann J., Bugnard G., Dual J., *3-D wave propagation in anisotropic microstructures with tilted orthotropic axes*, Proceedings of the International Congress on Ultrasonics, Vienna (Austria), 2007
- Bryner J., Kehoe T., Vollmann J., Aebi L., Sotomayor Torres C., Dual J., *Characterization of nanoimprinting polymer films using picosecond ultrasonics*, Proceedings of the IEEE International Ultrasonics Symposium, New York (USA), 2007
- Bryner J., Vollmann J., Profunser D.M., Dual J., *Simulation of the elastic wave propagation in anisotropic microstructures*, Proceedings of the Society of Photo-Optical Instrumentation Engineers (SPIE), Munich (Germany), 2007
- Bryner J., Vollmann J., Profunser D.M., Bugnard G., Dual J., *Elastic wave propagation in anisotropic microstructures for the interpretation of laser acoustic measurements*, Proceedings of the IEEE International Ultrasonics Symposium, Vancouver (Canada), 2006
- Bryner J., Profunser D.M., Vollmann J., Mueller E., Dual J., *Characterization of Ta and TaN diffusion barriers beneath Cu layers using picosecond ultrasonics*, Ultrasonics 44, e1269-e1275, 2006